



HAL
open science

Multiple Antenna Communications for 5G

Kalyana Gopala

► **To cite this version:**

Kalyana Gopala. Multiple Antenna Communications for 5G. Networking and Internet Architecture [cs.NI]. Sorbonne Université, 2018. English. NNT : 2018SORUS352 . tel-02865497

HAL Id: tel-02865497

<https://theses.hal.science/tel-02865497>

Submitted on 11 Jun 2020

HAL is a multi-disciplinary open access archive for the deposit and dissemination of scientific research documents, whether they are published or not. The documents may come from teaching and research institutions in France or abroad, or from public or private research centers.

L'archive ouverte pluridisciplinaire **HAL**, est destinée au dépôt et à la diffusion de documents scientifiques de niveau recherche, publiés ou non, émanant des établissements d'enseignement et de recherche français ou étrangers, des laboratoires publics ou privés.

Sorbonne Université

Ecole Doctorale

Doctorat, Communication Systems Department

KALYANA GOPALA

MULTIPLE ANTENNA COMMUNICATIONS FOR 5G

Thèse dirigée par Prof. Dirk Slock, Professor, Eurecom, France

Soutenu le 7 Dec 2018

Prof. Naceur Malouch
Prof. Constantinos B. Papadias
Prof. Luc Deneire
Prof. Dirk Slock
Prof. Laura Cottatellucci
Dr. Maxime Guillaud

President du Jury
Rapporteur
Rapporteur
Jury
Jury
Jury

ABSTRACT

Multiple antenna communications is now ubiquitous, well researched by the academia and well accepted by the industry as can be seen by its presence in the third generation partnership project (3GPP) standards all the way up to the recent Release 15 for the fifth generation (5G) New Radio (NR). In this thesis, we pick two areas that are important research areas in multiple input multiple output (MIMO).

- Optimal algorithms for reciprocity calibration, particularly for the massive MIMO (MaMIMO) scenario.
- Precoding techniques for rapidly time-varying point to point MIMO channels like that seen for high-speed trains (HST).

MaMIMO is key to enabling the 1000x data rate promised by 5G. The effectiveness of MaMIMO, in turn, depends crucially on the availability of channel state information at the transmitter (CSIT). CSIT may be obtained either via feedback or using the concept of reciprocity. In the case of MaMIMO with a massive number of base station (BS) antennas, the preferred choice is reciprocity in conjunction with Time Division Duplexing (TDD). However, while the propagation channel is reciprocal, the overall end to end digital channel is not reciprocal due to the presence of Transmit (Tx) and Receive (Rx) chains which need to be corrected for to derive the CSIT. Hence, we consider a TDD MaMIMO scenario and look into internal calibration where the calibration is done internally over the air amongst the antennas of the BS. Our work provides a simple and elegant expression of the Cramer Rao Bound (CRB) for calibration parameter estimation for a general calibration framework that allows grouping of antennas. In addition, the CRB is applicable to both coherent and non-coherent estimation methods. We provide analysis for the existing least squares approaches and propose optimal algorithms to estimate the calibration parameters. In a typical setting, a TDD MaMIMO operates in two phases - the first one is a calibration phase where the calibration parameters are computed. It is then followed by a data phase where actual data transmission happens. We propose a novel method to perform calibration simultaneously with the data transmission in the Long Term Evolution (LTE) framework with no change in existing standards. A patent has been applied for this method.

We also consider precoding for a rapidly time-varying point to point MIMO link as encountered in HST. The high Doppler encountered in HST environments violates the orthogonality requirement for Orthogonal Frequency Division Multiplexing (OFDM), resulting in inter-carrier interference (ICI). While several prior works have focused on receiver techniques to mitigate ICI and it is known that multiple receive antennas in a single input multiple output (SIMO) scenario are very effective in canceling out the ICI, there has been no existing work on optimal precoder design in the case of MIMO. We study this problem under full CSIT. We first justify a linear approximation for the channel variation across the OFDM symbol. With the linearity

assumption, it is observed that the MIMO precoder design problem is similar to that of a MIMO Interfering Broadcast Channel (IBC) precoding design that maximizes the weighted sum rate (WSR). Hence, we reuse a known technique [23] employed in MIMO IBC, but re-interpret it as a majorization [38] approach. The precoder design takes into account receive windowing using the excess cyclic prefix (CP) and the window is jointly designed with the Tx precoder. CSIT is difficult to obtain in general, more so in the case of rapidly time-varying channels. Hence, in addition to full CSIT, this part of the work also investigates partial CSIT approaches where the Tx has only partial knowledge of the channel. We choose expected WSR (EWSR) as the metric to be optimized under partial CSIT. First, we use a large system approximation that also works well for a small number of Tx and Rx antennas to derive the precoders. Expected-signal-expected-interference-WSR (ESEI-WSR) is another metric that is applicable as the number of Tx antennas becomes large compared to that of the number of Rx antennas. The optimization under this metric is more mathematically tractable compared to that of the EWSR. In our work, we analyze the possibility of using the ESEI-WSR instead of the EWSR.

Finally, experimental results on the Eurecom MaMIMO testbed are presented that exploit some of the theory that has been discussed so far. The first experiment performs precoding for a TDD MaMIMO scenario using DL channel estimated via reciprocity calibration. The next experiment focuses on multi-user multi-cell precoding under partial CSIT while taking into account the end-to-end channel non-reciprocity. A third experiment explores the use of multiple antennas to mitigate self-interference for a Full Duplex (FD) scenario. Conclusions and a list of contributions are given in Chapter 7. This research has resulted in 8 conference publications, a journal publication, and a patent application.

DEDICATION AND ACKNOWLEDGEMENTS

I would like to acknowledge my gratitude to my supervisor Prof. Dirk Slock for guiding me in each of the contributions of this thesis. His clarity of thought and breadth of technical knowledge never ceases to amaze me.

I would like to express my deepest gratitude to Prof. V.U. Reddy who has always been my guide and upon whose advise I applied for this PhD position under Prof. Slock. I would also like to thank the two review members of the "comite de suivi" who have taken the trouble to review my progress during the first and second year of my Ph.D. I thank them deeply for asking me difficult but pertinent questions that have helped me look at my research from a different perspective.

As with every Ph.D., this journey has seen it's ups and downs and that is where my friends and family have served as super stress busters. Thanks to all my friends inside and outside of Eurecom. I have been fortunate to be a part of two lunch groups that gives me a sense of belonging to the place. In particular, I would like to thank Leela Gudupudi and his wife Vineela Krishna who made us feel at home during the initial days at Sophia Antipolis. My special thanks to Christo and Elena for helping me review the thesis write up. Would like to especially thank Sumit, Pramod, Rajeev, Pepe, Hector, Max, Christo, Jasmi, Ashwin, Gayatri, Krishna, Vaishnavi....

I have also grown as an individual thanks to the non-technical courses at Eurecom. Of special mention has been the association with the Professors Ken Pope & Andrew prior and my Team Lead group Fantastic 4.

And I am forever indebted to my parents, my sisters, my two precious kids and my wife for being the joy of my life. I would like to especially acknowledge the efficiency and multi-tasking skills of my wife that helped manage life as normal during the tenure of my Ph.D.

TABLE OF CONTENTS

	Page
List of Tables	ix
List of Figures	xi
1 Introduction	1
1.1 Notations	4
1.2 Organization of the thesis	4
2 Reciprocity Calibration for Massive MIMO	7
2.1 Introduction	7
2.1.1 UE aided calibration and Internal calibration	9
2.1.2 Coherent and Non-coherent calibration scheme	9
2.1.3 Key assumptions	10
2.2 State of the Art	11
2.2.1 Argos	11
2.2.2 Rogalin Method	12
2.2.3 Avalanche	13
2.2.4 Method in [43]	14
2.3 Group calibration System Model	14
2.3.1 Least Squares Solution	15
2.3.2 Fast Calibration	16
2.3.3 Non-coherent estimation	18
2.4 Cramer Rao Bound	18
2.5 Optimal Algorithms	21
2.5.1 Alternating Maximum Likelihood (AML)	21
2.5.2 Variational Bayes approach	22
2.6 Maximum likelihood vs. least squares	23
2.7 Analysis of least squares methods	24
2.8 Simulation Results	26
2.8.1 Comparison of grouping based schemes	27

TABLE OF CONTENTS

2.8.2	Comparison of single antenna transmission schemes	32
2.9	Summary of Contributions	33
3	Precoder design under Doppler - Full CSIT	35
3.1	Introduction	35
3.1.1	Key Assumption	36
3.2	System Model	36
3.3	Precoder Design	40
3.3.1	Covariance matrix update	40
3.3.2	Power allocation across the subcarriers	43
3.3.3	Optimization of window parameters - Gradient descent	43
3.3.4	Overall Algorithm and Convergence	44
3.4	Simulation Results	44
3.5	Summary of Contributions	49
4	Precoder design under Doppler - partial CSIT	51
4.1	System Model	51
4.2	Large MIMO asymptotics	53
4.2.1	Precoder Design	54
4.2.2	Simulation Results	56
4.3	Summary of Contributions	56
5	Analysis of the Gap between EWSR and ESEI-WSR	59
5.1	MIMO IBC Signal Model	59
5.2	EWSR	60
5.3	MaMIMO limit and ESEI-WSR	60
5.4	EWSR to ESEI-WSR gap Analysis	61
5.4.1	Monotonicity of gap with SNR	62
5.4.2	Second-Order Taylor Series Expansion of EWSR	63
5.4.3	MISO correlated channel	63
5.4.4	MIMO zero mean i.i.d channel	65
5.5	Actual EWSR Gap	66
5.6	Simulation Results	67
5.7	Conclusion	67
5.8	Summary of Contributions	68
6	Experimental results	69
6.1	Downlink channel estimation via RCMM.	69
6.1.1	Massive MIMO testbed	69
6.1.2	Frame structure	72

6.1.3	Results	73
6.2	MU-MIMO precoding for a 2 BS, 2 UE scenario	74
6.2.1	Channel Estimation	75
6.2.2	EWSR Lower Bound: EWSMSE	75
6.2.3	Dual DL precoder	77
6.2.4	Results	78
6.3	Multiple antenna based self-interference cancellation for Full Duplex	80
6.3.1	USRP based testbed	81
6.3.2	Frame structure	82
6.3.3	Results	83
6.4	Summary of Contributions	85
7	Conclusion	87
7.1	Contributions	89
7.1.1	Chapter 2	89
7.1.2	Chapter 3	89
7.1.3	Chapter 4	90
7.1.4	Chapter 5	90
7.1.5	Chapter 6	91
A	Appendix A	93
	Bibliography	95

LIST OF TABLES

TABLE	Page
2.1 The number of channel uses required for calibration	18
2.2 Number of antennas transmitting at each channel use for two Fast Calibration schemes.	27
3.1 Overall Algorithm to solve objective function f_0	45
4.1 Overall Algorithm for precoder design	55
6.1 Parameters of the Massive MIMO Prototype	71

LIST OF FIGURES

FIGURE	Page
1.1 Typical cellular architecture depicting different cells.	2
2.1 Reciprocity Model in Time Division Duplexing	8
2.2 Illustration of coherent and non-coherent calibration	10
2.3 Illustration of the group calibration system model	15
2.4 Comparison of fast calibration with Avalanche scheme ($M = 64$ and the number of channel uses is 12). The curves are averaged across 500 channel realizations. The performance with both the FCC and NPC constraints is shown.	29
2.5 Comparison of fast calibration with Avalanche scheme for $M = 67$ and the number of channel uses=12. The curves are averaged across 500 channel realizations. The NPC constraint is used for the MSE computation.	30
2.6 Comparison of CRB with different antenna group sizes for $M = 64$ antenna scenario.	31
2.7 64 antennas arranged as a 4×16 grid.	31
2.8 Interleaved and non-interleaved MSE and CRB with NPC for an antenna transmit group size of 4 ($M = 64$ and the number of channel uses is $G = 16$).	32
2.9 Comparison of single antenna transmit schemes with the CRB ($G = M = 16$). The curves are generated over one realization of an i.i.d. Rayleigh channel and a known first coefficient constraint is used.	33
2.10 Comparison of simulation MSE for an $M = 32$ antenna scenario with the theoretical expression for MSE for the first coefficient known constraint (FCC).	34
2.11 Convergence of the various iterative schemes for $M = 16$ and $G = M$	34
3.1 Illustration of ExCP windowing in an OFDM symbol	36
3.2 Verification of the linear model for channel variation.	38
3.3 Simulation Results with $N_t = 4, N_r = 3, N = 64, N_e = 16$ and Doppler of 450Kmph	46
3.4 Comparison of windows used to exploit ExCP. $N_t = 4, N_r = 3, N = 64, N_e = 16$	47
3.5 Simulation Results with $N_t = 3, N_r = 3, N = 64, N_e = 16$, and Doppler of 450Kmph	48
3.6 Comparison of windows used to exploit ExCP. $N_t = 3, N_r = 3, N = 64, N_e = 16$	48
4.1 EWSR comparison for $N_t = 6, N_r = 3$	56

5.1	Gap between ESEI-WSR and EWSR for the MISO correlated scenario for different values of transmit antennas.	67
5.2	Gap obtained from the second-order Taylor series approximation vs. the true value of the gap for a MIMO correlated scenario. The number of antennas at each receiver, N_k , is taken as 4.	68
6.1	Eurecom MaMIMO prototype	70
6.2	Demo configuration for RCMM	70
6.3	Software setup for the experiment.	71
6.4	Frame structure for calibration parameter estimation.	72
6.5	Frame structure for MRT transmission to verify the reciprocity calibration. SF refers to subframe.	73
6.6	Performance of MRT with and without calibration for a 23 antenna BS with a single UE.	74
6.7	Demo configuration for MU-MIMO precoding.	75
6.8	Example plot for the channel taps in the time domain.	76
6.9	Performance of MRT and ZF precoders compared to no precoding	79
6.10	Comparison of the performance of partial CSIT LMMSE precoder with that of ZF which requires full information of cross-links.	80
6.11	FD demo configuration in the lab.	81
6.12	FD demo setup in the lab.	82
6.13	Frame structure for channel estimation.	83
6.14	Frame structure for precoding.	83
6.15	Signal level and constellation plot at UE for the different precoding approaches.	84
6.16	Interference level at the BS Rx for different BF approaches.	84
6.17	BS Tx-Rx configuration to measure the rank profile.	85
6.18	Smaller singular value at each subcarrier for the 2×2 channel. The larger singular value is normalized to unity.	86

ABBREVIATIONS

3GPP	Third generation partnership project
5G	Fifth generation
BS	Base Station
CP	Cyclic Prefix
CRB	Cramer-Rao Bound
CSI	Channel State Information
CSIT	Channel State Information at the Transmitter
CSIR	Channel State Information at the Receiver
DC	Difference of Convex functions
DL	Downlink
eMBB	enhanced Mobile Broadband
ESEI-WSR	Expected Signal covariance Expected Interference covariance based WSR
EWSMSE	Expected Weighted Sum Mean Squared Error
EWSR	Expected WSR
FD	Full Duplex
FDD	Frequency Division Duplexing
FIR	Finite Impulse response
FFT	Fast Fourier Transform
HST	High-speed trains
i.i.d	Independent and identically distributed
IBC	Interference Broadcast Channels
ICI	Intercarrier Interference
LoS	Line of Sight
LS	Large Scale
LTE	Long Term Evolution
LTI	Linear time-invariant
MaMIMO	Massive MIMO
mMTC	massive machine type communication

MF	Matched Filter
MMSE	Minimum Mean Squared Error
MIMO	Multiple-Input Multiple-Output
MISO	Multiple-Input Single-Output
MRC	Maximum Ratio Combining
MRT	Maximum Ratio Transmission
MSE	Mean Squared Error
MU	Multiuser
Mu-MIMO	Multiuser MIMO
NLOS	Non-LoS
NR	New Radio
OFDM	Orthogonal Frequency-Division Multiplexing
OTA	Over-the-air
RCMM	Reciprocity Calibration for Massive MIMO
RF	Radio Frequency
Rx	Receiver
SIMO	Single Input Multiple Output
SINR	Signal to Interference plus Noise Ratio
SNR	Signal to Noise Ratio
SoA	State of the Art
TDD	Time Division Duplexing
Tx	Transmitter
UL	Uplink
URLLC	Ultra Reliable and Low latency Communication
USRP	Universal Software Radio Peripheral
WiMAX	Worldwide Interoperability for Microwave Access
WSMSE	Weighted Sum Mean Squared Error
WSR	Weighted Sum Rate
ZF	Zero-Forcing

INTRODUCTION

Cellular networks have enabled the wide reach of wireless networks and have made wireless communication universal. Figure 1.1 shows a typical cellular network consisting of base stations (BS) and user equipment (UE). The link from BS to UE forms the downlink (DL) and the reverse link from UE to BS is referred to as the uplink (UL). Cellular technology has evolved tremendously since their initial deployment in the 1980s and today, we are at an important threshold where the fifth generation (5G) has been standardized by the third generation partnership project (3GPP) and is undergoing field trials by the industry. The air interface for 5G is known as New Radio (NR). A good overview of the initial evolution of the wireless standards may be found in [14].

Note that the BS talks to multiple UE and the available resources (in time and spectrum) have to be judiciously allocated across these multiple UEs which compete for access to the resources. Hence, the choice of an appropriate modulation scheme and multiple access technique is crucial. Beyond the third generation (3G) of cellular networks, Orthogonal Frequency Division Multiplexing (OFDM) has been the preferred choice for modulation. OFDM divides the overall frequency selective channel into overlapping but orthogonal bands called subcarriers. Each subcarrier can be processed individually in a frequency flat manner resulting in a low complexity receiver (Rx) even at high bandwidths. Note that spectrum availability in a given region is a function of geographic locations and the frequency band of operation. Again, OFDM fits naturally to this kind of a scenario as it is easy to scale the OFDM to different bandwidths. Hence, both the competing technologies for the fourth generation (4G), Worldwide Interoperability for Microwave Access (WiMAX) and long term evolution (LTE) were based on OFDM. Another important consideration in a cellular system is the choice of a Duplexing scheme that allows the two-way communication between the BS and the UE. In a time division duplexing (TDD) scheme, the UL

and DL transmissions occur on the same frequency band but at different time intervals. In a frequency division duplexing (FDD) scheme, the transmission intervals may overlap but the UL and DL happen over different frequency bands.

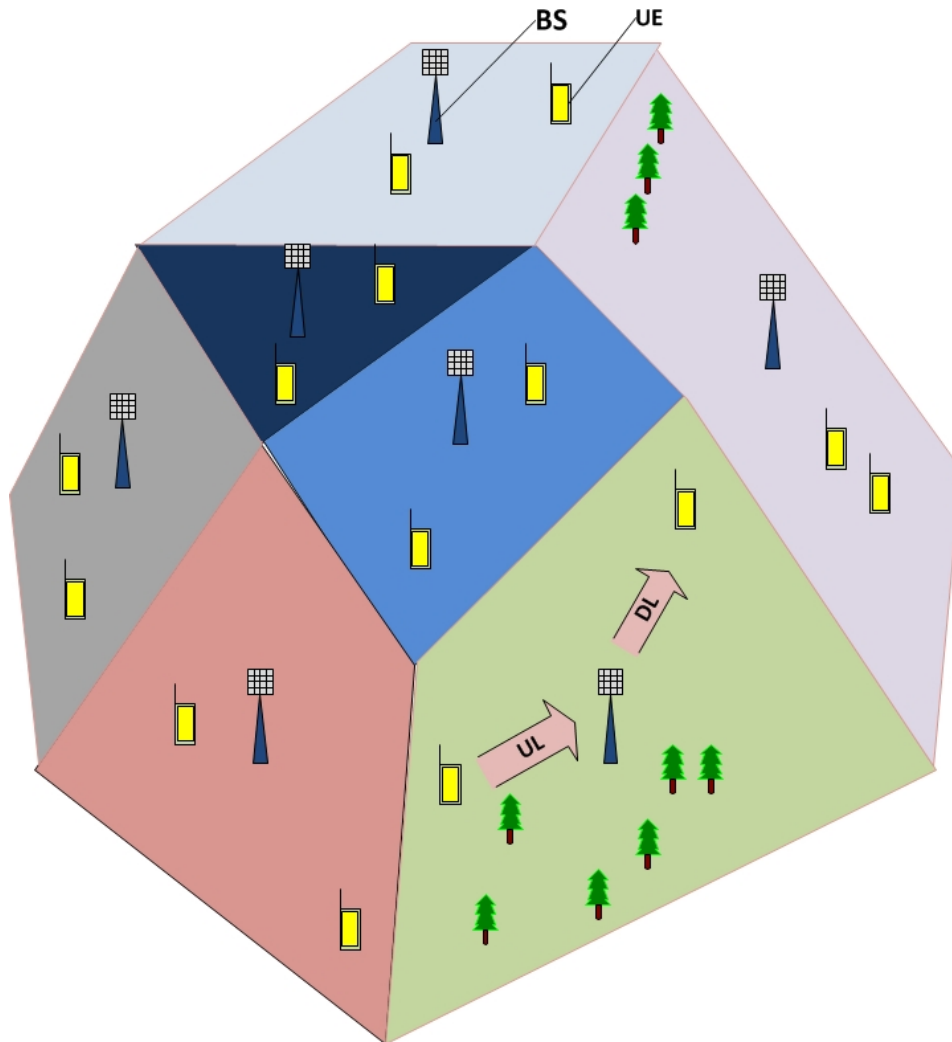


Figure 1.1: Typical cellular architecture depicting different cells.

The phase 1 standardization of 5G was approved by the 3GPP in July 2018. The new standard ushers in new use cases like the massive machine type communication (mMTC) and Ultra Reliable and Low latency Communication (URLLC). It also extends the existing 4G services in a use case termed the enhanced Mobile Broadband (eMBB). An important mandate here is the targeted 1000x increase in wireless data capacity. A better term for this "wireless data capacity" is area throughput [9].

$$(1.1) \quad \text{Area throughput [bit/s/km}^2\text{]} = B[\text{Hz}] \cdot D[\text{cells/km}^2] \cdot \text{SE},$$

where B is the bandwidth, D is the average cell density and SE is the spectral efficiency per cell.

This clearly implies that to achieve the ambitious 1000x target, one has to focus on all the three components. Noting that bandwidth is a scarce and costly resource and cell densification has a negative impact on handoff requirements and quality of service for the high mobility customers, a reasonable approach is to first look for avenues to increase the SE. It is well known that increase in SNR improves the SNR only logarithmically whereas multiple antennas can result in a linear increase in capacity with an increase in the number of antennas at Transmitter (Tx) and Rx [40]. Specifically, the capacity of a point to point Multiple Input Multiple Output (MIMO) link gets scaled by the minimum of the number of Tx and Rx antennas. Practically, increasing the number of antennas at the BS (M) is easier compared to that at the UE which typically has one or a few antennas. This motivates the concept of a multi-user MIMO (MU-MIMO) where multiple UEs communicate with the BS over the same time and frequency resource in the UL. This has an additional advantage too that it is easier to have a rich scattering channel which is crucial for MIMO multiplexing gains. Thus, at least in theory, MU-MIMO is capable of providing us with the desired SE increase. When MU-MIMO or space division multiple access (SDMA) was introduced in 4G, the number of BS antennas M was assumed to be of the same order as that of the number of UEs with which simultaneous communication was to be established. In practice, this is hard to scale beyond a few UEs due to the high receiver complexity and unpredictable link quality in a non-line of sight (NLoS) environment. The seminal works by Marzetta [26],[25] showed the advantages of having a large number of BS antennas for a finite number of UEs. This configuration, popularly known as Massive MIMO (MaMIMO) greatly simplifies the UL and DL precoders. In fact, owing to the phenomenon of channel hardening and favorable propagation, simple maximal ratio combining (MRC) in the UL and maximal ratio transmission (MRT) in the DL become optimal asymptotically. As a result, MaMIMO is a practical approach to realize the gains of MU-MIMO.

The effectiveness of MaMIMO (as in the case of MU-MIMO), in turn, depends crucially on the availability of channel state information at the transmitter (CSIT). That is, a BS with a massive number of antennas requires the knowledge of the downlink (DL) channel to each of the user equipments (UEs) to perform multi-user precoding. Given the massive number of antennas, a direct estimation of these channels in the DL would be impractical taking into account the number of pilots to be transmitted and the amount of channel information that a UE has to feedback to the BS. In a TDD system, one can exploit reciprocity of the physical propagation channel to derive the DL channel from the UL channel estimates. Hence, what is popular today is to consider TDD MaMIMO systems. The assumption of channel reciprocity is strictly true only for the propagation channel and not for the end to end digital channel that involves the Tx and Rx chains. It is possible to model and correct this loss of reciprocity digitally using linear multiplicative factors termed calibration parameters. This, in turn, calls for algorithms to estimate these parameters. This topic is called Reciprocity Calibration for MaMIMO (RCMM) and forms part of our research focus. We benchmark these algorithms by coming up with the

Cramer Rao Bound (CRB) for these algorithms. Next, we also come up with optimal algorithms for transmit antenna array calibration. In addition to the theoretical work, we also perform experimental work that complements some of our theoretical work.

3GPP standards for LTE and NR have been designed to support speeds of up to 500kmph. The high Doppler in these environments violates the orthogonality requirement for OFDM, resulting in ICI. Thus, Performance of OFDM systems is limited by inter-carrier interference (ICI) under high Doppler scenarios such as that encountered in high-speed trains (HST). While the lower data rate transmissions are not impacted by Doppler, the higher data rates are severely impacted. Several publications have addressed the receiver design for SISO (single input single output) and single input multiple output (SIMO) to combat ICI. Notably, the use of multiple receive antennas is known to be a very effective way to combat ICI. In our research, we investigate precoding techniques for rapidly time-varying MIMO channels like that seen for HST. I.e, we focus on exploiting the transmit antennas to mitigate the impact of ICI. Of course, such a design has to take into account receiver capabilities as well. Hence, in our Tx precoder design, we also factor in the presence of excess cyclic prefix (CP) at the receiver that can further mitigate the ICI. Channel state information at the Tx (CSIT) is difficult to obtain in general, more so in the case of rapidly time-varying channels. Hence, in addition to full CSIT, this part of the work also investigates partial CSIT approaches where the Tx has only partial knowledge of the channel.

1.1 Notations

In the following discussions, a bold notation in small letters indicates a vector and bold notation with capital letters indicates a matrix. On some occasions, calligraphic font with capital letters is also used for matrices. Unless otherwise specified, vector refers to a column vector. The operation "diag" has an interpretation identical to that in Matlab. When applied to a vector, it produces a diagonal matrix with the diagonal elements formed out of the same vector. When the operation is performed on a diagonal matrix, the result is a column vector formed out of the diagonal elements of this matrix. $E(\cdot)$ is the expectation operator. \otimes refers to the Kronecker product. In the following text, the notation $|\mathbf{A}|$ refers to the determinant of the matrix \mathbf{A} . \ln refers to natural logarithm. $\mathcal{CN}(\mu, \mathbf{C})$ refers to a circularly complex Gaussian distribution with mean μ and covariance \mathbf{C} . Tx may denote transmit/transmitter/transmission and Rx may denote receive/receiver/reception. The list of abbreviations has also been separately tabulated.

1.2 Organization of the thesis

Chapter 2 contains the entire theoretical research on reciprocity calibration for MaMIMO. First, the reciprocity model is introduced clearly demarcating the propagation channel which is reciprocal and the non-reciprocal radio frequency (RF) chain. We then explain various terminology, namely, UE aided calibration and Internal calibration, Coherent and non-coherent calibration,

etc. This is followed by some of the relevant state of the art (SoA). We derive the CRB for these algorithms under a more general setting that allows for antenna grouping. Our results apply to both coherent and non-coherent calibration techniques. We also present new optimal algorithms for transmit antenna array calibration.

Chapters 3,4 deal with the topic of sum rate maximization for a point to point MIMO transmission under Doppler. Chapter 3 considers the problem of precoder design for an HST scenario under complete CSIT. To make the analysis tractable, the channel variation is assumed to be linear as has been done previously in the literature and it is shown that this approximation is justified for our problem scenario. With this setting, we observe that the problem of precoder design under ICI is similar to that of a MIMO Interfering Broadcast Channel (IBC) precoding design and hence tap into existing solutions in that space. The design is extended to account for the presence of Excess CP (ExCP) wherein optimal window parameters are also derived to take advantage of the ExCP. The same problem is treated under a more realistic setting of partial CSIT in Chapter 4. Chapter 5 continues to analyze the problem of partial CSIT that was started in Chapter 4. However, the problem formulation in Chapter 5 considers a general setting of MIMO IBC and analyses the possibility of approximating the expected weighted sum rate (EWSR) metric with the expected-signal-expected-interference-WSR (ESEI-WSR) metric. Finally, in Chapter 6 we perform an experimental validation on the Eurecom MaMIMO testbed that exploits some of the theory that has been discussed so far. The first experiment performs precoding for a TDD MaMIMO scenario using DL channel estimated via reciprocity calibration. The next experiment focuses on multi-user multi-cell precoding under partial CSIT while taking into account the end-to-end channel non-reciprocity. A third experiment explores the use of multiple antennas to mitigate self-interference for a Full Duplex (FD) scenario.

The final chapter provides the conclusions. At the end of every chapter, the list of contributions and associated publications are provided. However, for easy reference, the final chapter also lists out the contributions from our research chapter-wise. In this thesis, if any particular result is not the work of the author, an explicit reference to the source is provided.

RECIPROCITY CALIBRATION FOR MASSIVE MIMO

2.1 Introduction

In this chapter, we present our work on reciprocity calibration for a MaMIMO scenario. Consider a MaMIMO BS with M_A antennas talking to a user equipment (UE) having M_B number of antennas. To exploit the advantages of Massive MIMO, it is key to have channel state information at the transmitter (CSIT). The channel of interest here is of dimension $M_B \times M_A$. In the DL, estimation of the channel from each BS antenna requires a dedicated pilot to be transmitted from that antenna. As the number of antennas is massive, this demands a huge number of pilot transmissions resulting in severe loss of overall system throughput. At the same time, in the uplink (UL), a single pilot is sufficient to determine the channel from one UE antenna to all the BS antennas. Thus, in a MaMIMO scenario, it is more attractive to perform UL channel estimation. Hence, there is a lot of interest in deriving the DL channel estimates from the UL channel estimates. TDD Massive MIMO (MaMIMO) is an ideal candidate for this due to the common assumption of channel reciprocity. Simply put, this would imply that the estimated channel in the UL can be directly used as DL channel. However, the overall digital channel is not reciprocal. Fig. 2.1 shows a detailed picture of the components forming the overall digital channel between a pair of radios A and another pair of radios B . It is clear that the RF components are not reciprocal as the UL and DL signals traverse completely different paths beyond the switch.

In Fig. 2.1, \mathbf{C} refers to the propagation channel which is reciprocal. The $(i, j)^{th}$ entry of \mathbf{C} corresponds to the propagation channel between the antennas i and j . Hence, all diagonal elements of \mathbf{C} are undefined. The overall DL and UL channels observed in the digital domain are noted by $\mathbf{H}_{A \rightarrow B}$ and $\mathbf{H}_{B \rightarrow A}$. In the frequency domain, over a narrow frequency band, they can be represented by:

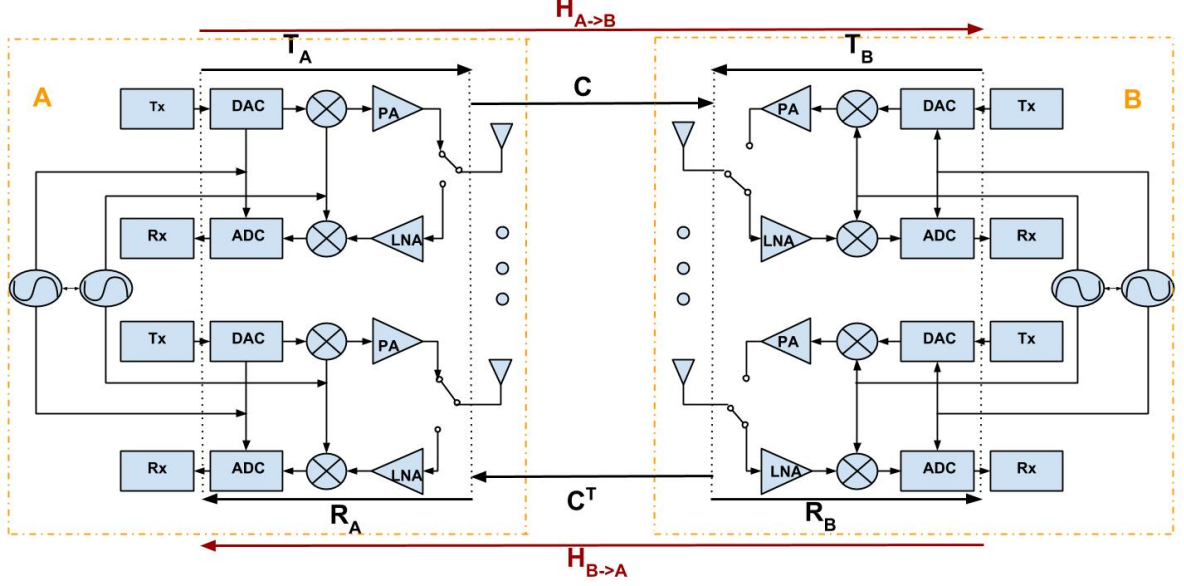


Figure 2.1: Reciprocity Model in Time Division Duplexing

$$(2.1) \quad \begin{cases} \mathbf{H}_{A \rightarrow B} = \mathbf{R}_B \mathbf{C} \mathbf{T}_A, \\ \mathbf{H}_{B \rightarrow A} = \mathbf{R}_A \mathbf{C}^T \mathbf{T}_B. \end{cases}$$

Matrices \mathbf{T}_A , \mathbf{R}_A , \mathbf{T}_B , \mathbf{R}_B model the response of the transmit and receive RF front-ends and are called the absolute calibration factors. The diagonal elements in these matrices represent the linear effects attributable to the impairments in the transmitter and receiver parts of the RF front-end respectively, whereas the off-diagonal elements correspond to RF cross-talk and antenna mutual coupling. Thus, the DL channel $\mathbf{H}_{A \rightarrow B}$ may be derived from the UL channel $\mathbf{H}_{B \rightarrow A}$ as follows.

$$(2.2) \quad \mathbf{H}_{A \rightarrow B} = \mathbf{R}_B (\mathbf{R}_A^{-1} \mathbf{H}_{B \rightarrow A} \mathbf{T}_B^{-1})^T \mathbf{T}_A = \underbrace{\mathbf{R}_B \mathbf{T}_B^{-T}}_{\mathbf{F}_B^{-T}} \mathbf{H}_{B \rightarrow A}^T \underbrace{\mathbf{R}_A^{-T} \mathbf{T}_A}_{\mathbf{F}_A} = \mathbf{F}_B^{-T} \mathbf{H}_{B \rightarrow A}^T \mathbf{F}_A.$$

Thus, the lack of reciprocity at the level of the RF chain brings in a need for reciprocity calibration factors \mathbf{F}_A and \mathbf{F}_B . If we drop the note of the set A and B, we have

$$(2.3) \quad \mathbf{F} = \mathbf{R}^{-T} \mathbf{T},$$

\mathbf{F} is called a relative calibration factor as it is obtained as a ratio of the absolute calibration factors. It is important to note that for the purpose of DL channel estimation, there is no need to estimate the absolute calibration factors. Instead, we need only the relative calibration factors. We would also like to point out here that for the purpose of precoding, we only need the knowledge of $\mathbf{H}_{A \rightarrow B}$ up to a complex gain factor. This can be seen from the fact that the final Tx output

power is determined by the Tx power constraints and that a common phase factor on all the Tx antennas does not have any impact on the precoding. In turn, hence, \mathbf{F}_A , \mathbf{F}_B also only need be determined up to a complex scale factor.

A TDD reciprocity based MIMO system normally has two phases for its function. First, during the initialization of the system or the training phase, the reciprocity calibration process is activated, which consists in estimating \mathbf{F}_A and \mathbf{F}_B . Then during the data transmission phase, these calibration coefficients are used together with instantaneous measured UL channel $\hat{\mathbf{H}}_{B \rightarrow A}$ to estimate the CSIT $\mathbf{H}_{A \rightarrow B}$, based on which advanced precoding algorithms can be performed. Since the calibration coefficients stay stable during quite a long time [37] (in the order of hours), the calibration process doesn't have to be done very frequently.

Co-located MaMIMO refers to a single BS with a massive number of antennas that are co-located. In contrast, in *distributed MaMIMO* the antennas are spread out over the cell. It was shown in [41] that a distributed MaMIMO can achieve higher performance compared to co-located MaMIMO.

2.1.1 UE aided calibration and Internal calibration

There are two main approaches to reciprocity calibration based on whether or not a UE is involved in its determination.

1. In *UE aided calibration*, explicit channel feedback from a UE during the calibration phase is used to estimate the calibration parameters. Hence, during a training phase, explicit pilots are exchanged between the BS and UE over-the-air. Based on these pilots, the UE feeds back its estimate of the channel to the BS which together with its estimate of the UL channel derives the calibration parameters.
2. A second approach is to estimate only the \mathbf{F}_A up to a scale factor and not estimate the \mathbf{F}_B at all. Of course, if all the UEs have just one antenna each, \mathbf{F}_B is just a complex scalar and need not be estimated. In the general case of UEs with multiple receive antennas, the existing literature [32, 33] justifies this approach. Such an approach is called *internal calibration* or *self-calibration* where the calibration is performed entirely between the antennas of the BS. An important advantage of this kind of calibration is that it ensures tight clock and frequency synchronization amongst the antennas that are being calibrated in the case of co-located MaMIMO. The self-calibration may be performed over-the-air (OTA) or via additional hardware circuitry specifically for calibration. The OTA approach is a more popular method today and our research is focused on this topic.

2.1.2 Coherent and Non-coherent calibration scheme

The calibration parameters of the antenna may be considered to be constant in the order of several hours. However, the variation of the physical propagation channel is typically much faster.

This leads to two ways of approaching the estimation of the relative calibration parameters. We could complete the entire estimation of these parameters in a short time span where the propagation channel stays a constant. Such a time duration would be called a coherent time slot. When the estimation happens within one coherent time slot, it is called a coherent estimation scheme. Alternatively, the problem may well be formulated over several different coherent time slots (during which the calibration parameters themselves are assumed constant), and in this case, it is called non-coherent estimation. This is also illustrated in Figure 2.2.

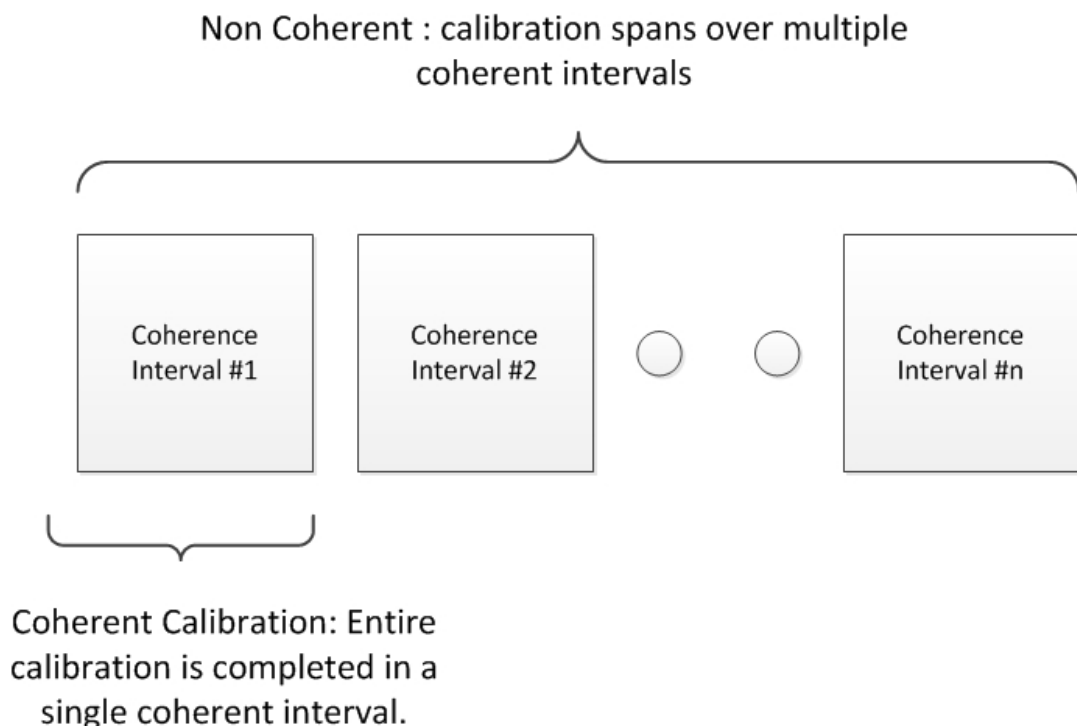


Figure 2.2: Illustration of coherent and non-coherent calibration

2.1.3 Key assumptions

1. We discuss the estimation of the reciprocity calibration factors over a narrow frequency band where the calibration factors are assumed to be a constant. In the case of wideband signals, we assume a multi-carrier system like OFDM and the estimation happens on a per sub-carrier basis.
2. It is assumed that the impact of the Tx and Rx chains may be modeled as a linear scaling factor over a narrow frequency band. This has been validated in several real implementations like [37], [35]. This can also be seen later in Chapter 6 as shown in Figure 6.6 where the performance with calibration matches that with the ideal DL channel.

3. The calibration matrix \mathbf{F} is diagonal. This was validated experimentally in [20] where the off-diagonal elements of \mathbf{F} were found to be less than 30dB compared to the diagonal elements. Note, however, that this does not necessarily imply no mutual coupling or cross-talk. If $\mathcal{M}_A, \mathcal{M}_B$ represent reciprocal non-diagonal matrices that encapsulate the mutual coupling and cross-talk, we get,

$$(2.4) \quad \begin{cases} \mathbf{H}_{A \rightarrow B} = \mathbf{R}_B (\mathcal{M}_B \mathbf{C} \mathcal{M}_A) \mathbf{T}_A, \\ \mathbf{H}_{B \rightarrow A} = \mathbf{R}_A (\mathcal{M}_A \mathbf{C}^T \mathcal{M}_B) \mathbf{T}_B. \end{cases}$$

Hence, by treating the mutual coupling and cross-talk as part of the propagation channel, we get back the diagonal calibration factors! Hence, the diagonal \mathbf{F} could be a result of either no mutual coupling or just reciprocal mutual coupling. The existing literature that uses mutual coupling to perform reciprocity calibration implicitly assumes it to be reciprocal. Only [45] considers mutual coupling as non-reciprocal. However, the same authors treat it as reciprocal in their next work [46]. In summary, however, what is important in our research is the diagonal nature of \mathbf{F} that is justified by the numerous experimental validations based on that assumption. In fact, our own experiments reported in Section 6.1.1 are in agreement with this assumption.

2.2 State of the Art

In this section, we discuss the estimation schemes available in the literature.

2.2.1 Argos

Argos was the first published Massive MIMO prototype supporting 64 antennas simultaneously serving 15 terminals [37]. This work introduced the internal calibration procedure where the calibration procedure is done exclusively at the BS without involving the UE. Transmission and reception RF chain asymmetries are modeled by scalar coefficients while RF crosstalk or mutual coupling are ignored resulting in a diagonal \mathbf{F} . The idea is to use one of the BS antennas as a reference and derive the relative calibration factors of the rest of the BS antennas relative to this reference antenna. As mentioned before, the relative calibration factor \mathbf{F} can only be estimated up to a scale factor. As the matrix \mathbf{F} is assumed to be diagonal, only the diagonal elements \mathbf{f} are relevant, where $\mathbf{f} = \text{diag}(\mathbf{F})$. The relative calibration factors of the individual antennas are denoted as f_i . Let t_i and r_i represent corresponding Tx and Rx absolute calibration parameters for the radio i , such that $f_i = \frac{t_i}{r_i}$. Then,

$$(2.5) \quad \begin{aligned} y_{i \rightarrow 0} &= r_0 c_{i \rightarrow 0} t_i p_i + n_{i \rightarrow 0}, \\ y_{0 \rightarrow i} &= r_i c_{i \rightarrow 0} t_0 p_0 + n_{0 \rightarrow i}, \end{aligned}$$

where $y_{i \rightarrow 0}$ denotes the received signal at the reference antenna from antenna i . p_i and p_0 are the transmission pilots, and $n_{i \rightarrow 0}$ denotes the noise at the reference antenna at the time of

transmission from antenna i . Note that 0 is considered to be the index for the reference antenna. The calibration procedure in the Argos system thus uses a bidirectional transmission between the reference antenna and other antennas to derive their relative calibration coefficients. Assuming the pilots to be unity, the calibration parameters are estimated as follows:

$$(2.6) \quad f_i = \frac{y_{i \rightarrow 0}}{y_{0 \rightarrow i}}.$$

However, this method is sensitive to the position of the reference antenna which can result in significant channel amplitude difference for antennas close to the reference antenna and those far away.

2.2.2 Rogalin Method

The Rogalin method [35] can be regarded as an extension of the Argos calibration. It was primarily intended for a distributed Massive MIMO system but can be equally applied to a co-located MIMO scenario. In this method, no more reference antenna is defined and the calibration is performed among different antenna element pairs.

The principle of the Rogalin method is as follows. Consider the set of all transmissions between antennas i and j that have happened in the same coherence time, and assume pilots as unity.

$$(2.7) \quad y_{i \rightarrow j} = r_j c_{i \rightarrow j} t_i + n_{i \rightarrow j}, \quad y_{j \rightarrow i} = r_i c_{i \rightarrow j}^T t_j + n_{j \rightarrow i}$$

Eliminating the propagation channel, we obtain,

$$(2.8) \quad f_i y_{j \rightarrow i} - y_{i \rightarrow j} f_j = f_i n_{j \rightarrow i} - n_{i \rightarrow j} f_j$$

The calibration coefficients can be obtained by minimizing the Least Square (LS) cost function.

$$(2.9) \quad J_{LS}(f_1, f_2, \dots, f_M) = \sum_{(i,j) \in \mathcal{S}} |f_j y_{j \rightarrow i} - f_i y_{i \rightarrow j}|^2$$

where \mathcal{S} is the set of all pairs of transmissions.

To avoid the trivial all-zeros solution, f_1 is assumed to be unity. The result can be obtained by taking derivatives w.r.t. all f_i , yielding

$$(2.10) \quad \hat{\mathbf{f}}_{2:M} = -(\mathbf{A}_1^H \mathbf{A}_1)^{-1} \mathbf{A}_1^H \mathbf{a}_1$$

where $\mathbf{A} = [\mathbf{a}_1 | \mathbf{A}_1]$, with \mathbf{a}_1 as the first column and \mathbf{A}_1 the rest of the columns. The entries of \mathbf{A} are given by

$$(2.11) \quad A_{i,j} = \begin{cases} \sum_{l:(i,l) \in \mathcal{S}} |y_{i \rightarrow l}|^2 & \text{for } j = i \\ -y_{i \rightarrow j}^* y_{j \rightarrow i} & \text{for } j \neq i, (i,j) \in \mathcal{S} \\ 0 & \text{for } j \neq i, (i,j) \notin \mathcal{S} \end{cases}$$

The Argos method can be viewed as a special case every antenna (with indices 2 till M) forms a transmission pair only with the reference antenna (element 1) at the center. The cost function is written as

$$(2.12) \quad J_{Argos}(f_1, f_2, \dots, f_M) = \sum_{j \neq 1} |f_j y_{j \rightarrow 1} - f_1 y_{1 \rightarrow j}|^2$$

By generalizing the Argos method to an LS formulation, Rogalin method gets rid of the need for a reference antenna. By involving bi-directional transmission between any radio element pairs, it outperforms the Argos method which relies only on the transmission between the reference antenna and other antenna elements. In a distributed MaMIMO setting, this work also proposes hierarchical calibration, i.e. grouping radio elements into different clusters and performing intra-cluster and inter-cluster calibration separately.

2.2.3 Avalanche

The typical estimation methods mentioned in 2.2.1 and 2.2.2 need M channel uses to complete the estimation of the calibration parameters. In other words, the time to estimate the calibration parameters is linear in the number of antennas. Avalanche [31] is a fast recursive coherent calibration method that can perform the estimation in $\mathcal{O}(\sqrt{M})$ channel uses. The algorithm successively uses already calibrated parts of the antenna array to calibrate uncalibrated radios which, once calibrated, are merged into the calibrated array. At a given point during calibration, assume M_0 radios have already been calibrated using L channel uses. Refer to this as a reference set 0 whose calibration factor is \mathbf{f}_0 . With these calibrated radios, a new set of radios M_1 will be calibrated. During the calibration process of the reference set, another antenna j belonging to the set M_1 would have received L transmissions from this reference set. The L length vector thus observed at the antenna j would be,

$$(2.13) \quad \mathbf{y}_j = \mathbf{P}^T \mathbf{T}_0 \mathbf{C}_{0 \rightarrow j} r_j + \mathbf{n}_{0 \rightarrow j}.$$

Here, \mathbf{P}^T represents the transmit pilots and $\mathbf{n}_{0 \rightarrow j}$ refers to the vector of noise observed at antenna j . Next, consider a single pilot (unity pilots) transmission from all the new M_1 radios to be calibrated. This results in an observation vector of length M_0 at the reference antennas.

$$(2.14) \quad \mathbf{y}_0 = \mathbf{R}_0 \sum_{i=1}^{M_1} \mathbf{C}_{i \rightarrow 0} t_i + \mathbf{n}_{i \rightarrow 0}.$$

Then, it is proved in this paper that if $M_1 \leq L$, the calibration factors for antenna j in this new set of radios is given by,

$$(2.15) \quad \mathbf{f}_1 = \left(\mathbf{Y}^H \mathbf{Y} \right)^{-1} \mathbf{Y}^H \mathbf{P}^T \text{diag}(\mathbf{f}_0) \mathbf{y}_0.$$

Here, $\mathbf{Y} = [\mathbf{y}_1, \mathbf{y}_2, \dots, \mathbf{y}_{M_1}]$. A key drawback of this algorithm is that of error propagation as it uses previously estimated calibration values to estimate new ones. Note, however, that at any

time instant t , the new number of antennas that can transmit would be $\max(t - 1, 1)$. Hence, the maximum number of antennas that can be transmitted with L channel uses would be $\sum_{i=2}^L \max(i - 1, 1) = \frac{(L-1)L}{2}$. Thus, the overall estimation for M antennas may be performed in $\mathcal{O}(\sqrt{M})$ channel uses. More details on this method are provided in the simulation section 2.8.

2.2.4 Method in [43]

In this work, a penalized ML based algorithm is proposed to estimate the calibration parameters. The overall received signal may be expressed as,

$$(2.16) \quad \mathbf{Y} = \mathbf{R}\mathbf{C}\mathbf{T} + \mathbf{N} = \mathbf{R}\mathbf{C}\mathbf{R}^T \mathbf{R}^{-T} \mathbf{T} + \mathbf{N} = \underbrace{\mathbf{R}\mathbf{C}\mathbf{R}^T}_{\mathcal{H}} \mathbf{F} + \mathbf{N}.$$

Here, the $(i, j)^{th}$ entry of the matrix \mathbf{Y} corresponds to the received signal at antenna j from antenna i . Hence, the diagonal entries of this matrix are undefined. \mathbf{N} corresponds to the matrix of noise observed and again has diagonal entries undefined. Denoting \mathbf{f} as the diagonal elements of \mathbf{F} , a penalized ML is then formulated as,

$$(2.17) \quad [\hat{\mathbf{f}}, \hat{\mathcal{H}}] = \arg \max_{\mathbf{f}, \mathcal{H}} \ln p(\mathbf{Y} | \mathbf{f}, \mathcal{H}) + \epsilon (\|\mathbf{f}\|^2 + \|\mathcal{H}\|^2),$$

where ϵ is an arbitrary parameter chosen to control the convergence of the algorithm. The algorithm proceeds by alternately optimizing $\hat{\mathbf{f}}$ and $\hat{\mathcal{H}}$ as follows.

$$(2.18) \quad \begin{aligned} \hat{\mathbf{h}} &= (\mathcal{F}^H \mathcal{F} + \epsilon \mathbf{I})^{-1} \mathcal{F}^H \mathbf{y}, \\ \hat{\mathbf{f}} &= (\mathcal{H}^H \mathcal{H} + 2\epsilon \mathbf{I})^{-1} \mathcal{H}^H \mathbf{y}, \end{aligned}$$

where $\mathbf{h} = \text{vec}(\mathcal{H})$, the vector operator, and $\hat{\mathbf{h}}$ is an estimate of \mathbf{h} .

This paper also derives a CRB about which we discuss later in relation to our own derivation of the CRB in section 2.4.

2.3 Group calibration System Model

Here we present a more general system model [?] that allows the grouping of multiple antennas during transmission. This model falls back to the single antenna transmission scenario when each grouping has only one antenna.

Here, as shown in 2.3, the M antennas are partitioned into G groups with M_i antennas each. Each group A_i transmits pilots \mathbf{P}_i for L_i channel uses. Let $\mathbf{Y}_{i \rightarrow j}$ be the received signal at antenna j upon transmission of pilot \mathbf{P}_i from antenna i . Then for every pair of transmission between antennas i and j (bi-directional Tx), we obtain,

$$(2.19) \quad \text{Bi-directional Tx} \left\{ \begin{aligned} \underbrace{\mathbf{Y}_{i \rightarrow j}}_{M_j \times L_i} &= \underbrace{\mathbf{R}_j}_{M_j \times M_j} \underbrace{\mathbf{C}_{i \rightarrow j}}_{M_j \times M_i} \underbrace{\mathbf{T}_i}_{M_i \times M_i} \underbrace{\mathbf{P}_i}_{M_i \times L_i} + \mathbf{N}_{i \rightarrow j}, \\ \mathbf{Y}_{j \rightarrow i} &= \mathbf{R}_i \mathbf{C}_{i \rightarrow j}^T \mathbf{T}_j \mathbf{P}_j + \mathbf{N}_{j \rightarrow i}, \end{aligned} \right.$$

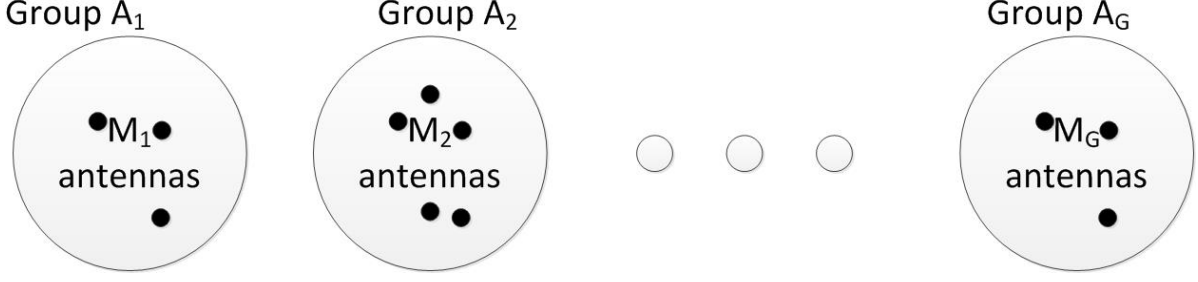


Figure 2.3: Illustration of the group calibration system model

$\mathbf{N}_{i \rightarrow j}$ represents the noise seen at antenna j when antenna i is transmitting. Equation (2.19) also shows the dimensions of the matrices involved for clarity. It is important to note that the channel is assumed to be constant during this bi-directional Tx. Eliminating the propagation channel $\mathbf{C}_{i \rightarrow j}$,

$$(2.20) \quad \mathbf{P}_i^T \mathbf{F}_i^T \mathbf{Y}_{j \rightarrow i} - \mathbf{Y}_{i \rightarrow j}^T \mathbf{F}_j \mathbf{P}_j = \mathbf{P}_i^T \mathbf{F}_i^T \mathbf{N}_{j \rightarrow i} - \mathbf{N}_{i \rightarrow j}^T \mathbf{F}_j \mathbf{P}_j,$$

where $\mathbf{F}_i = \mathbf{R}_i^{-T} \mathbf{T}_i$ and $\mathbf{F}_j = \mathbf{R}_j^{-T} \mathbf{T}_j$ are the calibration matrices for groups i and j . Using the vec operator and its properties, equation (2.20) may be rewritten as

$$(2.21) \quad \begin{aligned} \text{vec}(\mathbf{P}_i^T \mathbf{F}_i^T \mathbf{Y}_{j \rightarrow i}) &= \text{vec}(\mathbf{Y}_{i \rightarrow j}^T \mathbf{F}_j \mathbf{P}_j) + \text{vec}(\mathbf{P}_i^T \mathbf{F}_i^T \mathbf{N}_{j \rightarrow i} - \mathbf{N}_{i \rightarrow j}^T \mathbf{F}_j \mathbf{P}_j), \\ (\mathbf{Y}_{j \rightarrow i}^T \otimes \mathbf{P}_i^T) \text{vec}(\mathbf{F}_i^T) &= (\mathbf{P}_j^T \otimes \mathbf{Y}_{i \rightarrow j}^T) \text{vec}(\mathbf{F}_j^T) + \tilde{\mathbf{N}}_{ij}. \end{aligned}$$

Here, we have used the property that for any matrices $\mathbf{X}_1, \mathbf{X}_2$, and \mathbf{X}_3 ,

$$(2.22) \quad \text{vec}(\mathbf{X}_1 \mathbf{X}_2 \mathbf{X}_3) = (\mathbf{X}_3^T \otimes \mathbf{X}_1) \text{vec}(\mathbf{X}_2),$$

where \otimes denotes the Kronecker product. $\tilde{\mathbf{N}}_{ij} = \text{vec}(\mathbf{P}_i^T \mathbf{F}_i^T \mathbf{N}_{j \rightarrow i} - \mathbf{N}_{i \rightarrow j}^T \mathbf{F}_j^T \mathbf{P}_j)$. In addition, as the matrices, \mathbf{F}_i are diagonal, all the columns corresponding to the zero entries of the calibration matrices can be eliminated. Hence, (2.21) may be further rewritten as,

$$(2.23) \quad (\mathbf{Y}_{j \rightarrow i}^T * \mathbf{P}_i^T) \mathbf{f}_i - (\mathbf{P}_j^T * \mathbf{Y}_{i \rightarrow j}^T) \mathbf{f}_j = \tilde{\mathbf{N}}_{ij},$$

where $*$ denotes the Khatri-Rao product [22] (or column-wise Kronecker product). With matrices \mathbf{A} and \mathbf{B} partitioned into columns, $\mathbf{A} = [\mathbf{a}_1 \ \mathbf{a}_2 \ \dots \ \mathbf{a}_M]$ and $\mathbf{B} = [\mathbf{b}_1 \ \mathbf{b}_2 \ \dots \ \mathbf{b}_M]$ where \mathbf{a}_i and \mathbf{b}_i are column vectors for $i \in 1 \dots M$, then, $\mathbf{A} * \mathbf{B} = [\mathbf{a}_1 \otimes \mathbf{b}_1 \ \mathbf{a}_2 \otimes \mathbf{b}_2 \ \dots \ \mathbf{a}_M \otimes \mathbf{b}_M]$. Here, we have used the equality $\text{vec}(\mathbf{X}_1 \text{diag}(\mathbf{x}) \mathbf{X}_3) = (\mathbf{X}_3^T * \mathbf{X}_1) \mathbf{x}$. \mathbf{f}_i refers to the diagonal elements of the matrix \mathbf{F}_i .

2.3.1 Least Squares Solution

Collecting all these bi-directional transmissions, we arrive at a least-squares formulation to solve for the relative calibration factors \mathbf{f} .

$$(2.24) \quad \hat{\mathbf{f}} = \arg \min_{\mathbf{f}} \sum_{i,j \in \mathcal{G}} \|(\mathbf{Y}_{j \rightarrow i}^T * \mathbf{P}_i^T) \mathbf{f}_i - (\mathbf{P}_j^T * \mathbf{Y}_{i \rightarrow j}^T) \mathbf{f}_j\|^2,$$

where \mathcal{G} defines the set of all bi-directional transmissions. Of course, this needs to be augmented with a constraint,

$$(2.25) \quad \mathcal{C}(\hat{\mathbf{f}}, \mathbf{f}) = 0,$$

in order to exclude the trivial solution $\hat{\mathbf{f}} = \mathbf{0}$ in (2.24). The constraint on $\hat{\mathbf{f}}$ may depend on the true parameters \mathbf{f} . As we shall see further this constraint needs to be complex valued (which represents two real constraints). Typical choices for the constraint are

1) Norm plus phase constraint (NPC):

$$(2.26) \quad \text{norm: } \text{Re}\{\mathcal{C}(\hat{\mathbf{f}}, \mathbf{f})\} = \|\hat{\mathbf{f}}\|^2 - c, \quad c = \|\mathbf{f}\|^2,$$

$$(2.27) \quad \text{phase: } \text{Im}\{\mathcal{C}(\hat{\mathbf{f}}, \mathbf{f})\} = \text{Im}\{\hat{\mathbf{f}}^H \mathbf{f}\} = 0.$$

2) Linear constraint:

$$(2.28) \quad \mathcal{C}(\hat{\mathbf{f}}, \mathbf{f}) = \hat{\mathbf{f}}^H \mathbf{g} - c = 0.$$

If we choose the vector $\mathbf{g} = \mathbf{f}$ and $c = \|\mathbf{f}\|^2$, then the $\text{Im}\{\cdot\}$ part of equation (2.28) corresponds to (2.27). The most popular linear constraint is the First Coefficient Constraint (FCC), which is (2.28) with $\mathbf{g} = \mathbf{e}_1$, $c = 1$.

2.3.2 Fast Calibration

Here, we consider a coherent calibration scheme and derive parameters for the group calibration that result in the estimation of the relative calibration factors \mathbf{f} using the minimum number of channel uses. Consider a scheme where every antenna group A_i transmits pilots \mathbf{P}_i in a round robin fashion. Once all the subgroups have transmitted, we will get the following structure by stacking the individual equations. Consider the following sequence

- When group 2 transmits, we can formulate $L_2 L_1$ number of equations.
- When group 3 transmits, we can formulate $L_3 L_1 + L_3 L_2$ number of equations.
- When group i transmits, we can formulate $\sum_{j=1}^{i-1} L_i L_j$ number of equations.
- Thus, the total number of equations after all the groups transmit is $\sum_{i=1}^G \sum_{j=1}^{i-1} L_i L_j$.

This process continues until group G finishes its transmission. During this process of transmission by the G antenna groups, we can start forming equations as indicated, that can be solved recursively for subsets of unknown calibration parameters, or we can wait until all equations are formed to solve the problem jointly. Finally, stacking equations (2.23) for all $1 \leq i < j \leq G$ yields

$$(2.29) \quad \mathcal{Y}(\mathbf{P})\mathbf{f} = \tilde{\mathbf{n}},$$

where,

$$(2.30) \quad \mathcal{Y}(\mathbf{P}) = \underbrace{\begin{bmatrix} (\mathbf{Y}_{2 \rightarrow 1}^T * \mathbf{P}_1^T) & -(\mathbf{P}_2^T * \mathbf{Y}_{1 \rightarrow 2}^T) & 0 & \dots \\ (\mathbf{Y}_{3 \rightarrow 1}^T * \mathbf{P}_1^T) & 0 & -(\mathbf{P}_3^T * \mathbf{Y}_{1 \rightarrow 3}^T) & \dots \\ 0 & (\mathbf{Y}_{3 \rightarrow 2}^T * \mathbf{P}_2^T) & -(\mathbf{P}_3^T * \mathbf{Y}_{2 \rightarrow 3}^T) & \dots \\ \vdots & \vdots & \vdots & \ddots \end{bmatrix}}_{\left(\sum_{j=2}^G \sum_{i=1}^{j-1} L_i L_j\right) \times M}.$$

$\tilde{\mathbf{n}}$ represents the stacked form of the noise components. By independence of the rows, we can state that the problem is fully determined if and only if,

$$(2.31) \quad \sum_{1 \leq i < j \leq G} L_j L_i \geq M - 1.$$

We address the problem of finding the smallest number of groups enabling calibration of the whole array while ensuring identifiability at each step, by finding the best choices for the L_i in order to see to what extent optimizing the group based calibration can speed up the calibration process. Let us consider the case where the total number of channel uses available for calibration is fixed to K . We derive the number of pilot transmissions for each group, L_1, \dots, L_G , that would maximize the total number of antennas that can be calibrated, i.e.,

$$(2.32) \quad \max_{(L_1, \dots, L_G)} \left[\sum_{j=2}^G \sum_{i=1}^{j-1} L_j L_i + 1 \right], \text{ subject to } \sum_{i=1}^G L_i = K.$$

Form the Lagrangian,

$$(2.33) \quad \sum_{i=1}^G \sum_{j=1}^{i-1} L_i L_j + 1 + \lambda \left(\sum_{i=1}^G L_i - K \right)$$

Differentiating with respect to L_p , the number of pilot transmissions for the group p , we get

$$(2.34) \quad \begin{aligned} \sum_{j=1}^{p-1} L_j + \sum_{i=p+1}^G L_i + \lambda &= 0, & \sum_{i=1}^G L_i - L_p + \lambda &= 0 \\ K - L_p + \lambda &= 0, & L_p &= K + \lambda \end{aligned}$$

Using $\sum_{i=1}^G L_i = K$, we get $L_p = \frac{K}{G}$, independent of p . This implies that every group transmits for the same number of time instants, L . Thus, the maximum number of antennas that can be calibrated using LG time instants is $\frac{1}{2}L^2G(G-1) + 1$.

$$(2.35) \quad \begin{aligned} M &= \frac{1}{2}L^2G(G-1) + 1 \quad \text{subject to } LG = K \\ &= \frac{1}{2}L^2 \left(\frac{K}{L} \right) \left(\frac{K}{L} - 1 \right) + 1 \\ &= \frac{1}{2}K(K-L) + 1 \end{aligned}$$

Scenario	Number of channel uses	Number of Antennas that can be calibrated
	$\sum_{i=1}^G L_i$	$(\sum_{i=1}^G \sum_{j=1}^{i-1} L_i L_j) + 1$
$L_i = L$	LG	$\frac{1}{2}L^2G(G-1) + 1$
$L_i = L = 1$	G	$\frac{1}{2}G(G-1) + 1$

Table 2.1: The number of channel uses required for calibration

From equation (2.35), it is clear that to maximize the number of antennas that can be calibrated, $L = 1$. However, while the above results are correct, the derivation as shown above is not appropriate to optimize a discrete parameter. The correct derivation was provided by the second author in the Appendix of [?].

2.3.3 Non-coherent estimation

We would like to remark that (2.24) applies to any set of bi-directional transmissions. In contrast to fast calibration, it is often interesting to perform these transmissions across many independent coherent time slots (non-coherent calibration scheme). This could either be because the channel coherence time is not sufficient to complete the calibration estimation or simply because the BS would like to perform the calibration process with minimal interruption to the data transmission. In the non-coherent case, the key difference is that the propagation channel becomes a function of the coherent timeslot t . Specifically, the equation (2.19) would be modified as,

$$(2.36) \quad \text{Bi-directional Tx} \begin{cases} \mathbf{Y}_{i \rightarrow j}(t) = \mathbf{R}_j \mathbf{C}_{i \rightarrow j}(t) \mathbf{T}_i \mathbf{P}_i(t) + \mathbf{N}_{i \rightarrow j}(t), \\ \mathbf{Y}_{j \rightarrow i}(t) = \mathbf{R}_i \mathbf{C}_{i \rightarrow j}^T(t) \mathbf{T}_j \mathbf{P}_j(t) + \mathbf{N}_{j \rightarrow i}(t). \end{cases}$$

Here $t \in [1 \ 2 \ \dots \ T]$ denotes a particular coherent time slot and T is the total number of coherent time slots used for estimating the calibration parameters. Proceeding as before, the non-coherent estimator would be obtained as,

$$(2.37) \quad \begin{aligned} \hat{\mathbf{f}} &= \arg \min_{\mathbf{f}} \sum_{t=1}^T \sum_{\substack{i, j \in \mathcal{G}(t) \\ i \neq j}} \left\| \left(\mathbf{Y}_{j \rightarrow i}^T(t) * \mathbf{P}_i^T(t) \right) \mathbf{f}_i - \left(\mathbf{P}_j^T(t) * \mathbf{Y}_{i \rightarrow j}^T(t) \right) \mathbf{f}_j \right\|^2 \\ &= \arg \min_{\mathbf{f}} \|\mathcal{Y}(\mathbf{P})\mathbf{f}\|^2, \end{aligned}$$

It is advantageous to consider a non-coherent scenario as it includes as a special case, the coherent scenario. Hence, in the following section, CRB is derived for a non-coherent setting.

2.4 Cramer Rao Bound

We discuss the CRB computation for the non-coherent reciprocity calibration over T coherent time slots. The non-coherent case reduces to the coherent case when there is just one coherent time

slot being considered and bi-directional transmissions between all the antennas can be completed within this time slot. Note that while the channel can vary across the different coherent time slots, the calibration factors vary more slowly and remain a constant across all the coherent slots. Consider a coherent time slot, t , where a set of bi-directional transmissions are performed. From (2.19), we have,

$$(2.38) \quad \mathbf{Y}_{i \rightarrow j}(t) = \underbrace{\mathbf{R}_j \mathbf{C}_{i \rightarrow j}(t) \mathbf{R}_i^T}_{\mathcal{H}_{i \rightarrow j}(t)} \mathbf{F}_i \mathbf{P}_i(t) + \mathbf{N}_{i \rightarrow j}(t).$$

We define $\mathcal{H}_{i \rightarrow j}(t) = \mathbf{R}_j \mathbf{C}_{i \rightarrow j}(t) \mathbf{R}_i^T$ to be an auxiliary internal channel (not corresponding to any physically measurable quantity) that appears as a nuisance parameter in the estimation of the calibration parameters. Note that the auxiliary channel $\mathcal{H}_{i \rightarrow j}(t)$ inherits the reciprocity from the channel $\mathbf{C}_{i \rightarrow j}(t)$: $\mathcal{H}_{i \rightarrow j}(t) = \mathcal{H}_{j \rightarrow i}^T(t)$. Upon applying the vectorization operator for each bidirectional transmission between groups i and j , we have, similarly to (2.29),

$$(2.39) \quad \text{vec}(\mathbf{Y}_{i \rightarrow j}(t)) = \left(\mathbf{P}_i^T(t) * \mathcal{H}_{i \rightarrow j}(t) \right) \mathbf{f}_i + \text{vec}(\mathbf{N}_{i \rightarrow j}(t)).$$

In the reverse direction, using $\mathcal{H}_{i \rightarrow j}(t) = \mathcal{H}_{j \rightarrow i}^T(t)$, we have

$$(2.40) \quad \text{vec}(\mathbf{Y}_{j \rightarrow i}^T(t)) = \left(\mathcal{H}_{i \rightarrow j}^T(t) * \mathbf{P}_j^T(t) \right) \mathbf{f}_j + \text{vec}(\mathbf{N}_{j \rightarrow i}^T(t)).$$

Alternatively, (2.39) and (2.40) may also be written as

$$(2.41) \quad \begin{cases} \text{vec}(\mathbf{Y}_{i \rightarrow j}(t)) = \left[(\mathbf{F}_i \mathbf{P}_i(t))^T \otimes \mathbf{I} \right] \text{vec}(\mathcal{H}_{i \rightarrow j}(t)) + \text{vec}(\mathbf{N}_{i \rightarrow j}(t)) \\ \text{vec}(\mathbf{Y}_{j \rightarrow i}^T(t)) = \left[\mathbf{I} \otimes (\mathbf{P}_j^T(t) \mathbf{F}_j) \right] \text{vec}(\mathcal{H}_{i \rightarrow j}(t)) + \text{vec}(\mathbf{N}_{j \rightarrow i}^T(t)). \end{cases}$$

In the case of non-coherent calibration, the key point is to pick only bi-directional transmissions that happen every coherent time slot. Stacking all the bi-directional observations into a vector, $\mathbf{y}(t) = [\text{vec}(\mathbf{Y}_{1 \rightarrow 2}(t))^T \text{vec}(\mathbf{Y}_{2 \rightarrow 1}^T(t))^T \text{vec}(\mathbf{Y}_{1 \rightarrow 3}(t))^T \dots]^T$, the above two alternative formulations can be summarized into,

$$(2.42) \quad \mathbf{y}(t) = \mathcal{H}(\mathbf{h}(t), \mathbf{P}(t), t) \mathbf{f} + \mathbf{n} = \mathcal{F}(\mathbf{f}, \mathbf{P}(t), t) \mathbf{h}(t) + \mathbf{n},$$

where $\mathbf{h}(t) = [\text{vec}(\mathcal{H}_{1 \rightarrow 2})^T \text{vec}(\mathcal{H}_{1 \rightarrow 3})^T \text{vec}(\mathcal{H}_{2 \rightarrow 3})^T \dots]^T$, and \mathbf{n} is the corresponding noise vector. The pilot matrix \mathbf{P} is different across different coherent time slots, but to simplify the notation, we omit the explicit dependence on t where there is no room for confusion. The composite matrices $\mathcal{H}(\mathbf{h}(t), \mathbf{P}, t)$ and $\mathcal{F}(\mathbf{f}, \mathbf{P}, t)$ are given below for an example scenario, where, in t^{th} time slot, the

bi-directional transmissions happened between the antenna groups 1, 2 and 3.

$$(2.43) \quad \mathcal{H}(\mathbf{h}(t), \mathbf{P}, t) = \begin{bmatrix} \mathbf{P}_1^T * \mathcal{H}_{1 \rightarrow 2} & 0 & 0 \\ 0 & \mathcal{H}_{1 \rightarrow 2}^T * \mathbf{P}_2^T & 0 \\ \mathbf{P}_1^T * \mathcal{H}_{1 \rightarrow 3} & 0 & 0 \\ 0 & 0 & \mathcal{H}_{1 \rightarrow 3}^T * \mathbf{P}_3^T \\ 0 & \mathcal{H}_{3 \rightarrow 2}^T * \mathbf{P}_2^T & 0 \\ 0 & 0 & \mathcal{H}_{2 \rightarrow 3}^T * \mathbf{P}_3^T \end{bmatrix}$$

$$\mathcal{F}(\mathbf{f}, \mathbf{P}, t) = \begin{bmatrix} \mathbf{P}_1^T \mathbf{F}_1 \otimes \mathbf{I} & 0 & 0 \\ \mathbf{I} \otimes \mathbf{P}_2^T \mathbf{F}_2 & 0 & 0 \\ 0 & \mathbf{P}_1^T \mathbf{F}_1 \otimes \mathbf{I} & 0 \\ 0 & \mathbf{I} \otimes \mathbf{P}_3^T \mathbf{F}_3 & 0 \\ 0 & 0 & \mathbf{P}_2^T \mathbf{F}_2 \otimes \mathbf{I} \\ 0 & 0 & \mathbf{I} \otimes \mathbf{P}_3^T \mathbf{F}_3 \end{bmatrix}.$$

Stacking these equations over all T coherent time slots, we get,

$$(2.44) \quad \mathbf{y} = \underbrace{\begin{bmatrix} \mathcal{H}(\mathbf{h}(1), \mathbf{P}, 1) \\ \vdots \\ \mathcal{H}(\mathbf{h}(T), \mathbf{P}, T) \end{bmatrix}}_{\mathcal{H}(\mathbf{h}, \mathbf{P})} \mathbf{f} + \mathbf{n} = \underbrace{\begin{bmatrix} \mathcal{F}(\mathbf{f}, \mathbf{P}, 1) & 0 & 0 \\ 0 & \ddots & 0 \\ 0 & 0 & \mathcal{F}(\mathbf{f}, \mathbf{P}, T) \end{bmatrix}}_{\mathcal{F}(\mathbf{f}, \mathbf{P})} \underbrace{\begin{bmatrix} \mathbf{h}(1) \\ \vdots \\ \mathbf{h}(T) \end{bmatrix}}_{\mathbf{h}} + \mathbf{n}$$

$$= \mathcal{H}(\mathbf{h}, \mathbf{P})\mathbf{f} + \mathbf{n} = \mathcal{F}(\mathbf{f}, \mathbf{P})\mathbf{h} + \mathbf{n}.$$

Here, $\mathcal{F}(\mathbf{f}, \mathbf{P})$ is a block diagonal matrix whose diagonal block t is $\mathcal{F}(\mathbf{f}, \mathbf{P}, t)$. The scenario is now identical to that encountered in some blind channel estimation scenarios and hence we can take advantage of some existing tools [4],[3], which we exploit next.

Treating \mathbf{h} and \mathbf{f} as deterministic unknown parameters, and assuming that the receiver noise \mathbf{n} is distributed as $\mathcal{CN}(0, \sigma^2 \mathbf{I})$, the Fisher Information Matrix (FIM) \mathbf{J} for jointly estimating \mathbf{f} and \mathbf{h} can immediately be obtained from (2.42) as

$$(2.45) \quad \mathbf{J} = \frac{1}{\sigma^2} \begin{bmatrix} \mathcal{H}^H \\ \mathcal{F}^H \end{bmatrix} \begin{bmatrix} \mathcal{H} & \mathcal{F} \end{bmatrix}.$$

The computation of the CRB requires \mathbf{J} to be non-singular. However, for the problem at hand, \mathbf{J} is inherently singular. To determine the CRB when the FIM is singular, constraints have to be added to regularize the estimation problem. As the calibration parameters are complex, one complex constraint corresponds to two real constraints. Further, we are only interested in the CRB for \mathbf{f} in the presence of the nuisance parameters \mathbf{h} . Hence we are only interested in the (1, 1) block of the inverse of the 2×2 block matrix \mathbf{J} in (2.45). Incorporating the effect of the constraint (2.25) on \mathbf{f} , we can derive from [6] the following constrained CRB for \mathbf{f} :

$$(2.46) \quad \text{CRB}_{\mathbf{f}} = \sigma^2 \mathcal{V}_{\mathbf{f}} \left(\mathcal{V}_{\mathbf{f}}^H \mathcal{H}^H \mathcal{D}_{\mathcal{F}}^{\perp} \mathcal{H} \mathcal{V}_{\mathbf{f}} \right)^{-1} \mathcal{V}_{\mathbf{f}}^H.$$

Here, $\mathcal{P}_{\mathcal{X}} = \mathcal{X}(\mathcal{X}^H \mathcal{X})^\dagger \mathcal{X}^H$ and $\mathcal{P}_{\mathcal{X}}^\perp = \mathbf{I} - \mathcal{P}_{\mathcal{X}}$ are the projection operators on respectively the column space of matrix \mathcal{X} and its orthogonal complement, and \dagger corresponds to the Moore-Penrose inverse. The $M \times (M-1)$ matrix $\mathcal{V}_{\mathbf{f}}$ is such that its column space spans the orthogonal complement of that of $\frac{\partial \mathcal{L}(f)}{\partial \mathbf{f}^*}$, i.e., $\mathcal{P}_{\mathcal{V}_{\mathbf{f}}} = \mathcal{P}_{\frac{\partial \mathcal{L}}{\partial \mathbf{f}^*}}^\perp$. For example, in the FCC case, $\frac{\partial \mathcal{L}(f)}{\partial \mathbf{f}^*} = \mathbf{g} = \mathbf{e}_1$, where \mathbf{e}_1 is the first column of the Identity matrix. Hence, $\mathcal{V}_{\mathbf{f}}$ would be the orthogonal complement of this matrix which would be the remaining columns of the Identity matrix.

We now make a few remarks to compare our CRB derivation with another work [43] that derives the CRB for a single antenna scenario where transmission happens one antenna at a time. In [43], the relative calibration factors are derived from the absolute Tx and Rx side calibration parameters, which become identifiable because a model is introduced for the internal propagation channel. The internal channel is modeled as Gaussian with the mean taken as the line of sight (LoS) component (distance induced delay and attenuation) and the non-LoS (NLOS) components are assumed to result in a scaled identity covariance matrix. The NLOS components are assumed to be 60dB below the mean channel power. This implies an almost deterministic prior for the (almost known) channel and would result in underestimation of the CRB, as noted in their own work [43, Sec. III-E-2]. In short, the CRB derivation in [43] has a strong assumption on the knowledge of the channel. Our CRB derivation, on the other hand, can handle both single antenna transmissions and group transmissions and treats the internal channel as an unknown nuisance parameter. Treating the internal channel in this manner is the right approach as it reflects the real-world scenario.

2.5 Optimal Algorithms

In this section, we propose some optimal estimators. First, a maximum likelihood (ML) approach, and later a Variational Bayes (VB) based approach.

2.5.1 Alternating Maximum Likelihood (AML)

From (2.42) we get the negative log-likelihood up to an additive constant, as

$$(2.47) \quad \frac{1}{\sigma^2} \|\mathbf{y} - \mathcal{H}(\mathbf{h}, \mathbf{P})\mathbf{f}\|^2 = \frac{1}{\sigma^2} \|\mathbf{y} - \mathcal{F}(\mathbf{f}, \mathbf{P})\mathbf{h}\|^2.$$

The maximum likelihood estimator of (\mathbf{h}, \mathbf{f}) , obtained by minimizing (2.47), can be computed using alternating optimization on \mathbf{h} and \mathbf{f} , which leads to a sequence of quadratic problems. As a result, for a given \mathbf{f} , we find $\hat{\mathbf{h}} = (\mathcal{F}^H \mathcal{F})^{-1} \mathcal{F}^H \mathbf{y}$ and for a given \mathbf{h} , we find $\hat{\mathbf{f}} = (\mathcal{H}^H \mathcal{H})^{-1} \mathcal{H}^H \mathbf{y}$. This leads to the Alternating Maximum Likelihood (AML) algorithm (Algorithm 1) [3, 4] which iteratively maximizes the likelihood by alternating between the desired parameters \mathbf{f} and the nuisance parameters \mathbf{h} for the formulation (2.42).

Algorithm 1 Alternating maximum likelihood (AML)

- 1: **Initialization:** Initialize $\hat{\mathbf{f}}$ using existing calibration methods (e.g. the method in 2.2) or as a vector of all 1's.
 - 2: **repeat**
 - 3: Construct \mathcal{F} as in (2.43) using $\hat{\mathbf{f}}$.
 $\hat{\mathbf{h}} = (\mathcal{F}^H \mathcal{F})^{-1} \mathcal{F}^H \tilde{\mathbf{y}}$
 - 4: Construct \mathcal{H} as in (2.43) using $\hat{\mathbf{h}}$.
 $\hat{\mathbf{f}} = (\mathcal{H}^H \mathcal{H})^{-1} \mathcal{H}^H \tilde{\mathbf{y}}$
 - 5: **until** the difference in the calculated $\hat{\mathbf{f}}$ between two iterations is small enough.
-

2.5.2 Variational Bayes approach

In Variational Bayes (VB), a Bayesian estimate is obtained by computing an approximation to the posterior distribution of the parameters \mathbf{h}, \mathbf{f} with priors $\mathbf{f} \sim \mathcal{CN}(0, \alpha^{-1} \mathbf{I}_M)$, $\mathbf{h} \sim \mathcal{CN}(0, \beta^{-1} \mathbf{I}_{N_h})$ and α, β are assumed to have themselves a uniform prior. N_h is the number of elements in \mathbf{h} . This approximation, called the variational distribution, is chosen to minimize the Kullback-Leibler distance between the true posterior distribution $p(\mathbf{h}, \mathbf{f}, \alpha, \beta | \mathbf{y})$ and a factored variational distribution

$$(2.48) \quad q_{\mathbf{h}}(\mathbf{h}) q_{\mathbf{f}}(\mathbf{f}) q_{\alpha}(\alpha) q_{\beta}(\beta).$$

The factors can be obtained in an alternating fashion as,

$$(2.49) \quad \ln(q_{\psi_i}(\psi_i)) = \langle \ln p(\mathbf{y}, \mathbf{h}, \mathbf{f}, \alpha, \beta) \rangle_{k \neq i} + c_i,$$

where ψ_i refers to the i^{th} block of $\psi = [\mathbf{h}, \mathbf{f}, \alpha, \beta]$ and $\langle \rangle_{k \neq i}$ represents the expectation operator over the distributions q_{ψ_k} for all $k \neq i$. c_i is a normalizing constant. The log likelihood,

$$(2.50) \quad \begin{aligned} \ln p(\mathbf{y}, \mathbf{h}, \mathbf{f}, \alpha, \beta) &= \ln p(\mathbf{y} | \mathbf{h}, \mathbf{f}, \alpha, \beta) + \ln p(\mathbf{f} | \alpha) + \ln p(\mathbf{h} | \beta) \\ &= -N_y \ln \sigma^2 - \frac{1}{\sigma^2} \|\mathbf{y} - \mathcal{H} \mathbf{f}\|^2 + M \ln \alpha - \alpha \|\mathbf{f}\|^2 \\ &\quad + N_h \ln \beta - \beta \|\mathbf{h}\|^2 + c. \end{aligned}$$

Here, N_y refers to the number of elements in \mathbf{y} and c is a constant. We shall assume $\sigma^2 = 1$ and as known. It is straightforward to see that proceeding as in equation (2.49), α, β would have a Gamma distribution with mean $\langle \alpha \rangle = \frac{M}{\langle \|\mathbf{f}\|^2 \rangle}$ and $\langle \beta \rangle = \frac{N_h}{\langle \|\mathbf{h}\|^2 \rangle}$. On the other hand (taking only relevant terms),

$$(2.51) \quad \begin{aligned} \ln q_{\mathbf{f}}(\mathbf{f}) &= \mathbf{f}^H \langle \mathcal{H}^H \rangle \mathbf{y} - \mathbf{f}^H \langle \mathcal{H}^H \mathcal{H} \rangle \mathbf{f} - \langle \alpha \rangle \mathbf{f}^H \mathbf{f} \\ \ln q_{\mathbf{h}}(\mathbf{h}) &= \mathbf{h}^H \langle \mathcal{F}^H \rangle \mathbf{y} - \mathbf{h}^H \langle \mathcal{F}^H \mathcal{F} \rangle \mathbf{h} - \langle \beta \rangle \mathbf{h}^H \mathbf{h} \end{aligned}$$

This implies that $\mathbf{f} \sim \mathcal{CN}(\hat{\mathbf{f}}, \mathbf{C}_{\hat{\mathbf{f}}})$ and $\mathbf{h} \sim \mathcal{CN}(\hat{\mathbf{h}}, \mathbf{C}_{\hat{\mathbf{h}}})$. The overall algorithm may now be summarized as in Algorithm 2.

Algorithm 2 Variational Bayes Estimation of calibration parameters

- 1: **Initialization:** Initialize $\hat{\mathbf{f}}$ using existing calibration methods. Use this estimate to determine $\hat{\mathbf{h}}, \langle \alpha \rangle, \langle \beta \rangle$.
 - 2: **repeat**
 - 3: $\langle \mathcal{H}^H \mathcal{H} \rangle = \mathcal{H}^H(\hat{\mathbf{h}})\mathcal{H}(\hat{\mathbf{h}}) + \langle \mathcal{H}^H(\tilde{\mathbf{h}})\mathcal{H}(\tilde{\mathbf{h}}) \rangle$
 - 4: $\hat{\mathbf{f}} = (\langle \mathcal{H}^H \mathcal{H} \rangle + \langle \alpha \rangle \mathbf{I})^{-1} \langle \mathcal{H}^H \rangle \mathbf{y}$
 - 5: $\mathbf{C}_{\tilde{\mathbf{f}}\tilde{\mathbf{f}}} = (\langle \mathcal{H}^H \mathcal{H} \rangle + \langle \alpha \rangle \mathbf{I})^{-1}$
 - 6: $\langle \mathcal{F}^H \mathcal{F} \rangle = \mathcal{F}^H(\hat{\mathbf{f}})\mathcal{F}(\hat{\mathbf{f}}) + \langle \mathcal{F}^H(\tilde{\mathbf{f}})\mathcal{F}(\tilde{\mathbf{f}}) \rangle$
 - 7: $\hat{\mathbf{h}} = (\langle \mathcal{F}^H \mathcal{F} \rangle + \langle \beta \rangle \mathbf{I})^{-1} \langle \mathcal{F}^H \rangle \mathbf{y}$
 - 8: $\mathbf{C}_{\tilde{\mathbf{h}}\tilde{\mathbf{h}}} = (\langle \mathcal{F}^H \mathcal{F} \rangle + \langle \beta \rangle \mathbf{I})^{-1}$
 - 9: $\langle \alpha \rangle = \frac{M}{\langle \|\mathbf{f}\|^2 \rangle}, \langle \|\mathbf{f}\|^2 \rangle = \hat{\mathbf{f}}^H \hat{\mathbf{f}} + \text{tr}\{\mathbf{C}_{\tilde{\mathbf{f}}\tilde{\mathbf{f}}}\}.$
 - 10: $\langle \beta \rangle = \frac{N_h}{\langle \|\mathbf{h}\|^2 \rangle}, \langle \|\mathbf{h}\|^2 \rangle = \hat{\mathbf{h}}^H \hat{\mathbf{h}} + \text{tr}\{\mathbf{C}_{\tilde{\mathbf{h}}\tilde{\mathbf{h}}}\}.$
 - 11: **until** convergence.
-

When $G = M$, $\mathbf{C}_{\tilde{\mathbf{f}}\tilde{\mathbf{f}}}$ and $\mathbf{C}_{\tilde{\mathbf{h}}\tilde{\mathbf{h}}}$ are diagonal and $\langle \mathcal{F}^H(\tilde{\mathbf{f}})\mathcal{F}(\tilde{\mathbf{f}}) \rangle, \langle \mathcal{H}^H(\tilde{\mathbf{h}})\mathcal{H}(\tilde{\mathbf{h}}) \rangle$ can be computed easily (diagonal). However, when $G < M$, these matrices are block diagonal. To simplify the computation, we propose the following,

$$(2.52) \quad \begin{aligned} \mathbf{C}_{\tilde{\mathbf{f}}\tilde{\mathbf{f}}} &\approx \frac{\text{tr}\left\{(\langle \mathcal{H}^H \mathcal{H} \rangle + \langle \alpha \rangle \mathbf{I})^{-1}\right\}}{M} \mathbf{I}_M \\ \mathbf{C}_{\tilde{\mathbf{h}}\tilde{\mathbf{h}}} &\approx \frac{\text{tr}\left\{(\langle \mathcal{F}^H \mathcal{F} \rangle + \langle \beta \rangle \mathbf{I})^{-1}\right\}}{N_h} \mathbf{I}_{N_h}. \end{aligned}$$

We call this approach EC-VB (Expectation consistent [30] VB). Note here that by forcing the matrices $\mathbf{C}_{\tilde{\mathbf{f}}\tilde{\mathbf{f}}}, \mathbf{C}_{\tilde{\mathbf{h}}\tilde{\mathbf{h}}}$ to zero and α, β to zero, this algorithm reduces to the Alternating Maximum Likelihood (AML) algorithm [3, 4] which iteratively maximizes the likelihood by alternating between the desired parameters \mathbf{f} and the nuisance parameters \mathbf{h} for the formulation (2.42). The penalized ML method used in [43] uses quadratic regularization terms for both \mathbf{f} and \mathbf{h} which can be interpreted as Gaussian priors and which may improve estimation in ill-conditioned cases. In our case, we arrive at a similar solution from the VB perspective and more importantly, the regularization terms are optimally tuned.

2.6 Maximum likelihood vs. least squares

At first, it would seem that the ML and CRB formulations above are unrelated to the LS method used in most existing works. However, consider again the bi-directional received signal in a pair (i, j) as in equation (2.36). Eliminating the common propagation channel, we get the elementary equation for the LS method (2.37). Using this, along with equation (2.44), one obtains

$$(2.53) \quad \mathcal{Y}(\mathbf{P})\mathbf{f} = \mathcal{F}^{\perp H} \mathbf{y} = \tilde{\mathbf{n}},$$

where

$$(2.54) \quad \mathcal{F}^\perp = \begin{bmatrix} \mathbf{I} \otimes (\mathbf{F}_2 \mathbf{P}_2)^* & 0 & 0 & 0 & \dots \\ -(\mathbf{F}_1 \mathbf{P}_1)^* \otimes \mathbf{I} & 0 & 0 & 0 & \dots \\ 0 & \mathbf{I} \otimes (\mathbf{F}_3 \mathbf{P}_3)^* & 0 & 0 & \dots \\ 0 & -(\mathbf{F}_1 \mathbf{P}_1)^* \otimes \mathbf{I} & 0 & 0 & \dots \\ 0 & 0 & \mathbf{I} \otimes (\mathbf{F}_3 \mathbf{P}_3)^* & 0 & \dots \\ 0 & 0 & -(\mathbf{F}_2 \mathbf{P}_2)^* \otimes \mathbf{I} & 0 & \dots \\ \vdots & \vdots & \vdots & \vdots & \ddots \end{bmatrix},$$

such that the column space of \mathcal{F}^\perp corresponds to the orthogonal complement of the column space of \mathcal{F} (see Appendix A) assuming that either $M_i \geq L_i$ or $L_i \geq M_i$ for all $1 \leq i \leq G$.

Now, the ML criterion in (2.47) is separable in \mathbf{f} and \mathbf{h} . Optimizing (2.47) w.r.t. \mathbf{h} leads to $\hat{\mathbf{h}} = (\mathcal{F}^H \mathcal{F})^\dagger \mathcal{F}^H \mathbf{y}$ as mentioned earlier. Substituting this estimate for \mathbf{h} into (2.47) yields a ML estimator $\hat{\mathbf{f}}$ minimizing

$$(2.55) \quad \mathbf{y}^H \mathcal{D}_{\mathcal{F}}^\perp \mathbf{y} = \mathbf{y}^H \mathcal{D}_{\mathcal{F}^\perp} \mathbf{y} = \mathbf{y}^H \mathcal{F}^\perp (\mathcal{F}^{\perp H} \mathcal{F}^\perp)^\dagger \mathcal{F}^{\perp H} \mathbf{y},$$

where we used $\mathcal{D}_{\mathcal{F}}^\perp = \mathcal{D}_{\mathcal{F}^\perp}$. This should be compared to the least-squares method which consists in minimizing $\|\mathcal{F}^{\perp H} \mathbf{y}\|^2 = \|\mathcal{Y} \mathbf{f}\|^2$.

$$(2.56) \quad \|\mathcal{Y} \mathbf{f}\|^2 = \|\mathcal{F}^{\perp H} \mathbf{y}\|^2 = \mathbf{y}^H \mathcal{F}^\perp \mathcal{F}^{\perp H} \mathbf{y},$$

Hence (2.55) can be interpreted as an optimally weighted least-squares method since from (2.42) $\mathcal{F}^{\perp H} \mathbf{y} = \mathcal{F}^{\perp H} \mathbf{n} = \tilde{\mathbf{n}}$ leads to colored noise with covariance matrix $\sigma^2 \mathcal{F}^{\perp H} \mathcal{F}^\perp$. It is not clear though whether accounting for the optimal weighting in ML would lead to significant gains in performance. The weighting matrix (before inversion) $\mathcal{F}^{\perp H} \mathcal{F}^\perp$ is block diagonal with a square block corresponding to the pair of antenna groups (i, j) being of dimension $L_i L_j$. If all $L_i = 1$, then $\mathcal{F}^{\perp H} \mathcal{F}^\perp$ is a diagonal matrix. If furthermore all $M_i = 1$ (groups of isolated antennas), all pilots are of equal magnitude, and if all calibration factors would be of equal magnitude, then $\mathcal{F}^{\perp H} \mathcal{F}^\perp$ would be just a multiple of identity and hence would not represent any weighting. In any case, the fact that the CRB derived above and the ML and LS methods are all based on the signal model (2.42) shows that the CRB derived in section 2.4 is the appropriate CRB for the estimation methods discussed here.

2.7 Analysis of least squares methods

In this section, we analyze the mean square error for the LS estimator and compare it with the CRB. From (2.29), the metric to be optimized is $\|\mathcal{Y} \mathbf{f}\|^2$ which was derived as a result of eliminating the propagation channel \mathbf{C} . The same objective may also be obtained by eliminating

the factor \mathbf{h} in (2.44), specifically by minimizing $\|\mathcal{F}^{\perp H} \mathbf{y}\|^2$. Here, \mathcal{F}^\perp is the orthogonal matrix to \mathcal{F} such that $\mathcal{F}^{\perp H} \mathcal{F} = \mathbf{0}$. \mathcal{F}^\perp corresponding to (2.43) is shown in (2.57).

$$(2.57) \quad \mathcal{F}^\perp = \begin{bmatrix} \mathbf{I} \otimes (\mathbf{F}_2 \mathbf{P}_2)^* & 0 & 0 \\ -(\mathbf{F}_1 \mathbf{P}_1)^* \otimes \mathbf{I} & 0 & 0 \\ 0 & \mathbf{I} \otimes (\mathbf{F}_3 \mathbf{P}_3)^* & 0 \\ 0 & -(\mathbf{F}_1 \mathbf{P}_1)^* \otimes \mathbf{I} & 0 \\ 0 & 0 & \mathbf{I} \otimes (\mathbf{F}_3 \mathbf{P}_3)^* \\ 0 & 0 & -(\mathbf{F}_2 \mathbf{P}_2)^* \otimes \mathbf{I} \end{bmatrix}$$

Thus, we can write,

$$(2.58) \quad \min_{\hat{\mathbf{f}}} \|\mathcal{F}^{\perp H}(\hat{\mathbf{f}})\mathbf{y}\|^2 = \min_{\hat{\mathbf{f}}} \|\mathcal{F}^{\perp H}(\hat{\mathbf{f}})\mathcal{F}\mathbf{h} + \mathcal{F}^{\perp H}(\hat{\mathbf{f}})\mathbf{n}\|^2,$$

where the additional term in braces highlights that in this case, the matrix $\mathcal{F}^{\perp H}$ is generated with $\hat{\mathbf{f}}$. When this is not explicitly indicated, the matrix is constructed out of the true \mathbf{f} . Next, to get (2.58) into a more convenient form, we make the following observation.

$$(2.59) \quad \begin{aligned} & \mathcal{F}^{\perp H}(\mathbf{f} - \hat{\mathbf{f}})\mathcal{F}(\mathbf{f} - \hat{\mathbf{f}}) = 0. \\ \Rightarrow & \left(\mathcal{F}^{\perp H}(\mathbf{f}) - \mathcal{F}^{\perp H}(\hat{\mathbf{f}}) \right) (\mathcal{F}(\mathbf{f}) - \mathcal{F}(\hat{\mathbf{f}})) = 0. \\ \Rightarrow & \mathcal{F}^{\perp H}(\mathbf{f})\mathcal{F}(\hat{\mathbf{f}}) = -\mathcal{F}^{\perp H}(\hat{\mathbf{f}})\mathcal{F}(\mathbf{f}). \end{aligned}$$

Further, under the assumption of small noise, $\mathcal{F}^{\perp H}(\hat{\mathbf{f}})\mathbf{n} \approx \mathcal{F}^{\perp H}(\mathbf{f})\mathbf{n}$. From (2.58), (2.59) and the small noise assumption, we can write the LS criterion as,

$$(2.60) \quad \min_{\hat{\mathbf{f}}} \|\mathcal{F}^{\perp H} \mathcal{F}(\hat{\mathbf{f}})\mathbf{h} - \mathcal{F}^{\perp H} \mathbf{n}\|^2 = \min_{\hat{\mathbf{f}}} \|\mathcal{F}^{\perp H} \mathcal{H}\hat{\mathbf{f}} - \mathcal{F}^{\perp H} \mathbf{n}\|^2.$$

At this point, note that $\mathcal{F}^{\perp H} \mathcal{H}$ is not full rank. This can be seen as follows.

$$(2.61) \quad \mathcal{F}^{\perp H} \mathcal{H}\mathbf{f} = \mathcal{F}^{\perp H} \mathcal{F}\mathbf{h} = \mathbf{0}.$$

Hence, to regularize the problem, we need to add constraints. Consider a linear constraint of the form,

$$(2.62) \quad \hat{\mathbf{f}}^H \mathbf{g} = c.$$

Let $\hat{\mathbf{f}} = \begin{bmatrix} \mathbf{g} & \mathcal{V} \end{bmatrix} \begin{bmatrix} \alpha_1 \\ \alpha_{2:M} \end{bmatrix}$, where \mathcal{V} is the orthonormal complement to the vector \mathbf{g} . The notation $\alpha_{2:M}$ indicates the elements 2 to M of the vector α . α_1 denotes the first element of the same vector. Now, using the constraint $\hat{\mathbf{f}}^H \mathbf{g} = \begin{bmatrix} \alpha_1^* & \alpha_{2:M}^* \end{bmatrix} \begin{bmatrix} \mathbf{g}^H \mathbf{g} \\ \mathcal{V}^H \mathbf{g} \end{bmatrix} = \alpha_1^* \mathbf{g}^H \mathbf{g} = c$. This implies that α_1 is real and is equal to a fixed value $\frac{c}{\mathbf{g}^H \mathbf{g}}$. As a result, (2.60) may be written in terms of the new parameters $\alpha_{2:M}$ as follows,

$$(2.63) \quad \min_{\hat{\mathbf{f}}} \|\mathcal{F}^{\perp H} \mathcal{H}\hat{\mathbf{f}} - \mathcal{F}^{\perp H} \mathbf{n}\|^2 = \min_{\alpha_{2:M}} \|\mathcal{F}^{\perp H} \mathcal{H}\mathcal{V} \alpha_{2:M} - \mathcal{F}^{\perp H} \mathbf{n} + \mathcal{F}^{\perp H} \mathcal{H}\mathbf{g} \frac{c}{\mathbf{g}^H \mathbf{g}}\|^2$$

The Mean Square Error (MSE) for this minimization is straightforward and may be obtained as

$$(2.64) \quad \text{MSE}_{\text{LS}} = \sigma^2 \mathcal{V} \left(\mathcal{V}^H \mathbf{A}^H \mathbf{A} \mathcal{V} \right)^{-1} \mathcal{V}^H \mathbf{A}^H \mathbf{B} \mathbf{A} \mathcal{V} \left(\mathcal{V}^H \mathbf{A}^H \mathbf{A} \mathcal{V} \right)^{-1} \mathcal{V}^H.$$

Here, $\mathbf{A} = \mathcal{F}^{\perp H} \mathcal{H}$ and $\mathbf{B} = \mathcal{F}^{\perp H} \mathcal{F}^{\perp}$. In comparison, the CRB from (2.46) is given by

$$(2.65) \quad \text{CRB} = \sigma^2 \mathcal{V}_f \left(\mathcal{V}_f^H \mathcal{H}^H \mathcal{F}^{\perp} (\mathcal{F}^{\perp H} \mathcal{F}^{\perp})^{-1} \mathcal{F}^{\perp H} \mathcal{H} \mathcal{V}_f \right)^{-1} \mathcal{V}_f^H = \sigma^2 \mathcal{V}_f \left(\mathcal{V}_f^H \mathbf{A}^H \mathbf{B}^{-1} \mathbf{A} \mathcal{V}_f \right)^{-1} \mathcal{V}_f^H,$$

where we used $\mathcal{P}_{\mathcal{F}}^{\perp} = \mathcal{P}_{\mathcal{F}^{\perp}} = \mathcal{F}^{\perp} (\mathcal{F}^{\perp H} \mathcal{F}^{\perp})^{-1} \mathcal{F}^{\perp H}$. Further, note that the matrix \mathcal{V}_f is a matrix that has to span the orthogonal complement of the derivative of the constraint. In our linear constraint (2.62), $\frac{\partial \mathcal{L}(f)}{\partial \mathbf{f}^*} = \mathbf{g}$. Hence, the matrix \mathcal{V} is the same as the desired matrix \mathcal{V}_f .

To understand the relation between (2.64) and (2.65), let us write down the expression for a weighted least squares with weight matrix \mathbf{W} .

$$(2.66) \quad \text{MSE}_{\text{WLS}} = \sigma^2 \mathcal{V} \mathbf{U} \mathcal{V}^H, \quad \mathbf{U} = \left(\mathcal{V}^H \mathbf{A}^H \mathbf{W} \mathbf{A} \mathcal{V} \right)^{-1} \mathcal{V}^H \mathbf{A}^H \mathbf{W} \mathbf{B} \mathbf{W} \mathbf{A} \mathcal{V} \left(\mathcal{V}^H \mathbf{A}^H \mathbf{W} \mathbf{A} \mathcal{V} \right)^{-1}.$$

Now, if we choose the weighting factor \mathbf{W} as \mathbf{B}^{-1} , we get back the same expression as that of the CRB. This implies, that to bring down the error variance to that of the CRB, a weighted least squares is called for. Thus, we establish that the key difference between the CRB and that of the MSE of the LS is in the lack of weighting factor $(\mathcal{F}^{\perp H} \mathcal{F}^{\perp})^{-1}$, which is intuitively appealing as this weighting factor is nothing but the inverse covariance of the colored noise in $\mathcal{F}^{\perp H} \mathbf{y}$.

The expression here covers the linear constraint as was given in 2.3. For the FCC, we need to choose $\mathbf{g} = \mathbf{e}_1$. In this case $\hat{\mathbf{f}}^H \mathbf{g} = c$ chooses the first element of $\hat{\mathbf{f}}$ to be known and the matrix \mathcal{V} is composed of the rest of the columns of the Identity matrix. Now, the NPC constraint may also be approximated by a linear constraint in the vicinity of the true \mathbf{f} . To see this, first, note that the phase part of the NPC constraint, as given in (2.27), is already a linear constraint where, in (2.62), we need to choose $\mathbf{g} = \mathbf{f}$. In the vicinity of the true \mathbf{f} , $\hat{\mathbf{f}}^H \hat{\mathbf{f}}$ may also be approximated by $\hat{\mathbf{f}}^H \mathbf{f}$, and hence the choice of $\mathbf{g} = \mathbf{f}$ serves as a linear approximation for the norm and phase part of the NPC constraint. With this choice, the matrix \mathcal{V} spans the orthogonal complement of the space of \mathbf{f} .

2.8 Simulation Results

In this section, we assess numerically the performance of various calibration algorithms, using $\text{MSE} = \mathbb{E}[\|\hat{\mathbf{f}} - \mathbf{f}\|^2]$ as the performance evaluation metric, and compare them against their CRBs as the benchmark. For all simulations, the Tx and Rx calibration parameters for the BS antennas are assumed to have random phases uniformly distributed over $[-\pi, \pi]$ and amplitudes uniformly distributed in the range $[1 - \delta, 1 + \delta]$ where $\delta = 0.1$. This assumption is widely used in literature such as in [34],[44],[43], which is also in line with the measurement results from experiments in [20]. We further assume that the first coefficient is fixed to 1 so that $f_1 = 1$ for the true \mathbf{f} . In this way, regardless of whether the FCC or the NPC (i.e. (2.26),(2.27) with $c = \|\mathbf{f}\|^2$) constraints are

used, direct comparison of $\hat{\mathbf{f}}$ to \mathbf{f} is possible for the MSE computation (in which the expectation is replaced by sample averaging). The channels between all the BS antennas are assumed to be independent and identically distributed (i.i.d.) Rayleigh fading unless specified otherwise.

2.8.1 Comparison of grouping based schemes

Now we evaluate the proposed group-based fast calibration method from Section 2.3.2. For a fair comparison across different schemes, the number of channel uses should be the same. Hence, we compare the fast calibration method of Section 2.3.2 against the Avalanche scheme proposed in [31]. Note that the Argos method and the method from Rogalin *et al.* are not fast algorithms as they need channel uses of the order of M , so they cannot be compared with the fast calibration methods. The number of antennas that transmit at each time instant (i.e. the group sizes of the 12 antenna groups) is shown in Table 2.2. FC-I corresponds to a fast calibration scheme where the antenna grouping is exactly the same as that of Avalanche. However, we also try a more equally partitioned grouping of antennas in FC-II. The pilots used for transmission have unit magnitudes with uniformly distributed random phases in $[-\pi, \pi]$.

Table 2.2: Number of antennas transmitting at each channel use for two Fast Calibration schemes.

Scheme	Antennas transmitting per channel use. $M = 64$											
FC-I	1	1	2	3	4	5	6	7	8	9	10	8
FC-II	5	5	5	5	5	5	5	5	6	6	6	6
Scheme	Antennas transmitting per channel use. $M = 67$											
FC-I	1	1	2	3	4	5	6	7	8	9	10	11
FC-II	5	5	5	5	5	6	6	6	6	6	6	6

The performance of these schemes is depicted in Fig. 2.4 for $M = 64$. From Section 2.3.2, it can be seen that the minimal number of channel uses required for calibration is $G = 12 = \lceil \sqrt{2M} \rceil$. The performance is averaged over 500 realizations of channel and calibration parameters. Note that the Avalanche algorithm inherently uses the FCC in its estimation process. For comparison to methods using NPC, the Avalanche estimate $\hat{\mathbf{f}}$ is then rescaled in order to satisfy the NPC constraint.

As the CRB depends on the constraint used for calibration estimation, the corresponding CRBs for these approaches are also shown. However, note that the CRB for the FC-I grouping applies to both the Avalanche method and the proposed fast calibration method (which performs least-squares (2.24) over all the available data jointly). For each type of constraint, there are thus 3 MSE curves (Avalanche, FC-I, and FC-II) and 2 CRB curves (for FC-I and FC-II). As the MSE curve is averaged over multiple channel realizations, the CRB plotted here is also an average over the CRB values corresponding to these channel realizations.

In Fig. 2.4, the performance of the proposed fast calibration with the FC-I grouping outperforms that of the Avalanche scheme. With $M = 64$ and $G = 12$ antenna groups, the overall system

of equations is overdetermined: from (2.31) with $L_i = 1$, $66 = \frac{1}{2}G(G - 1) > M - 1 = 63$. Note that the Avalanche scheme also transmits from multiple antennas at a time as a group. However, there are multiple reasons why the proposed fast calibration outperforms the Avalanche method.

- The proposed fast calibration exploits all data jointly for the parameter estimation unlike the Avalanche method, which employs a recursive method and is hence subject to error propagation.
- The performance improves when the group sizes are allocated more equitably as in grouping scheme FC-II. Intuitively, the overall estimation performance of the fast calibration would be limited by the (condition number of the) largest group size and hence it is reasonable to use a grouping scheme that tries to minimize the size of the largest antenna group. These observations hold irrespective of the constraints used.

The CRBs in Fig. 2.4 illustrate the ultimate calibration accuracy that calibration schemes can achieve, which, according to equation (2.46) depend on \mathbf{f} and hence also on the value of δ . The curves in Fig 2.4 are calculated with typical values defined at the beginning of this section. Avalanche with the FCC constraint exhibits a huge MSE and hence most portions of this curve fall outside the range of Fig. 2.4. Note also that the MSE in some cases falls below the CRB, see for instance the MSE NPC FC-I curve at low SNRs. This is because in this SNR region the MSE saturates due to bias and the CRB is no longer applicable.

To gain further insight into the working of Avalanche, it is illustrative to consider the case of $M = 67$ antennas, which is the maximum number of antennas that can be calibrated with $G = 12$ channel uses. As shown in section 2.3.2, the best strategy is to divide the antennas into $G = 12$ groups and letting each group transmit exactly once ($L_i = 1$). This then results in a linear system of 66 equations (2.29) plus one constraint in 67 unknowns. Indeed, (2.31) yields $66 = \frac{1}{2}G(G - 1) = M - 1 = 66$. Thus, the system of equations is exactly determined by using an appropriate constraint to resolve the scale factor ambiguity. Hence, the error attained by any LS solution would be zero and the different constraints used for estimation would only lead to different scale factors in the calibration parameter estimates. So, all the solutions would be equivalent. Also, FC-I grouping leads to a block triangular structure with square diagonal blocks for the matrix \mathcal{Y} defined in (2.30) after removing the first column. Hence, the back substitution based solution performed by Avalanche is indeed the overall LS solution with the first coefficient known constraint. Thus, in Fig. 2.5 where the performance of these schemes is compared for $M = 67$, we see that the curves for Avalanche and fast calibration with the FC-I grouping overlap completely. In general, this behavior would occur whenever the number of antennas corresponds to the maximum that can be calibrated with the number of channel uses (see Sec. 2.3.2), and the antenna grouping is similar to that for FC-I. At the range of SNRs considered, the MSE is saturated and is hence far below the CRB for this grouping. In fact, only a part of the CRB for the FC-I grouping can be seen as the rest of the curve falls outside the range of the figure. Indeed,

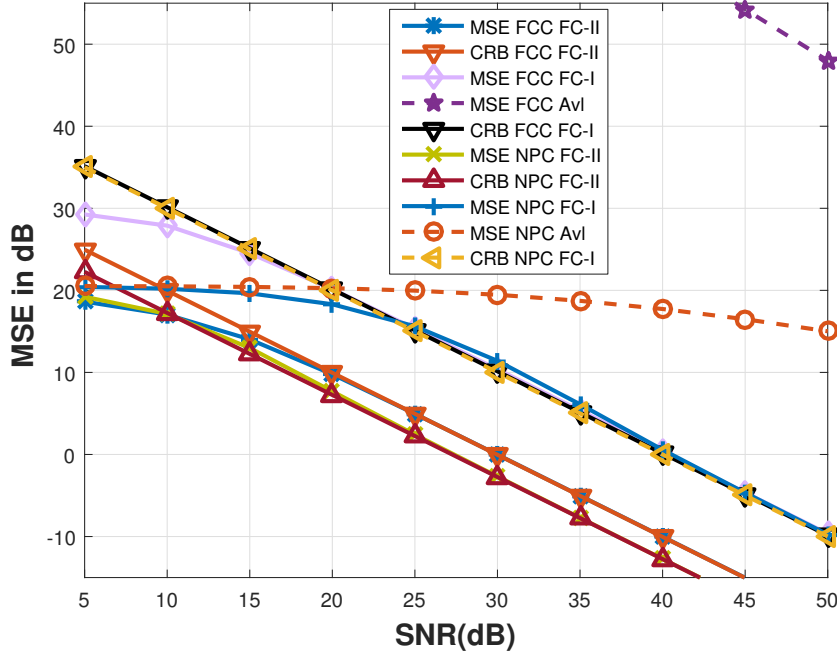


Figure 2.4: Comparison of fast calibration with Avalanche scheme ($M = 64$ and the number of channel uses is 12). The curves are averaged across 500 channel realizations. The performance with both the FCC and NPC constraints is shown.

though not shown in Fig. 2.5, the MSE curve with the FC-I grouping only starts to overlap with the corresponding CRB curve for SNR beyond 100dB! However, it is important to note that the performance improves dramatically with a more equitable grouping of the antennas as can be seen from the curves for the FC-II grouping in the same figure.

Next, we make a comparison between different grouping schemes on the basis of their CRB. Consider a system with $M = 64$ antennas. With single antenna grouping, the minimum number of channel uses required for calibration is M . Hence, we assume that there are M channel uses available for reciprocity calibration irrespective of the antenna grouping strategy used. At the same time, the minimum number of channel uses required for calibration is given by $G(G - 1) \geq (2M - 1)$, giving $G = 12$. In this case, the number of antennas in each group would be 5 or 6 if we distribute the antennas as equitably as possible across the groups. If we choose this scheme, then every antenna group can transmit pilots for multiple channel uses during the overall M channel uses required for the single antenna grouping. In Figure 2.6, we plot the CRB for different group sizes between the slowest single antenna grouping (Num groups = $M = 64$) and the fastest multiple antenna grouping. Whenever a faster grouping is used, antenna groups can transmit pilots during multiple channel uses which further scales down the CRB by that pilot use factor. The CRB is averaged over multiple realizations of the channel and an SNR of 30dB is considered. The NPC constraint is used for the calculation of the CRB. In this plot, two separate curves are displayed for $\delta = 0.25$ and $\delta = 0.5$. From this plot, we can infer

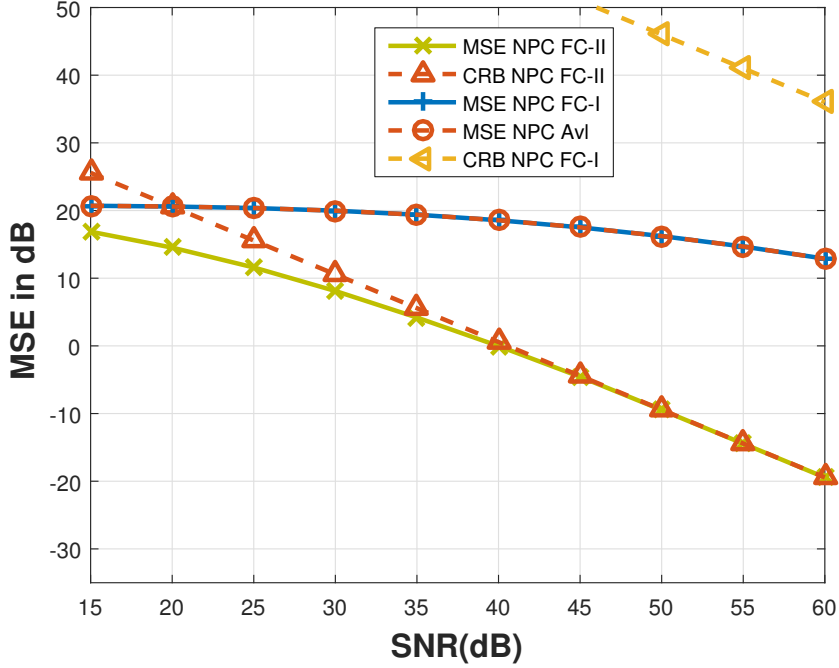


Figure 2.5: Comparison of fast calibration with Avalanche scheme for $M = 67$ and the number of channel uses=12. The curves are averaged across 500 channel realizations. The NPC constraint is used for the MSE computation.

that given a fixed number of available channel uses, it is more beneficial to use the smallest possible size for antenna groups. In the case where there are a sufficient number of channel uses available, this would imply a preference for the single antenna grouping over multiple antenna grouping. However, it is also noteworthy that a grouping with two antennas per group also has a performance comparable to that of single antenna grouping while requiring only half the time for calibration.

So far, we have focused on an i.i.d. intra-array channel model and we have seen in Fig. 2.4 and Fig. 2.5 that the size of the transmission groups is an important parameter that impacts the MSE of the calibration parameter estimates. We now consider a more realistic scenario where the intra-array channel is based on the geometry of the BS antenna array and make some observations on the choice of the antennas to form a group. We consider an array of $M = 64$ antennas arranged as in Fig. 2.7. The path loss $(4\pi \frac{d_{i \rightarrow j}}{\lambda})^2$ between any two antennas i and j is a function of their distance $d_{i \rightarrow j}$, and λ is the wavelength of the received signal. In the simulations, the distance between adjacent antennas, d , is chosen as $\frac{\lambda}{2}$. The phase of the channel between any two antennas is modeled to be a uniform random variable in $[-\pi, \pi]$. Such a model was also observed experimentally in [43]. The SNR is defined as the signal to noise ratio observed at the receive antenna nearest to the transmitter.

Continuing with the same internal channel model, consider a scenario in which antennas transmit in $G = 16$ groups of 4 each. Note that this is not the fastest grouping possible, but the

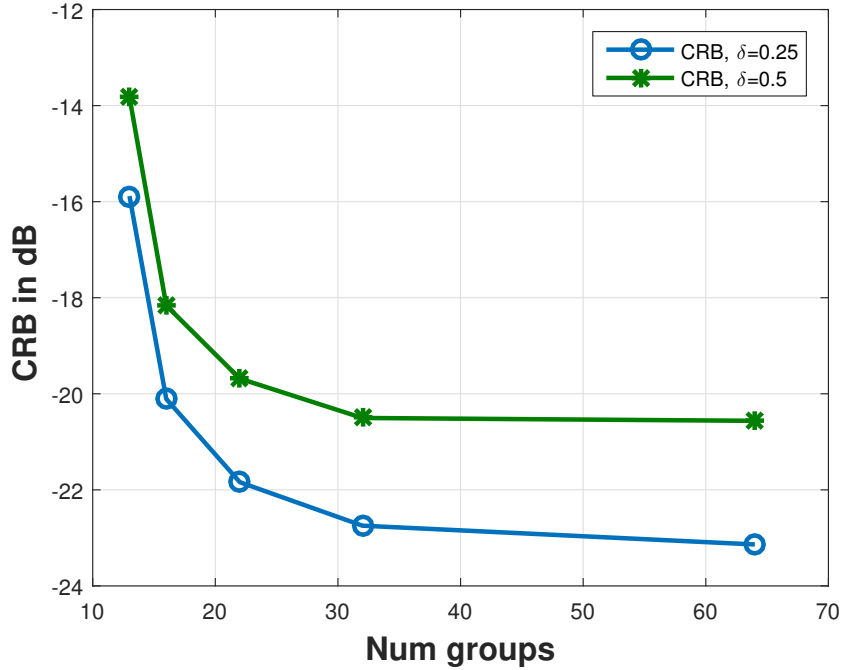


Figure 2.6: Comparison of CRB with different antenna group sizes for $M = 64$ antenna scenario.

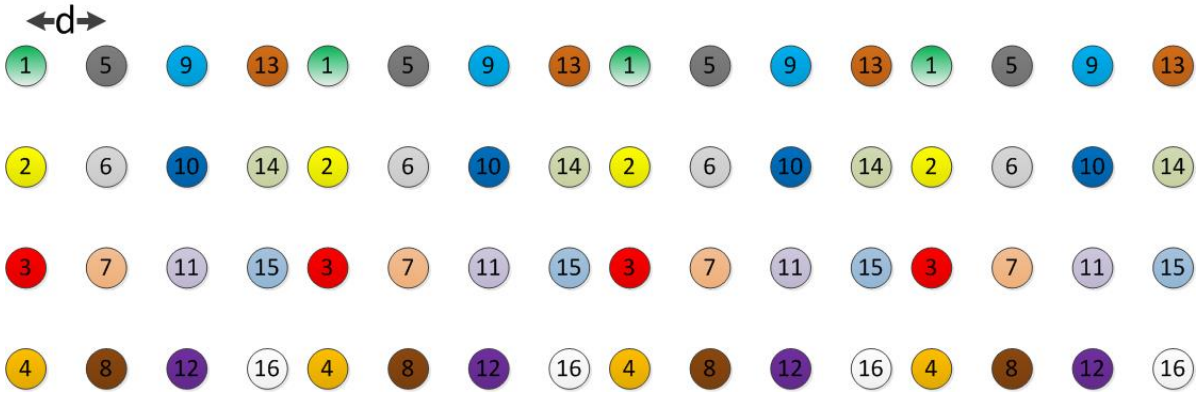


Figure 2.7: 64 antennas arranged as a 4×16 grid.

example is used for the sake of illustration. We consider two different choices to form the antenna groups: 1) interleaved grouping corresponding to selecting antennas with the same numbers into one group as in Fig. 2.7, 2) non-interleaved grouping corresponding to selecting antennas in each column as a group. Fig. 2.8 shows that interleaving of the antennas results in performance gains of about 10dB. Intuitively, the interleaving of the antennas ensures that the channel from a group to the rest of the antennas is as well conditioned as possible. This example clearly shows that in addition to the size of the antenna groups, the choice of the antennas that go into each group also has a significant impact on the estimation quality of the calibration parameters.

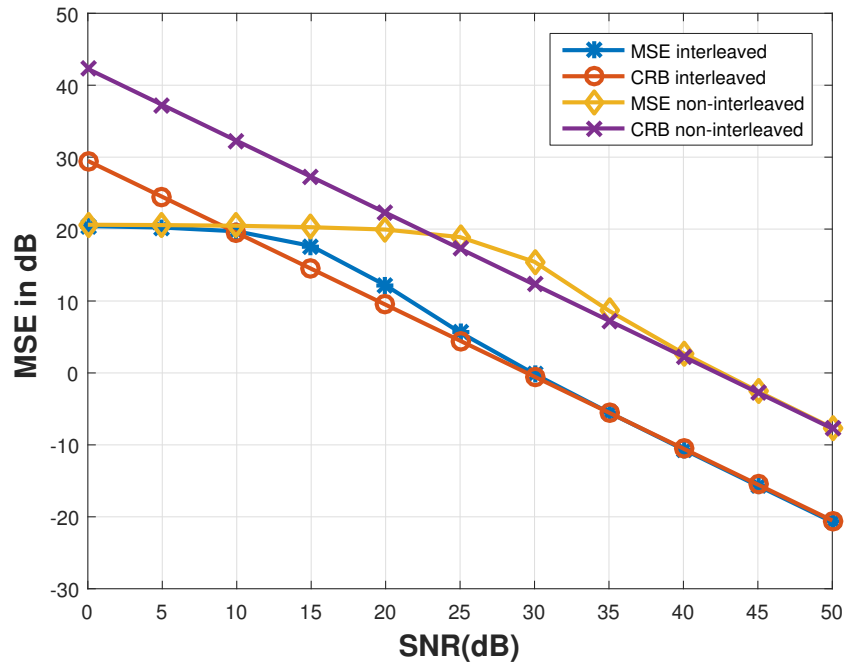


Figure 2.8: Interleaved and non-interleaved MSE and CRB with NPC for an antenna transmit group size of 4 ($M = 64$ and the number of channel uses is $G = 16$).

2.8.2 Comparison of single antenna transmission schemes

In Fig. 2.9, we consider slower transmit schemes that transmit from one antenna at a time ($G = M$) and compare their MSE performance with the CRB. The MSE with FCC for Argos, the method of Rogalin *et al.* [34] and the AML method in Algorithm 1 is plotted. As expected, the method of Rogalin *et al.* improves over Argos by using all the bi-directional received data. AML outperforms the performance of the method by Rogalin *et al.* at low SNR. These curves are compared with the CRB derived in 2.4 for the FCC case and it can be seen that the AML curve overlaps with the CRB at higher SNRs. Also plotted is the CRB as given in [43] assuming the internal propagation channel is fully known (the mean is known and the variance is negligible) and the underestimation of the MSE can be observed as expected. As was mentioned in section 2.6, the greater the variation in \mathbf{f} , greater would be the deviation of the LS approaches from the ML estimator and greater would be the advantage in using the AML method. To bring out the difference between the two CRB derivations, the amplitude variation parameter δ is chosen to be 0.5 to increase the range of values of Tx and Rx calibration parameters.

Figure 2.10 compares the MSE that was derived for the LS with the actual performance obtained in simulations using FCC. The results have been averaged across multiple channel and noise realizations. A large variation in calibration values ($\delta = 0.95$) is chosen for this simulation so as to enhance the gap between the LS performance and the CRB. The simulated MSE is seen to closely match the theoretical MSE. The plot also shows the CRB for this case which forms a

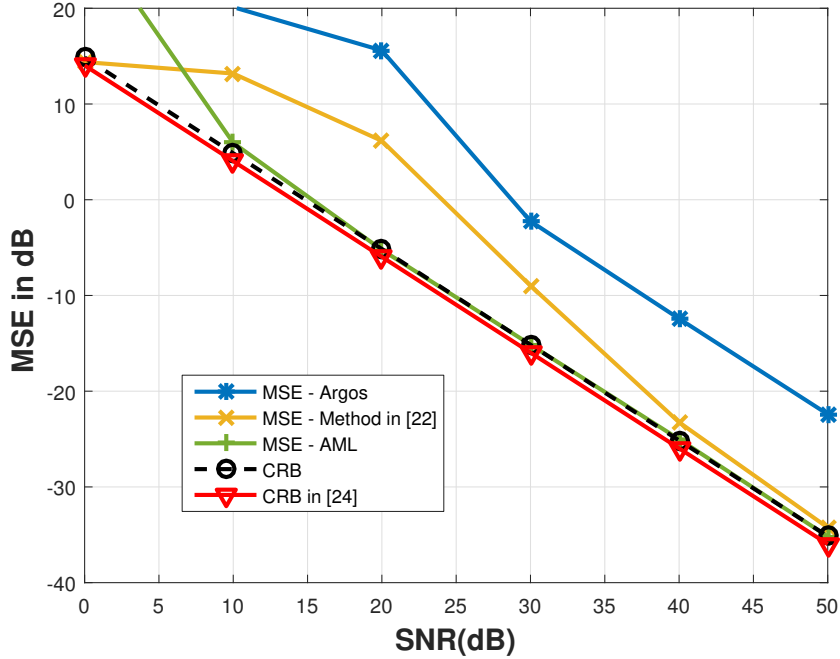


Figure 2.9: Comparison of single antenna transmit schemes with the CRB ($G = M = 16$). The curves are generated over one realization of an i.i.d. Rayleigh channel and a known first coefficient constraint is used.

lower bound, as expected.

Next, we compare the convergence of the optimal algorithms that were proposed in section 2.5 when the calibration parameters are generated with $\delta = 0.25$ in Figure 2.11. The curves in Figure 2.11 are generated for a single channel and calibration parameter realization and averaged over 200 noise realizations. We clearly see that the VB methods (initialized by LS) are far superior to the AML in terms of both MSE achievable and speed of convergence.

2.9 Summary of Contributions

- Showed that the group calibration framework proposed in [?] can result in Fast calibration (Section 2.3.2).
- Came up with a simple and elegant expression for the CRB for calibration parameter estimation (Section 2.4) that includes both coherent and non-coherent estimation methods.
- Came up with optimal algorithms for calibration parameter estimation (Section 2.5).
- We analyzed the performance of least squares methods and showed analytically that their performance differs from that of the CRB simply because they don't take into account the fact that the noise is colored.

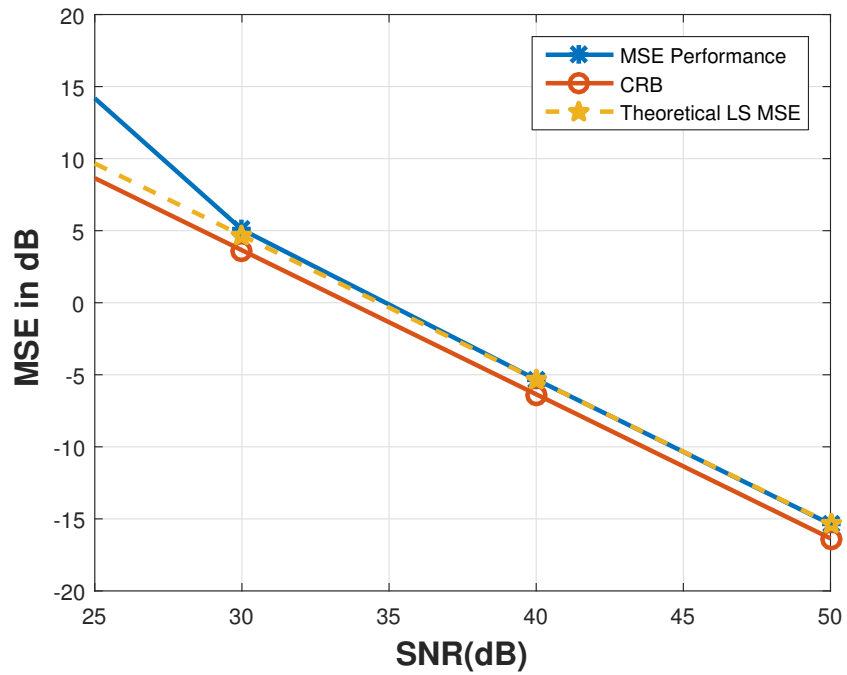


Figure 2.10: Comparison of simulation MSE for an $M = 32$ antenna scenario with the theoretical expression for MSE for the first coefficient known constraint (FCC).

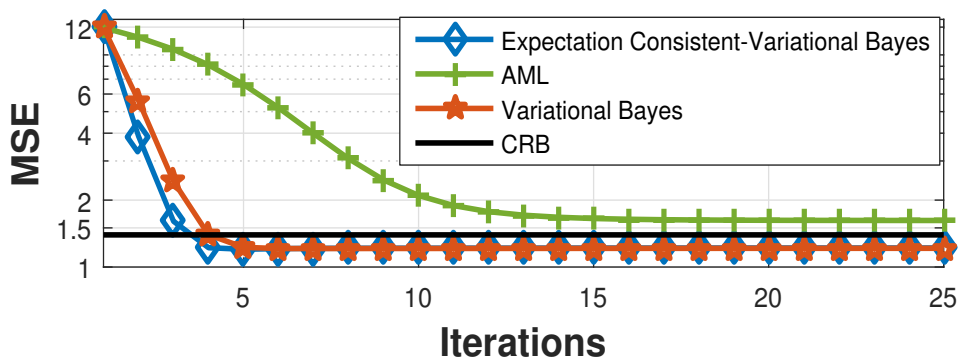


Figure 2.11: Convergence of the various iterative schemes for $M = 16$ and $G = M$.

- Some of the above contributions were published in [?], [?] and the rest will be in [?].
- This work has also resulted in a patent submission [?].

PRECODER DESIGN UNDER DOPPLER - FULL CSIT



3.1 Introduction

We consider a rapidly time-varying point to point MIMO link as encountered in HST (high-speed train) communicating with a BS. The BS is assumed to be within a distance of one kilometer from the track. The channel model [21] in such a scenario consists of the LoS path and a few reflected paths primarily due to reflections from the gantries that support the railway electrification system. The high Doppler encountered in this environment violates the orthogonality requirement for

OFDM, resulting in ICI. Several prior publications have focused on receiver techniques to mitigate ICI ([12],[48]) and it is known that multiple receive antennas in a SIMO scenario are very effective in canceling out the ICI. However, there has been no existing work on optimal precoder design in the case of MIMO. Hence, We study this problem under full CSIT.

3.1.1 Key Assumption

This work assumes full CSIT. Of course, this is hard to obtain in general, but the fact that our work is for an HST that runs on well-defined tracks makes the scenario a bit more plausible. For instance, a database could be maintained for the channels observed at different positions on the track. An alternative is to have additional leading antennas on the train that can perform DL channel estimation via channel reciprocity in case of a TDD system. As the train moves, the set of antennas dedicated for transmission would arrive at the same location and could use these channel estimates. We would also like to remark that this requirement for full CSIT is relaxed in the next chapter.

3.2 System Model

Consider a multiple input multiple output (MIMO) system with N_t transmit antennas and N_r receive antennas. An OFDM framework is chosen with N subcarriers and sampling rate f_s . Out of the total N subcarriers, let N_u be the number of utilized subcarriers. For instance, this would account for the guard subcarriers and DC subcarrier in an OFDM system. We consider a time-varying Rician fading FIR channel of length L . Thus for every combination of Tx(transmit) and Rx(receive) antenna, the time domain channel at sample n of an OFDM symbol may be represented as

$$(3.1) \quad \mathbf{h}(n) = \mathbf{h}_0 + \mathbf{h}'(n)$$

where \mathbf{h}_0 is of dimension $L \times 1$ and represents the average channel across the OFDM symbol. \mathbf{h}' is also of dimension $L \times 1$ and captures the time variation, has average value zero, and is orthogonal to \mathbf{h}_0 . It is easy to see that with this formulation, the ICI contribution comes entirely from $\mathbf{h}'(n)$.

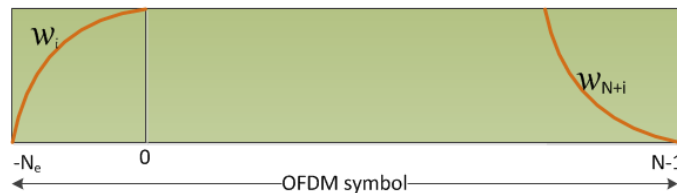


Figure 3.1: Illustration of ExCP windowing in an OFDM symbol

The length of the CP is considered to be greater than the channel delay spread by N_e samples. The total length of the OFDM symbol including the ExCP length is taken as $N_s = N + N_e$. It is

also assumed that the receiver would take advantage of this ExCP through windowing. As shown in Figure 3.1, let w_i be the window weights. In order to satisfy the Nyquist criterion

$$(3.2) \quad w_i + w_{N+i} = 1, \quad i \in \{-N_e \dots -1\}$$

Consider a single input single output (SISO) system and a linear time-invariant (LTI) channel of length L . The received symbols at the subcarrier level obtained after the fast Fourier transform (FFT) may be expressed as

$$(3.3) \quad \mathbf{y} = \mathbf{F}_N \mathbf{T}_{ex}^T \mathbf{D}_w \mathbf{T}_{-ds} \check{\mathbf{H}}_0 \mathbf{T}_{cp} \mathbf{F}_N^{-1} \mathbf{s} + \mathbf{F}_N \mathbf{T}_{ex}^T \mathbf{D}_w \check{\mathbf{v}}$$

This equation may be interpreted as follows. The inverse FFT (IFFT) matrix \mathbf{F}_N^{-1} acts on the data \mathbf{s} to produce the N OFDM time domain samples. The time domain samples are extended into the overall cyclic prefix that includes the length of the ExCP as well as the actual channel delay spread. The overall operation of cyclic prefix addition may be represented as \mathbf{T}_{cp} .

$$(3.4) \quad \mathbf{T}_{cp} = \begin{bmatrix} \mathbf{0}_{(L+N_e) \times (N-N_e-L)} & \mathbf{I}_{N_e+L} \\ & \mathbf{I}_N \end{bmatrix}, \quad \mathbf{T}_{ex} = \begin{bmatrix} \mathbf{0}_{N_e \times (N-N_e)} & \mathbf{I}_{N_e} \\ & \mathbf{I}_N \end{bmatrix},$$

The matrix $\check{\mathbf{H}}_0$ represents time domain convolution. The matrix \mathbf{T}_{-ds} represents the removal of the portion of the CP corresponding to the channel delay spread.

$$(3.5) \quad \mathbf{T}_{-ds} = \begin{bmatrix} \mathbf{0}_{(N+N_e) \times L} & \mathbf{I}_{N+N_e} \end{bmatrix}$$

\mathbf{D}_w represents the windowing over the ExCP region and \mathbf{T}_{ex}^T represents the folding operation after windowing at the Rx.

$$\mathbf{D}_w = \text{diag}(w_{-N_e} \dots w_{-1} \ 1 \dots 1 \ w_1 \dots w_{N_e}) = \text{diag}(\mathbf{w})$$

With this, equation (3.3) may be equivalently expressed as

$$(3.6) \quad \mathbf{y} = \mathbf{F}_N \mathbf{T}_{ex}^T \mathbf{D}_w \mathbf{T}_{ex} \check{\mathbf{H}}_0 \mathbf{F}_N^{-1} \mathbf{s} + \mathbf{F}_N \mathbf{T}_{ex}^T \mathbf{D}_w \check{\mathbf{v}},$$

where $\check{\mathbf{H}}_0$ is a circulant matrix such that $\mathbf{T}_{-ds} \check{\mathbf{H}}_0 \mathbf{T}_{cp} = \mathbf{T}_{ex} \check{\mathbf{H}}_0$. Now, if $\mathbf{T}_{ex}^T \mathbf{D}_w \mathbf{T}_{ex} = \mathbf{I}$, it can be seen easily that $\mathbf{F}_N \mathbf{T}_{ex}^T \mathbf{D}_w \mathbf{T}_{ex} \check{\mathbf{H}}_0 \mathbf{F}_N^{-1}$ would form a diagonal matrix as the FFT matrix forms the eigen vectors of a circulant matrix. Now, the requirement that $\mathbf{T}_{ex}^T \mathbf{D}_w \mathbf{T}_{ex} = \mathbf{I}$ is the same as the Nyquist criterion in equation (3.2) and hence clearly shows the need for this criterion to avoid ICI due to the receive windowing operation. Note also that equation (3.6) does not explicitly show the CP that accounts for the channel delay spread. In what follows, we will follow this approach to simplify our equations.

To continue the analysis, we can approximate $\mathbf{h}'(n)$ by a polynomial function. For an LTE-like OFDM system, we choose a linear model due to the significant subcarrier spacing compared to the Doppler frequency being considered. To verify the validity of this assumption we consider a

typical LTE scenario with center frequency 2.4GHz and channel spacing 15KHz. For various SNR values, the mean channel power, ICI as predicted by the linear model and Residual ICI beyond what is predicted by the linear model are shown in 3.2. It is clear that up to a Doppler of 1000Hz, which corresponds to a velocity of 450Kmph at 2.4GHz, the error due to the linear assumption is below -40dB.

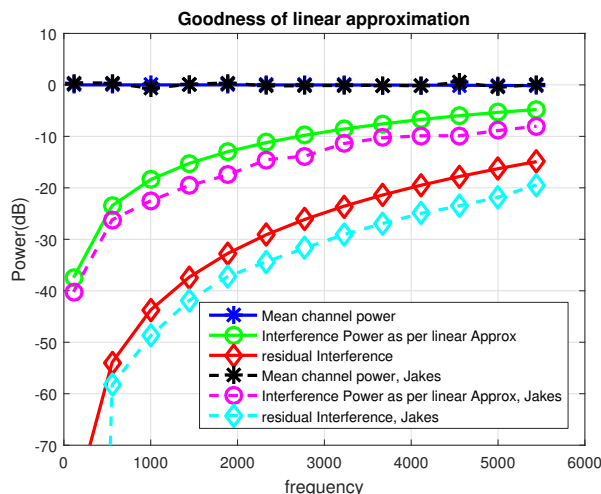


Figure 3.2: Verification of the linear model for channel variation.

At 450Kmph, 2.4GHz center frequency, Doppler frequency = 1KHz. From Figure 3.2, approximation error due to the linear modeling of ICI negligible up to 450Kmph assuming operating SNR < 35dB I.e, at this operating SNR, the error due to the approximation in channel variation is significantly lower than that of the AWGN noise floor. Indeed, if the operating SNR is lower, Figure 3.2 shows that channel variation may be safely treated as linear across the OFDM symbol for even higher levels of Doppler. We can also infer that at low operating SNR (< 10dB), the ICI due to speeds up to 450Kmph is negligible.

Thus, for the duration of an OFDM symbol including the ExCP, equation (3.1) may be rewritten in terms of orthogonal basis functions for every Tx-Rx antenna pair as,

$$(3.7) \quad \begin{bmatrix} \mathbf{h}^T(-N_e) \\ \vdots \\ \mathbf{h}^T(N-1) \end{bmatrix} = \begin{bmatrix} 1 & (-N_e - \frac{N_s-1}{2}) \\ \vdots & \vdots \\ 1 & (N-1 - \frac{N_s-1}{2}) \end{bmatrix} \begin{bmatrix} \mathbf{h}_0^T \\ \mathbf{h}_1^T \end{bmatrix}$$

where \mathbf{h}_1 is a constant across the OFDM symbol and captures the time variation per sample. Note here that \mathbf{h} is a column vector of length L representing the number of channel taps. Equation (3.7) implies that the transmit signal corresponding to every OFDM symbol passes through two independent time-invariant channels \mathbf{h}_0 and \mathbf{h}_1 . However, the output of the channel \mathbf{h}_1 gets modified by the linear time variation that results in ICI.

Next, we look a general point to point MIMO scenario with multiple Tx and Rx antennas. For the ease of handling the problem mathematically, we stack the symbols received at all the Rx

antennas across all the subcarriers of the OFDM symbol. This would result in a column vector of length $N_r N$ (N_r received elements for each subcarrier). The receiver output across all the receive antennas and subcarriers after the windowing and N -point FFT may be expressed as a column vector of length $N_r N$ (N_r received elements for each subcarrier). This may be expressed as,

$$(3.8) \quad \mathbf{y} = \mathbf{F}_{N,N_r} \mathbf{T}_{ex,N_r}^T \mathbf{D}_{w,N_r} \{ \mathbf{T}_{ex,N_r} \check{\mathbf{H}}_0 + \mathbf{D}_{b,N_r} \mathbf{T}_{ex,N_r} \mathbf{T}_{ex,N_r} \check{\mathbf{H}}_1 \} \mathbf{F}_{N,N_t}^{-1} \mathbf{s} + \mathbf{F}_{N,N_r} \mathbf{T}_{ex,N_r}^T \mathbf{D}_{w,N_r} \check{\mathbf{v}}.$$

$\check{\mathbf{H}}_0$ and $\check{\mathbf{H}}_1$ are time domain block circulant channel matrices of dimension $N_r N \times N_t N$. Each block in $\check{\mathbf{H}}_0$ or $\check{\mathbf{H}}_1$ is of dimension $N_r \times N_t$ and there are $N \times N$ such blocks in these matrices. $\check{\mathbf{v}}$ is the AWGN noise observed at the receiver and is normalized to have unit variance. \mathbf{s} is the concatenated transmit data vector across all the transmit antennas and subcarriers and is of dimension NN_t . $\mathbf{F}_{N,N_t} = \mathbf{F}_N \otimes \mathbf{I}_{N_t}$, where \mathbf{F}_N is the DFT (discrete Fourier transform) matrix.

$$\mathbf{D}_b = \text{diag} \left(-\left(N_e - \frac{N_s - 1}{2}\right) \dots \left(N - 1 - \frac{N_s - 1}{2}\right) \right)$$

Further, $\mathbf{D}_{w,N_r} = \mathbf{D}_w \otimes \mathbf{I}_{N_r}$, $\mathbf{D}_{b,N_r} = \mathbf{D}_b \otimes \mathbf{I}_{N_r}$ and $\mathbf{T}_{ex,N_r} = \mathbf{T}_{ex} \otimes \mathbf{I}_{N_r}$. Hence, assuming that the window parameters satisfy the Nyquist condition, equation (3.8) may be rewritten as

$$(3.9) \quad \begin{aligned} \mathbf{y} &= \check{\mathbf{H}}_0 \mathbf{s} + \mathbf{F}_{N,N_r} \mathbf{T}_{ex,N_r}^T \mathbf{D}_{w,N_r} \mathbf{D}_{b,N_r} \mathbf{T}_{ex,N_r} \check{\mathbf{H}}_1 \mathbf{F}_{N,N_t}^{-1} \mathbf{s} + \mathbf{F}_{N,N_r} \mathbf{T}_{ex,N_r}^T \mathbf{D}_{w,N_r} \check{\mathbf{v}} \\ &= \check{\mathbf{H}}_0 \mathbf{s} + \check{\Xi} \mathbf{H}_1 \mathbf{s} + \mathbf{v} \end{aligned}$$

where $\check{\mathbf{H}}_0 = \mathbf{F}_{N,N_r} \check{\mathbf{H}}_0 \mathbf{F}_{N,N_t}^{-1}$ is a block diagonal matrix corresponding to the time-invariant part. $\mathbf{H}_1 = \mathbf{F}_{N,N_r} \check{\mathbf{H}}_1 \mathbf{F}_{N,N_t}^{-1}$ is a block diagonal matrix corresponding to the time-varying part of the channel. $\check{\Xi} = \mathbf{F}_{N,N_r} \mathbf{T}_{ex,N_r}^T \mathbf{D}_{w,N_r} \mathbf{D}_{b,N_r} \mathbf{T}_{ex,N_r} \mathbf{F}_{N,N_t}^{-1}$, where Ξ is a block circulant matrix. It can be easily observed using the properties of the Kronecker product that $\check{\Xi} = \Xi \otimes \mathbf{I}_{N_r}$, where $\Xi = \mathbf{F}_N \mathbf{T}_{ex}^T \mathbf{D}_w \mathbf{D}_b \mathbf{T}_{ex} \mathbf{F}_N^{-1}$ is a circulant matrix of dimension $N \times N$. As Ξ is circular, any element k, l of the matrix may be expressed as $\xi((l - k)_N)$ where the notation $(\cdot)_N$ refers to modulo operation with respect to N . ξ would be the first row vector of Ξ and hence of length N . $\mathbf{v} = \mathbf{F}_{N,N_r} \mathbf{T}_{ex,N_r}^T \mathbf{D}_{w,N_r} \check{\mathbf{v}}$ is the frequency domain noise samples seen across the subcarriers and receive antennas.

Thus, at any subcarrier k , the received data may be written as

$$(3.10) \quad \mathbf{y}_k = (\check{\mathbf{H}}_{0k} + \mathbf{H}_{1k} \xi(0)) \mathbf{d}_k + \sum_{l=0, l \neq k}^{N-1} \mathbf{H}_{1l} \mathbf{d}_l \xi((l - k)_N) + \mathbf{v}_k = \underbrace{\mathbf{H}_{0k} \mathbf{d}_k}_{\text{Signal term}} + \underbrace{\sum_{l=0, l \neq k}^{N-1} \mathbf{H}_{1l} \mathbf{d}_l \xi((l - k)_N) + \mathbf{v}_k}_{\text{ICI and noise terms}}$$

\mathbf{H}_{0k} (dimension $N_r \times N_t$) is the mean frequency domain channel observed at subcarrier k . The second term in equation (3.10) represents the ICI caused by time variation due to Doppler. $\mathbf{d}_k = [\mathbf{s}(kN_t + 1) \dots \mathbf{s}(kN_t + N_t - 1)]^T$ is the $N_t \times 1$ vector of transmitted data symbols on the carrier k . $\xi((l - k)_N)$ refers to the (k, l) element of the matrix Ξ . \mathbf{v}_k is the $N_r \times 1$ vector of AWGN (additive white Gaussian noise) noise observed at carrier index k , with the following variance.

$$(3.11) \quad \mathbf{R}_{\mathbf{v}_k} = (e_k^T \mathbf{F}_N \mathbf{T}_{ex}^T \mathbf{D}_w \mathbf{D}_w^H \mathbf{T}_{ex} \mathbf{F}_N^H e_k) \otimes \mathbf{I}_{N_r} = (e_k^T \mathbf{F}_N \mathbf{T}_{ex}^T \mathbf{D}_w \mathbf{D}_w^H \mathbf{T}_{ex} \mathbf{F}_N^H e_k) \mathbf{I}_{N_r}$$

where e_k is a column vector with 1 at the k^{th} element. Let P be the maximum sum power requirement across all the subcarriers and let P_i be the individual power at any subcarrier i such that $\sum_{i=0}^{N-1} P_i = P$. Let the transmit covariance matrix of subcarrier k be $\mathbf{Q}_k = \mathbf{E}(\mathbf{d}_k \mathbf{d}_k^H)$ where $\mathbf{E}(\cdot)$ is the expectation operator. Thus, the capacity of this MIMO system across all the subcarriers in the presence of both ICI and AWGN noise would be given as follows.

$$(3.12) \quad \mathbf{C} = \sum_{k=0}^{N-1} \log |\mathbf{I} + \mathbf{H}_{0k} \mathbf{Q}_k \mathbf{H}_{0k}^H \mathbf{R}_k^{-1}|$$

where $\mathbf{R}_k = \mathbf{R}_{v_k} + \sum_{l=0, l \neq k}^{N-1} |\xi((l-k)_N)|^2 \mathbf{H}_{1l} \mathbf{Q}_l \mathbf{H}_{1l}^H$. Note that this formulation can include guard subcarriers and DC subcarrier by simply forcing their respective transmit covariances to zero. We are interested in determining the optimal \mathbf{Q}_k and the window weights w_i such that the capacity of the link is maximized under a power constraint

$$(3.13) \quad f_0 : \max_{\mathbf{Q}_k, \mathbf{w}} \mathbf{C} = \sum_{k=0}^{N-1} \log |\mathbf{I} + \mathbf{H}_{0k} \mathbf{Q}_k \mathbf{H}_{0k}^H \mathbf{R}_k^{-1}| \quad \text{subject to} \quad \sum_{k=0}^{N-1} \text{tr}\{\mathbf{Q}_k\} \leq P.$$

3.3 Precoder Design

We first note that the mathematical problem of a point to point MIMO precoder design under Doppler (3.13) is similar to that of a MIMO interfering broadcast channel (IBC). The only difference is that the interference from other base stations is replaced by ICI. Hence, similar approaches may be considered in this problem as well. The objective function f_0 in (3.13) is non-convex in the covariance matrix \mathbf{Q}_i and hence we follow an iterative majorization [38] based approach which is a re-interpretation of the technique used in [23]. In addition, to solve the joint problem of optimizing the window design we employ the alternating (cyclic) minimization approach to alternately optimize the precoder design and window design. At the beginning of the iteration for the subcarrier i , let P_i be the power constraint, $\bar{\mathbf{Q}}_i$ be the current values of the precoder and w_i be the window values. The steps involved in optimization are

- Update the value of \mathbf{Q}_i for every used subcarrier i using the majorization technique ([38]). This is given in subsection 3.3.1.
- Update of power allocation across all the subcarriers. This is given in subsection 3.3.2.
- Update of window parameters. This is given in section 3.3.3.

3.3.1 Covariance matrix update

Our iterative optimization algorithm operates one subcarrier at a time. With the focus on subcarrier i , on the same lines as [23], the objective function f_0 may be rewritten as

$$(3.14) \quad \max_{\mathbf{Q}_i} \sum_{k=0}^{N-1} \log |\mathbf{I} + \mathbf{H}_{0k} \mathbf{Q}_k \mathbf{H}_{0k}^H \mathbf{R}_k^{-1}| = \max_{\mathbf{Q}_i} \{\log |\mathbf{I} + \mathbf{H}_{0i} \mathbf{Q}_i \mathbf{H}_{0i}^H \mathbf{R}_i^{-1}| + f_i(\mathbf{Q}_i, \mathbf{Q}_{-i})\}$$

where $f_i(\mathbf{Q}_i, \mathbf{Q}_{-i}) = \sum_{l \neq i} \log |\mathbf{I} + \mathbf{H}_{0l} \mathbf{Q}_l \mathbf{H}_{0l}^H \mathbf{R}_l^{-1}|$. \mathbf{Q}_{-i} refers to the transmit covariances of all the subcarriers except for the i^{th} . It is shown in [23] (*Lemma 1*) that $f_i(\mathbf{Q}_i, \mathbf{Q}_{-i})$ is convex in \mathbf{Q}_i . Thus, equation (3.14) is the sum of a concave and convex function and hence the overall capacity is a non-convex function.

We replace the non-convex function above with its minorization. To obtain the minorizer, we replace a convex function $f_i(\mathbf{Q}_i, \mathbf{Q}_{-i})$ by its tangent at $\bar{\mathbf{Q}}_i, \bar{\mathbf{Q}}_{-i}$. As the tangent to a convex function always lies below the function, the new function f_1 is clearly a minorizer.

$$(3.15) \quad \begin{aligned} f_1 : \log |\mathbf{I} + \mathbf{H}_{0i} \mathbf{Q}_i \mathbf{H}_{0i}^H \mathbf{R}_i^{-1}| - \text{tr} \{ \mathbf{B}_i (\mathbf{Q}_i - \bar{\mathbf{Q}}_i) \} + f_i(\bar{\mathbf{Q}}_i, \bar{\mathbf{Q}}_{-i}) \\ \text{subject to } \text{tr} \{ \mathbf{Q}_i \} \leq \bar{P}_i \end{aligned}$$

where \mathbf{B}_i is the negative Hermitian of the derivative of $f_i(\mathbf{Q}_i, \mathbf{Q}_{-i})$ with respect to \mathbf{Q}_i evaluated at $\bar{\mathbf{Q}}_i, \bar{\mathbf{Q}}_{-i}$. \bar{P}_i indicates the current value of P_i at any given stage of the algorithm. \mathbf{B}_i is given in equation (3.16) below (see also [17]).

$$(3.16) \quad \begin{aligned} f_i(\mathbf{Q}_i, \mathbf{Q}_{-i}) &= \sum_{l \neq i} \log |\mathbf{I} + \mathbf{H}_{0l} \mathbf{Q}_l \mathbf{H}_{0l}^H \mathbf{R}_l^{-1}| = \sum_{l \neq i} \{ \log |\mathbf{R}_l + \mathbf{H}_{0l} \mathbf{Q}_l \mathbf{H}_{0l}^H| - \log |\mathbf{R}_l| \} \\ \partial \mathbf{R}_l &= \mathbf{H}_{1i} \partial \mathbf{Q}_i \mathbf{H}_{1i}^H |\xi((i-l)_N)|^2 \\ \partial f_i(\mathbf{Q}_i, \mathbf{Q}_{-i}) &= \sum_{l \neq i} \text{tr} \{ ((\mathbf{R}_l + \mathbf{H}_{0l} \mathbf{Q}_l \mathbf{H}_{0l}^H)^{-1} - \mathbf{R}_l^{-1}) \partial \mathbf{R}_l \} \\ &= \text{tr} \{ ((\mathbf{R}_l + \mathbf{H}_{0l} \mathbf{Q}_l \mathbf{H}_{0l}^H)^{-1} - \mathbf{R}_l^{-1}) \mathbf{H}_{1i} \partial \mathbf{Q}_i \mathbf{H}_{1i}^H |\xi((i-l)_N)|^2 \} \\ &= \text{tr} \{ |\xi((i-l)_N)|^2 \mathbf{H}_{1i}^H ((\mathbf{R}_l + \mathbf{H}_{0l} \mathbf{Q}_l \mathbf{H}_{0l}^H)^{-1} - \mathbf{R}_l^{-1}) \mathbf{H}_{1i} \partial \mathbf{Q}_i \} \\ \mathbf{B}_i &= - \left[\frac{\partial f_i(\mathbf{Q}_i, \mathbf{Q}_{-i})}{\partial \mathbf{Q}_i} \right]^H \\ &= \sum_{l \neq i} |\xi((i-l)_N)|^2 \mathbf{H}_{1i}^H \{ \mathbf{R}_l^{-1} - (\mathbf{R}_l + \mathbf{H}_{0l} \mathbf{Q}_l \mathbf{H}_{0l}^H)^{-1} \} \mathbf{H}_{1i} \end{aligned}$$

The Lagrangian for f_1 may now be written as

$$(3.17) \quad \mathbf{L}(\mathbf{Q}_i, \mu_i) = \log |\mathbf{I} + \mathbf{H}_{0i} \mathbf{Q}_i \mathbf{H}_{0i}^H \mathbf{R}_i^{-1}| - \text{tr} \{ \mathbf{B}_i (\mathbf{Q}_i - \bar{\mathbf{Q}}_i) \} + f_i(\bar{\mathbf{Q}}_i, \bar{\mathbf{Q}}_{-i}) - \mu_i (\text{tr} \{ \mathbf{Q}_i \} - \bar{P}_i)$$

where $\mu_i \geq 0$. The term $\log |\mathbf{I} + \mathbf{H}_{0i} \mathbf{Q}_i \mathbf{H}_{0i}^H \mathbf{R}_i^{-1}|$ is concave in \mathbf{Q}_i . As \mathbf{B}_i is a constant, $\text{tr} \{ \mathbf{B}_i (\mathbf{Q}_i - \bar{\mathbf{Q}}_i) \}$ is an affine function. Thus $-\text{tr} \{ \mathbf{B}_i (\mathbf{Q}_i - \bar{\mathbf{Q}}_i) \}$ and $-\mu_i (\text{tr} \{ \mathbf{Q}_i \} - \bar{P}_i)$ are also concave. This makes $\mathbf{L}(\mathbf{Q}_i, \mu_i)$ a concave problem (see [2]). We now proceed to solve this convex optimization problem.

We derive the optimal transmit directions for subcarrier i along the same lines as [23],[18]. The dual function for the Lagrangian (3.17) is

$$(3.18) \quad \mathcal{D}(\mu_i) = \max_{\mathbf{Q} \geq 0} \mathbf{L}(\mathbf{Q}, \mu_i)$$

In what follows, we will first obtain the dual \mathcal{D} by maximizing over \mathbf{Q} . Once this is done, the optimal solution is found by minimizing the dual problem.

Let $\mathbf{A}_i = \mathbf{H}_{0i}^H \mathbf{R}_i^{-1} \mathbf{H}_{0i}$. Taking $\mathbf{Q}_i = \mathbf{V}_i \Lambda_i \mathbf{V}_i^H$, where \mathbf{V}_i is a square matrix of dimension N_t with unit norm columns and Λ_i be a diagonal matrix with non-negative entries that represent the power allocation across the different transmit streams. Ignoring the constant terms, the maximization may be written as

$$(3.19) \quad \max_{\mathbf{V}_i} \log |\mathbf{I} + \mathbf{V}_i^H \mathbf{A}_i \mathbf{V}_i \Lambda_i| - \text{tr} \left\{ \mathbf{V}_i^H (\mathbf{B}_i + \mu_i \mathbf{I}) \mathbf{V}_i \Lambda_i \right\}$$

Note that \mathbf{B}_i is symmetric positive semi-definite and hence, so is $\mathbf{B}_i + \mu_i \mathbf{I}$. We can then define the Cholesky decomposition for $\mathbf{B}_i + \mu_i \mathbf{I}$ as $\mathbf{W}\mathbf{W}^H$ where \mathbf{W} is a lower-triangular Cholesky factor. Define $\tilde{\mathbf{V}}_i = \mathbf{W}^H \mathbf{V}_i$. Equation (3.19) may be rewritten as

$$(3.20) \quad \max_{\tilde{\mathbf{V}}_i} \log |\mathbf{I} + \tilde{\mathbf{V}}_i^H \mathbf{W}^{-1} \mathbf{A}_i \mathbf{W}^{-H} \tilde{\mathbf{V}}_i \Lambda_i| - \text{tr} \left\{ \tilde{\mathbf{V}}_i \tilde{\mathbf{V}}_i^H \Lambda_i \right\}$$

Let the eigen decomposition of $\mathbf{W}^{-1} \mathbf{A}_i \mathbf{W}^{-H}$ be $\mathbf{U}\Sigma\mathbf{U}^H$, where \mathbf{U} is a unitary matrix. Then if $\tilde{\mathbf{Q}}_i = \mathbf{U}^H \tilde{\mathbf{V}}_i \Lambda_i \tilde{\mathbf{V}}_i^H \mathbf{U}$, equation (3.20) may be rewritten as

$$(3.21) \quad \max_{\tilde{\mathbf{Q}}_i \geq 0} \log |\mathbf{I} + \Sigma \tilde{\mathbf{Q}}_i| - \text{tr} \left\{ \tilde{\mathbf{Q}}_i \right\}$$

By Hadamard inequality ([5, p.279]), the optimal $\tilde{\mathbf{Q}}_i$ has to be diagonal. Hence, $\tilde{\mathbf{U}}^H \tilde{\mathbf{V}}_i \Lambda_i^{\frac{1}{2}} = \tilde{\mathbf{Q}}_i^{\frac{1}{2}} = \mathbf{U}^H \mathbf{W}^H \mathbf{V}_i \Lambda_i^{\frac{1}{2}}$. By direct substitution, it is easy to see that $\mathbf{V}_i^H (\mathbf{B}_i + \mu_i \mathbf{I}) \mathbf{V}_i \Lambda_i = \tilde{\mathbf{Q}}_i$. Now, $\mathbf{V}_i^H \mathbf{A}_i \mathbf{V}_i \Lambda_i = \tilde{\mathbf{Q}}_i \Sigma$.

Thus the optimal \mathbf{V}_i diagonalizes both $\mathbf{B}_i + \mu_i \mathbf{I}$ and \mathbf{A}_i and can be interpreted as a solution for the generalized eigenmatrix condition ([15])

$$(3.22) \quad \mathbf{A}_i \mathbf{V}_i = (\mathbf{B}_i + \mu_i \mathbf{I}) \mathbf{V}_i \Sigma$$

While (3.22) provides the directions for transmission, the optimal power allocation Λ_i has to be determined. This can be done as follows. The Lagrangian in equation (3.17) may be rewritten as

$$(3.23) \quad \mathbf{L}(\mathbf{Q}_i, \mu_i) = \log |\mathbf{I} + \Lambda_i \mathbf{V}_i^H \mathbf{A}_i \mathbf{V}_i| - \text{tr} \left\{ \mathbf{V}_i^H (\mathbf{B}_i + \mu_i \mathbf{I}) \mathbf{V}_i \Lambda_i \right\} + \mu_i \bar{P}_i + f_i(\bar{\mathbf{Q}}_i, \bar{\mathbf{Q}}_{-i})$$

Let $\mathbf{V}_i^H \mathbf{A}_i \mathbf{V}_i = \mathbf{D}_{1i}$, where \mathbf{D}_{1i} is a diagonal matrix as \mathbf{V}_i is generalized eigenmatrix of \mathbf{A}_i , $\mathbf{B}_i + \mu_i \mathbf{I}$. Let \mathbf{D}_{2i} be a diagonal matrix containing the diagonal elements of the matrix $\mathbf{V}_i^H \mathbf{B}_i \mathbf{V}_i$. Equation (3.23) may be rewritten as

$$(3.24) \quad \mathbf{L}(\mathbf{Q}_i, \mu_i) = \log |\mathbf{I} + \Lambda_i \mathbf{D}_{1i}| - \text{tr} \left\{ (\mathbf{D}_{2i} + \mu_i \mathbf{I}) \Lambda_i \right\} + \mu_i \bar{P}_i + f_i(\bar{\mathbf{Q}}_i, \bar{\mathbf{Q}}_{-i})$$

Differentiating this with respect to λ_{ij} (the j^{th} diagonal entry of Λ_i) yields the water-filling equations,

$$(3.25) \quad \frac{\mathbf{D}_{1i}(j, j)}{1 + \mathbf{D}_{1i}(j, j) \lambda_{ij}} - (\mathbf{D}_{2i}(j, j) + \mu_i) = 0$$

The optimal power allocation Λ_i may be determined as

$$(3.26) \quad \lambda_{ij} = \left[\frac{1}{\mathbf{D}_{2i}(j,j) + \mu_i} - \frac{1}{\mathbf{D}_{1i}(j,j)} \right]^+ \\ \forall j \text{ such that } \mathbf{D}_{1i}(j,j) > 0$$

where $[x]^+$ indicates $\max(x, 0)$.

The optimal μ_i can now be determined using a bisection search as λ_{ij} is monotonic in μ_i . Thus, the convex objective function f_1 can be solved iteratively until \mathbf{Q}_i converges.

3.3.2 Power allocation across the subcarriers

After obtaining one set of updated \mathbf{Q}_i for all the subcarriers, one can now update the power allocation across the various subcarriers. Note that in this step, the optimal transmit directions across all the used subcarriers remain unchanged, and only the power allocation across the various transmit streams of all the used subcarriers is optimized. From [?],

$$(3.27) \quad \lambda_{ij} = \left[\frac{1}{\mathbf{D}_{2i}(j,j) + \eta} - \frac{1}{\mathbf{D}_{1i}(j,j)} \right]^+ \\ \forall i \text{ such that } \mathbf{D}_{1i}(j,j) > 0$$

The optimal η can now be determined using a bisection search as λ_{ij} is monotonic in η . Once all the λ_{ij} across all the subcarriers and their transmit streams are obtained, this is in turn used to update the transmit covariance matrix \mathbf{Q}_i and the power allocation P_i of each used subcarrier i .

3.3.3 Optimization of window parameters - Gradient descent

Once Tx covariance matrices \mathbf{Q}_i have been computed for all the subcarriers, we perform a gradient search to optimize the window parameters. We limit the optimization to the parameters w_i , $i \in -N_e, \dots, -1$ as the window parameters w_{N+i} may be determined to satisfy the Nyquist criterion.

$$(3.28) \quad \max_{w_i, i \in (-N_e \dots -1)} C = \sum_{k=0}^{N-1} \log |\mathbf{I} + \mathbf{H}_{0k} \mathbf{Q}_k \mathbf{H}_{0k}^H \mathbf{R}_k^{-1}|$$

Following the steps in [17],

$$(3.29) \quad \frac{\partial C}{\partial w_i^*} = \text{tr} \{ (\mathbf{I} + \mathbf{H}_{0k} \mathbf{Q}_k \mathbf{H}_{0k}^H \mathbf{R}_k^{-1})^{-1} \\ \left(\sum_{k=0}^{N-1} \mathbf{H}_{0k} \mathbf{Q}_k \left(\mathbf{H}_{1k}^H \frac{\partial \xi^H(0)}{\partial w_i^*} - \mathbf{H}_{0k}^H \mathbf{R}_k^{-1} \frac{\partial \mathbf{R}_k^{-1}}{\partial w_i^*} \right) \mathbf{R}_k^{-1} \right) \}$$

$$(3.30) \quad \frac{\partial \mathbf{R}_k^{-1}}{\partial w_i^*} = \sum_{l=0, l \neq k}^{N-1} \xi((l-k)_N) \frac{\partial \xi^H((l-k)_N)}{\partial w_i^*} \mathbf{H}_{1l} \mathbf{Q}_l \mathbf{H}_{1l}^H + \\ e_k^T \mathbf{F}_N \mathbf{T}_{cp}^T \mathbf{D}_w \frac{\partial \mathbf{D}_w^H}{\partial w_i^*} \mathbf{T}_{cp} \mathbf{F}_N^H e_k \mathbf{I}_{N_r}$$

$$(3.31) \quad \frac{\partial \xi^H((l-k)_N)}{\partial w_i^*} = e_l^T \mathbf{F}_N \mathbf{T}_{cp}^T \mathbf{D}_b \frac{\partial \mathbf{D}_w^H}{\partial w_i^*} \mathbf{T}_{cp} \mathbf{F}_N^H e_k$$

The matrix $\frac{\partial \mathbf{D}_w^H}{\partial w_i^*}$ is a diagonal matrix with unity at the i^{th} diagonal element, -1 at $(N+i)^{\text{th}}$ diagonal element, and zeros everywhere else. i.e., $\frac{\partial \mathbf{D}_w^H}{\partial w_i^*} = \text{diag}(0, \dots, 1, 0, \dots, -1, 0, \dots)$. The iterative update of the window parameters is now performed as

$$(3.32) \quad w_i = w_i + \varepsilon \frac{\partial C}{\partial w_i^*}, i \in -N_e \dots -1$$

where ε is a suitable positive step size for the gradient algorithm.

3.3.4 Overall Algorithm and Convergence

The overall algorithm that solves f_0 is summarized in Table 3.1. The overall algorithm alternates between the transmit precoder optimization and the window coefficient optimization. At every iteration of the transmit precoder, a convex sub-problem f_1 is created and optimized based on the updated value of $\mathbf{Q}_i, \mathbf{Q}_{-i}$ from the last iteration. A power allocation across all the subcarriers is performed at the end of one round of transmit covariance update for all subcarriers. The window optimization is based on the gradient search method.

The non-decreasing behavior of the algorithm in Table 3.1 is now shown below on the same lines as in [38]. Let $\bar{\mathbf{Q}}_i$ be the current value of \mathbf{Q}_i at the beginning of an iteration, and let \mathbf{Q}_i^* be the updated value. Then,

$$(3.33) \quad \begin{aligned} f_0(\bar{\mathbf{Q}}_i, \bar{\mathbf{Q}}_{-i}) &= f_1(\bar{\mathbf{Q}}_i, \bar{\mathbf{Q}}_{-i}) \\ &\leq f_1(\mathbf{Q}_i^*, \bar{\mathbf{Q}}_{-i}) \\ &\leq f_0(\mathbf{Q}_i^*, \bar{\mathbf{Q}}_{-i}) \end{aligned}$$

where the first equality can be observed to be true by direct inspection whenever $\mathbf{Q}_i = \bar{\mathbf{Q}}_i$. The first inequality is because \mathbf{Q}_i^* is the result of optimization in 3.3.1, and the second inequality is due to Proposition 1. This shows that the transmit covariance update is non-decreasing.

The iterations for optimization of \mathbf{Q}_i and power allocations are steps in cyclic minimization (actually maximization in this problem, also see [38]). Thus the overall algorithm in Table 3.1 results in a non-decreasing updated value of f_0 at each step of the iteration. This ensures convergence to a maximum value.

3.4 Simulation Results

We consider a MIMO fading channel based on equation (3.7). A single user MIMO scenario with a signal to AWGN noise ratio of 20dB is considered. For every Tx-Rx pair, finite impulse

Table 3.1: Overall Algorithm to solve objective function f_0

<p>Initialize window parameters using raised cosine filter coefficients for $k = 0, 1 \dots N - 1$</p> <p>Initialize $P_k = \frac{P}{N_u} \mathbf{I}$ and $\mathbf{Q}_k = \frac{P_k}{N_t} \mathbf{I}$</p> <p>Initialize $\mathbf{R}_{\mathbf{v}_k} = (e_k^T \mathbf{F}_N \mathbf{T}_{ex}^T \mathbf{D}_w \mathbf{D}_w^H \mathbf{T}_{ex} \mathbf{F}_N^H e_k) \mathbf{I}_{N_r}$</p> <p>Initialize $\mathbf{R}_{\bar{k}} = \mathbf{R}_{\mathbf{v}_k} + \sum_{l=0, l \neq k}^{N-1} \xi((l-k)_N) ^2 \mathbf{H}_{1k} \mathbf{Q}_l \mathbf{H}_{1k}^H$</p> <p>Initialize $\mathbf{H}_{0k} = \{\hat{\mathbf{H}}_{0k} + \mathbf{H}_{1k} \xi(0)\}$</p> <p>Repeat until convergence</p> <p>Perform Tx precoder optimization</p> <p>Repeat until convergence</p> <p>for $i = 0, 1 \dots N - 1$</p> <p>Repeat until convergence</p> <p>$\mathbf{R}_{\bar{i}} = \mathbf{I} + \sum_{l=0, l \neq i}^{N-1} \xi((i-l)_N) ^2 \mathbf{H}_{1i} \mathbf{Q}_l \mathbf{H}_{1i}^H$</p> <p>Compute $\mathbf{A}_i = \mathbf{H}_{0i}^H \mathbf{R}_{\bar{i}}^{-1} \mathbf{H}_{0i}$</p> <p>Compute $\mathbf{B}_i = \sum_{l \neq i} \Xi_{l,i} ^2 \mathbf{H}_{1l} \{ \mathbf{R}_{\bar{l}}^{-1} - (\mathbf{R}_{\bar{l}} + \mathbf{H}_{0l} \mathbf{Q}_l \mathbf{H}_{0l}^H)^{-1} \} \mathbf{H}_{1l}^H$</p> <p>Set $\underline{\mu}_i = 0, \bar{\mu}_i = \mu_{max}$</p> <p>Repeat until convergence</p> <p>$\mu_i = \frac{\underline{\mu}_i + \bar{\mu}_i}{2}$</p> <p>Compute the generalized eigenmatrix of \mathbf{A}_i and $\mathbf{B}_i + \mu_i \mathbf{I}$</p> <p>Normalize the generalized eigenmatrix to have unit norm; denote it as \mathbf{V}_i.</p> <p>Set $\mathbf{D}_{1i} = \mathbf{V}_i \mathbf{A}_i \mathbf{V}_i^H, \mathbf{D}_{2i} = \text{diag}(\mathbf{V}_i \mathbf{B}_i \mathbf{V}_i^H)$</p> <p>Compute the transmit powers, $\lambda_{ij} = \left[\frac{1}{\mathbf{D}_{2i(j,j)} + \mu_i} - \frac{1}{\mathbf{D}_{1i(j,j)}} \right]^+$</p> <p>If any diagonal entries of \mathbf{D}_{1i} are zero, corresponding λ_{ij} is set to zero.</p> <p>if $\text{tr}(\Lambda_i) > P_i$, set $\underline{\mu}_i = \mu_i$, else set $\bar{\mu}_i = \mu_i$</p> <p>Set $\mathbf{Q}_i = \mathbf{V}_i \Lambda_i \mathbf{V}_i^H$</p> <p>Perform power allocation update</p> <p>Set $\eta = 0, \bar{\eta} = \eta_{max}$</p> <p>Repeat until convergence</p> <p>$\eta = \frac{\eta + \bar{\eta}}{2}$</p> <p>for $l = 0, 1 \dots N - 1$</p> <p>Set $\mathbf{D}_{1l} = \mathbf{V}_l \mathbf{A}_l \mathbf{V}_l^H, \mathbf{D}_{2l} = \text{diag}(\mathbf{V}_l \mathbf{B}_l \mathbf{V}_l^H)$</p> <p>Compute the transmit powers, $\lambda_{lj} = \left[\frac{1}{\mathbf{D}_{2l(j,j)} + \eta} - \frac{1}{\mathbf{D}_{1l(j,j)}} \right]^+$</p> <p>If any diagonal entries of \mathbf{D}_{1l} are zero, corresponding λ_{lj} is set to zero.</p> <p>if $\sum_{l=0}^{N-1} \text{tr}(\Lambda_l) > P$, set $\underline{\eta} = \eta$, else set $\bar{\eta} = \eta$</p> <p>for $l = 0, 1 \dots N - 1$</p> <p>Set $\mathbf{Q}_l = \mathbf{V}_l \Lambda_l \mathbf{V}_l^H, P_l = \text{tr}(\Lambda_l)$</p> <p>Perform window coefficient update</p> <p>Repeat until convergence</p> <p>for $i = -N_e, \dots, -1$</p> <p>$w_i = w_i + \varepsilon \frac{\partial C}{\partial w_i^*}$ and $w_{N+i} = 1 - w_i$</p> <p>for $k = 0, 1 \dots N - 1$</p> <p>$\mathbf{R}_{\mathbf{v}_k} = e_k^T \mathbf{F}_N \mathbf{T}_{cp}^T \mathbf{D}_w \mathbf{D}_w^H \mathbf{T}_{cp} \mathbf{F}_N^H e_k \mathbf{I}_{N_r}$</p> <p>$\mathbf{R}_{\bar{k}} = \mathbf{R}_{\mathbf{v}_k} + \sum_{l=0, l \neq k}^{N-1} \xi((l-k)_N) ^2 \mathbf{H}_{1k} \mathbf{Q}_l \mathbf{H}_{1k}^H$</p> <p>$\mathbf{H}_{0k} = \{\hat{\mathbf{H}}_{0k} + \mathbf{H}_{1k} \xi(0)\}$</p>
--

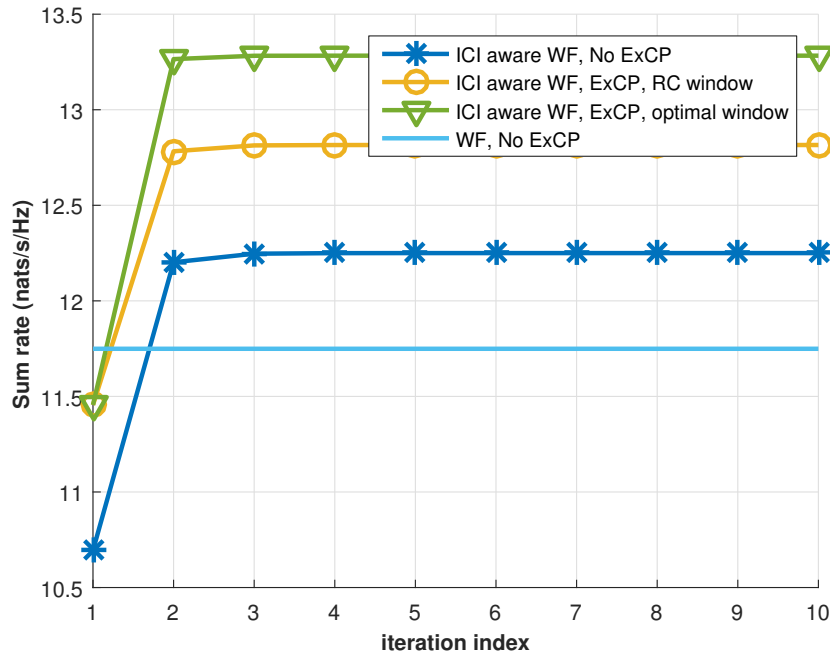


Figure 3.3: Simulation Results with $N_t = 4, N_r = 3, N = 64, N_e = 16$ and Doppler of 450Kmph

response (FIR) Rayleigh fading channels are generated independently with the power delay profile (PDP) as $[0 -5 -5]$ in dB for \mathbf{h}_0 and \mathbf{h}_1 . An LTE OFDM system operating at unlicensed 2.4GHz band is considered with 15KHz of channel spacing. A Doppler frequency corresponding to 450kmph is assumed. The entries of \mathbf{h}_1 are scaled such that the overall ICI power experienced at any receive antenna corresponds to a Doppler frequency shift of 450kmph. The capacity of the iterative scheme under different scenarios is considered. In the simulation results presented, all subcarriers are assumed to be used. For the gradient search, a step size of 0.01 is used. A single iteration of the window optimization itself has 100 steps of equation (3.32). The raised cosine window used for initialization is the same as in [11].

Figure 3.3 shows a scenario with $N_t = 4$ transmit antennas and $N_r = 3$ receive antennas. We consider $N = 64, N_e = 16$. The sum rate with a naive water filling approach that takes into account neither the ICI nor the ExCP is shown by the curve "WF, No ExCP". The curve "ICI aware WF, No ExCP" shows the merit in just accounting for the ICI while designing the precoder even if the ExCP is not exploited. The performance with the exploitation of the ExCP and a raised cosine window is shown by the curve "ICI aware WF, ExCP RC window". Finally, the performance with the optimal window obtained as explained in Section 3.3.3 is given by the curve "ICI aware WF, ExCP optimal window". The corresponding window roll off is given in Figure 3.4. To improve the clarity of the figure, only subcarrier numbers from -15 to +15 are displayed. "No Excess CP" corresponds to the scenario where ExCP is not exploited. "Excess CP raised cosine" refers to raised cosine window being used for ExCP. It is very clearly seen that the optimal window

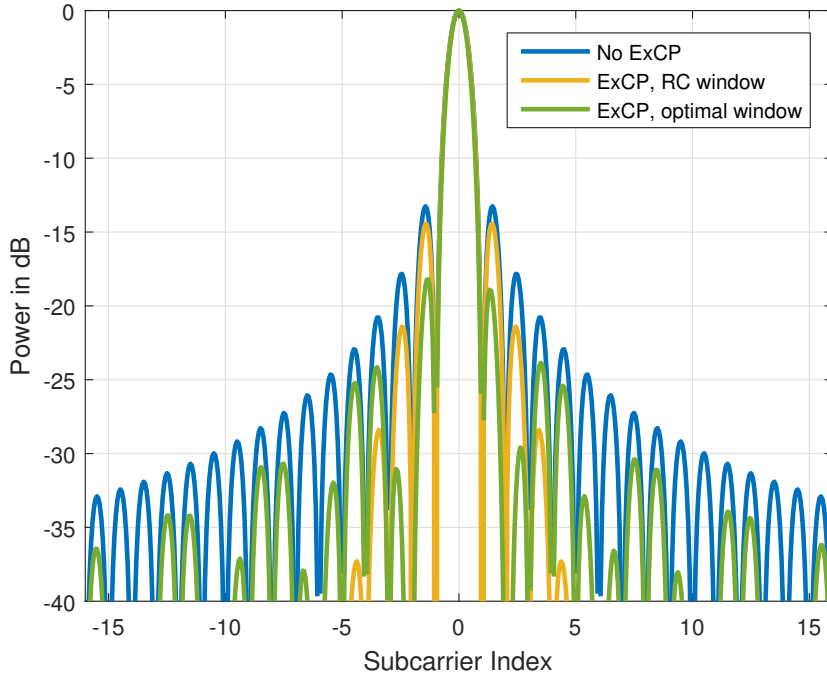


Figure 3.4: Comparison of windows used to exploit ExCP. $N_t = 4, N_r = 3, N = 64, N_e = 16$.

does a good side lobe reduction for the closest side lobes and does not over attenuate the farther side lobes, as done by the raised cosine window. This is quite intuitive too and explains why the optimal window performs superior to the raised cosine window.

Figure 3.5 shows a scenario with $N_t = 3$ transmit antennas and $N_r = 3$ receive antennas. We consider again, $N = 64, N_e = 16$ and the trend is similar to that in Figure 3.3. Figure 3.6 gives the roll-off obtained for the optimized window in comparison with other windows for the same scenario and once again, the optimal window strikes a better balance compared to the raised cosine window.

Comparing the Figures 3.3 and 3.5, we also observe that when the number of transmit antennas is higher, there is a greater gain in performing an ICI aware water-filling relative to the naive water-filling. This can be seen by observing the corresponding sum rate curves in the absence of the ExCP. This is in agreement with our motivation to exploit transmit antennas to mitigate the impact of ICI. I.e, more the number of transmit antennas, greater is the impact on the mitigation of ICI. In the simulation scenarios considered, we also see that the iterations always exhibit a non-decreasing behavior in the capacity as is predicted by the theory (section 3.3.4).

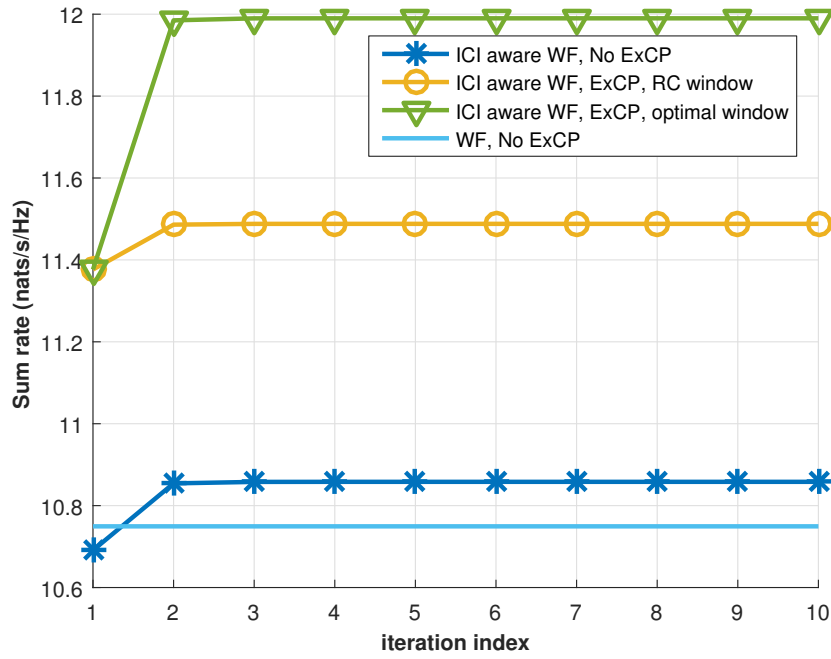


Figure 3.5: Simulation Results with $N_t = 3, N_r = 3, N = 64, N_e = 16$, and Doppler of 450Kmph

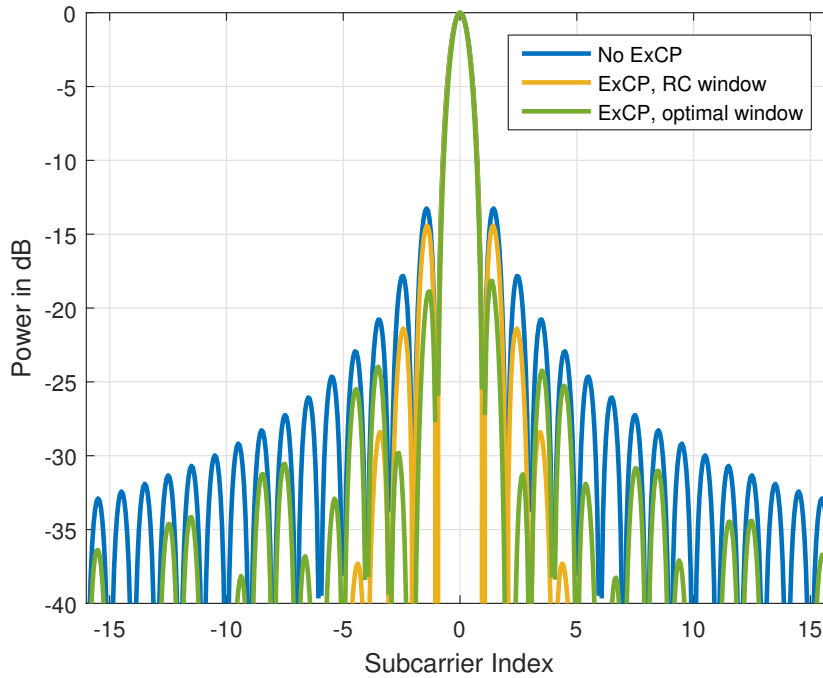


Figure 3.6: Comparison of windows used to exploit ExCP. $N_t = 3, N_r = 3, N = 64, N_e = 16$

3.5 Summary of Contributions

- We tackle the problem of designing the optimal precoders for a MIMO point to point link under high Doppler.
- Towards this, we first justify a linear approximation for the channel variation across the OFDM symbol.
- We come up with a good system model that can include the effect of the linear channel variation and the receive windowing using the ExCP.
- The system model reveals that the problem is similar to that of precoder design for a MIMO IBC with an additional receive window coefficients to be optimized as well.
- Due to the similarity of the problem with MIMO IBC, we take advantage of the difference of concave approach in [23].
- We re-interpret the approach in [23] as an instance of the majorization technique [38].
- The window optimization is performed via alternating minimization.
- We prove the convergence of the entire design.
- The work detailed here resulted in the publications [?], [?].

PRECODER DESIGN UNDER DOPPLER - PARTIAL CSIT

4.1 System Model

In chapter 3, complete knowledge of the channel was assumed at the Tx. In this chapter, we relax that assumption and look at ways to incorporate imperfect knowledge of CSIT. Consider a finite delay spread path wise MIMO channel model in the time domain as follows.

$$(4.1) \quad \mathcal{H}(\tau, t) = \underbrace{\mathcal{H}_r(\tau)\mathcal{D}(\tau, t)\mathcal{H}_t^T(\tau)}_{\text{Deterministic path wise model}} + \underbrace{\tilde{\mathcal{H}}(\tau, t)}_{\text{random part}}$$

where \mathcal{H}_r contains as columns the receive side path antenna array responses. Similarly, \mathcal{H}_t contains as columns the transmit side path antenna array responses. $\mathcal{D}(\tau, t)$ is a diagonal matrix that captures the path amplitudes and the Doppler variations of the different paths and is given by $D(\tau, t) = \text{diag}(A_1 e^{j2\pi f_1 t} \delta(\tau - \tau_1), A_2 e^{j2\pi f_2 t} \delta(\tau - \tau_2), \dots)$, where f_i are the Doppler frequencies, A_i are the complex path amplitudes and τ_i are the path delays. Note here that the time dependency (Doppler dependency) is limited to the diagonal matrix \mathcal{D} . i.e. other than the influence of the Doppler, the rest of the components are slow fading. The knowledge of the deterministic path may be obtained in two different ways.

As we are talking about the channel from a fixed BS to an HST that runs on a rail network, one possibility is to use location aided information to obtain the path delay, amplitudes and Doppler corresponding to the deterministic path-wise model. This information could be updated in a location indexed database.

Alternatively, we could assume that the transmitter is capable of estimating precisely the components of the deterministic part of the channel - A_i , τ_i and f_i . $\tilde{\mathcal{H}}(\tau, t)$ corresponds to the unknown random part of the channel and is the cause for partial CSIT at the transmitter. Using a precise estimate of $\mathcal{H}_r(\tau)\mathcal{D}(\tau, t)\mathcal{H}_t^T(\tau)$ at time t , the transmitter predicts a future instance of

the channel at a time offset of Δ as $\mathcal{H}_r(\tau)\mathcal{D}(\tau, t + \Delta)\mathcal{H}_t^T(\tau)$ assuming all components other than the Doppler for the deterministic channel component remain constant over the Δ time duration. Thus, for the OFDM symbol for which the precoder has to be designed, the transmitter has the channel estimate corresponding to the deterministic part of the channel.

$$(4.2) \quad \hat{\mathcal{H}}(\tau, t + \Delta) = \mathcal{H}_r(\tau)\mathcal{D}(\tau, t + \Delta)\mathcal{H}_t^T(\tau) = \mathcal{H}(\tau, t + \Delta) - \underbrace{\tilde{\mathcal{H}}(\tau, t + \Delta)}_{\text{random error}}$$

Now, as in chapter 3, the time variation across the OFDM symbol of interest is approximated to be linear. Thus, let $\mathcal{H}_0(\tau, t + \Delta)$ be the mean of the channel and $\mathcal{H}_1(\tau, t + \Delta)$ the linear time variation. After FFT at the receiver, the received data at each subcarrier would be of the following form,

$$(4.3) \quad \mathbf{y}_k = \mathbf{H}_{0k}\mathbf{d}_k + \sum_{l=0, l \neq k}^{N-1} \mathbf{H}_{1l}\mathbf{d}_l \xi((k-l)_N) + \mathbf{v}_k.$$

\mathbf{H}_{0k} (dimension $N_r \times N_t$) is the mean frequency domain channel observed at subcarrier k and is a result of $\mathcal{H}_0(t + \Delta, \tau)$. The second term in (4.3) represents the ICI (inter-carrier interference) caused by time variance due to Doppler. \mathbf{H}_{1k} is the frequency domain channel component corresponding to $\mathcal{H}_1(t + \Delta, \tau)$ at subcarrier k , $\mathbf{d}_k = [d_k(1) \cdots d_k(N_t)]^T$ is the $N_t \times 1$ vector of transmitted data symbols on the carrier k . \mathbf{v}_k is the $N_r \times 1$ vector of AWGN (additive white Gaussian noise) noise observed at carrier index k . The covariance of \mathbf{v}_k is normalized to be the identity matrix.

$$(4.4) \quad \xi((k-l)_N) = \frac{1}{N} \sum_{n=0}^{N-1} \left(n - \frac{N-1}{2} \right) e^{j2\pi(k-l)\frac{n}{N}}$$

Now, the prediction errors that result from the unpredictable part of the channel result in errors in $\hat{\mathcal{H}}_0(t + \Delta, \tau)$, $\hat{\mathcal{H}}_1(t + \Delta, \tau)$ - the estimates of $\mathcal{H}_0(t + \Delta, \tau)$, $\mathcal{H}_1(t + \Delta, \tau)$. Correspondingly $\hat{\mathbf{H}}_{0k}$, $\hat{\mathbf{H}}_{1k}$ (the estimates of \mathbf{H}_{0k} , \mathbf{H}_{1k}) are also in error. Therefore, to proceed further with the Tx precoder design under partial CSIT, we need a model for the errors in the estimates for \mathbf{H}_{0k} , \mathbf{H}_{1k} .

The unpredicted part of (3.7) is assumed to have a separable (Kronecker) model for each path delay of the FIR channel model. In the Kronecker model, the correlation between any two elements of the MIMO channel matrix may be expressed separately as a product of the transmit and receive side correlations [27]. Hence, after the FFT at the receiver (a linear operation) at each subcarrier k in the frequency domain,

$$(4.5) \quad \hat{\mathbf{H}}_{0k} = \mathbf{H}_{0k} - \mathbf{C}_r^{\frac{1}{2}} \tilde{\mathbf{H}}_{0k} \mathbf{C}_t^{\frac{1}{2}} \quad \hat{\mathbf{H}}_{1k} = \mathbf{H}_{1k} - \beta \mathbf{C}_r^{\frac{1}{2}} \tilde{\mathbf{H}}_{1k} \mathbf{C}_t^{\frac{1}{2}}$$

where $\mathbf{C}_r, \mathbf{C}_t$ are the receive and transmit side covariances for the error term. The elements of $\tilde{\mathbf{H}}_{0k}, \tilde{\mathbf{H}}_{1k}$ are i.i.d $\sim \mathcal{CN}(0, 1)$. Note that as the different channel taps are independent, the covariance matrices are subcarrier independent. β is a real number that signifies the extent of Doppler. As in 3, the transmit precoder is designed to maximize the weighted sum rate (WSR). Let the transmit covariance matrix of subcarrier k be $\mathbf{Q}_k = \mathbf{E}(\mathbf{d}_k \mathbf{d}_k^H) = \mathbf{G}_k \mathbf{G}_k^H$ where $\mathbf{E}(\cdot)$ is the

expectation operator. Thus, the WSR of this MIMO system across all the subcarriers in the presence of both ICI and AWGN noise would be given as $\text{WSR} = \sum_{k=0}^{N-1} \log |\mathbf{I} + \mathbf{G}_k^H \mathbf{H}_{0k}^H \mathbf{R}_k^{-1} \mathbf{H}_{0k} \mathbf{G}_k|$, where $\mathbf{R}_k = \mathbf{I} + \sum_{l=0, l \neq k}^{N-1} |\zeta((k-l)_N)|^2 \mathbf{H}_{1l} \mathbf{Q}_l \mathbf{H}_{1l}^H$. Note that this formulation can include guard subcarriers and DC subcarrier by simply forcing their respective transmit covariances to zero. Indeed, in this formulation for WSR, the weights are all unity, but this is done only to simplify the notation and help focus on the main part of the work. However, as the CSIT is imperfect, to derive a Tx precoder that is robust to the imperfections in CSIT, various optimization criterion could be considered, such as outage capacity. Here, we shall consider another commonly used metric - EWSR.

(4.6)

$$\text{EWSR} = \sum_{k=0}^{N-1} \mathbf{E}_{(\mathbf{H}_{0k}, \mathbf{H}_{1k})}(\widehat{\mathbf{H}}_{0k}, \widehat{\mathbf{H}}_{1k}) \log |\mathbf{I} + \mathbf{G}_k^H \mathbf{H}_{0k}^H \mathbf{R}_k^{-1} \mathbf{H}_{0k} \mathbf{G}_k| \quad \text{subject to} \quad \sum_{k=0}^{N-1} \text{tr} \{ \mathbf{G}_k \mathbf{G}_k^H \} \leq P.$$

4.2 Large MIMO asymptotics

The key difficulty with the optimization problem in (4.6) is the presence of the expectation operator. In this section, to tackle (4.6), we pursue the large MIMO asymptotics and alternating optimization for multi-user systems in [24], which are based on the single-user MIMO asymptotics of [39], [8] in which both $N_t, N_r \rightarrow \infty$ at a constant ratio. This approach tends to give good approximations even when N_t and N_r are not very large. Some alternative approaches are pursued later in chapter 5. Note that

$$(4.7) \quad \log |\mathbf{I} + \mathbf{G}_k^H \mathbf{H}_{0k}^H \mathbf{R}_k^{-1} \mathbf{H}_{0k} \mathbf{G}_k| = \log |\mathbf{I} + \mathbf{H}_{0k} \mathbf{Q}_k \mathbf{H}_{0k}^H \mathbf{R}_k^{-1}| = \log |\mathbf{R}_k| - \log |\mathbf{R}_k^-|$$

where $\mathbf{R}_k = \mathbf{R}_k^- + \mathbf{H}_{0k} \mathbf{Q}_k \mathbf{H}_{0k}^H$. For the general case of Gaussian CSIT with separable covariance (which is indeed our case as is seen in (4.5)), we can write

$$(4.8) \quad \mathbf{H} = \overline{\mathbf{H}} + \mathbf{C}_{rx}^{\frac{1}{2}} \widetilde{\mathbf{H}} \mathbf{C}_{tx}^{\frac{1}{2}}$$

where $\overline{\mathbf{H}} = \mathbf{E}(\mathbf{H})$, and the elements of $\widetilde{\mathbf{H}}$ are i.i.d $\sim \mathcal{CN}(0, 1)$. \mathbf{C}_{tx} and \mathbf{C}_{rx} are the Tx and Rx side covariances respectively. [39], [8] lead to asymptotic expressions of the form

$$(4.9) \quad \mathbf{E}_{\mathbf{H}} \log |\mathbf{I} + \mathbf{H} \mathbf{Q} \mathbf{H}^H| = \max_{z \geq 0, w \geq 0} \left\{ \log \left| \begin{array}{c|c} \mathbf{I} + w \mathbf{C}_{rx} & \overline{\mathbf{H}} \\ \hline -\mathbf{Q} \overline{\mathbf{H}}^H & \mathbf{I} + z \mathbf{Q} \mathbf{C}_{tx} \end{array} \right| - zw \right\}$$

To get the terms in (4.6) into the format of (4.9), at the level of each subcarrier k , we stack the channel estimates relevant for each subcarrier k . Let the resulting transmit and receiving covariances of these augmented matrices at each subcarrier k be denoted as $\mathbf{C}_{tx,k}$, and $\mathbf{C}_{rx,k}$.

$$(4.10) \quad \begin{aligned} \mathbf{H}_k &= [\mathbf{H}_{1,0} \xi(k) \cdots \mathbf{H}_{1,k-1} \xi(1) \mathbf{H}_{0k} \mathbf{H}_{1,k+1} \xi(N-1) \cdots] = \overline{\mathbf{H}}_k + \mathbf{C}_{rx,k}^{\frac{1}{2}} \widetilde{\mathbf{H}}_k \mathbf{C}_{tx,k}^{\frac{1}{2}} \\ \mathbf{C}_{tx,k} &= \text{diag}\{\gamma_{k,0} \cdots \gamma_{k,k-1} \mathbf{1} \gamma_{k,k+1} \cdots \gamma_{k,N-1}\} \otimes \mathbf{C}_t. \\ \mathbf{C}_{rx,k} &= \mathbf{C}_r. \end{aligned}$$

where the elements of $\tilde{\mathbf{H}}_k$ are i.i.d $\sim \mathcal{CN}(0,1)$ and $\bar{\mathbf{H}}_k$ refers to the mean part of \mathbf{H}_k . $\gamma_{k,l} = \beta^2 |\xi((k-l)_N)|^2$ and \otimes refers to the Kronecker product. Let \mathbf{Q} be a block diagonal matrix with the each diagonal block being \mathbf{Q}_k . $\mathbf{Q}_{\bar{k}}$ is similar to \mathbf{Q} but with the k^{th} block diagonal set to all zeros. Then,

$$(4.11) \quad \mathbf{R}_k = \mathbf{I} + \mathbf{H}_k \mathbf{Q} \mathbf{H}_k^H, \quad \mathbf{R}_{\bar{k}} = \mathbf{I} + \mathbf{H}_k \mathbf{Q}_{\bar{k}} \mathbf{H}_k^H.$$

Equation (4.6) now becomes (under large MIMO asymptotics),

$$(4.12) \quad \text{EWSR} = \sum_{k=0}^{N-1} \left(\max_{z_k, w_k \geq 0} \{\log |\mathbf{S}_k(\mathbf{Q}, z_k, w_k)| - z_k w_k\} - \max_{z_{\bar{k}}, w_{\bar{k}} \geq 0} \{\log |\mathbf{S}_k(\mathbf{Q}_{\bar{k}}, z_{\bar{k}}, w_{\bar{k}})| - z_{\bar{k}} w_{\bar{k}}\} \right)$$

where

$$(4.13) \quad \mathbf{S}_k(\mathbf{Q}, z_k, w_k) = \begin{bmatrix} \mathbf{I} + w_k \mathbf{C}_r & \bar{\mathbf{H}}_k \\ -\mathbf{Q} \bar{\mathbf{H}}_k^H & \mathbf{I} + z_k \mathbf{Q} \mathbf{C}_{tx,k} \end{bmatrix}$$

Further, by the rules of determinant for block matrices

$$(4.14) \quad \log |\mathbf{S}_k(\mathbf{Q}, z_k, w_k)| = \log |\mathbf{I} + w_k \mathbf{C}_r| + \log |\mathbf{I} + \mathbf{Q} \mathbf{T}_k(z_k, w_k)|$$

where $\mathbf{T}_k(z_k, w_k) = z_k \mathbf{C}_{tx,k} + \bar{\mathbf{H}}_k^H (\mathbf{I} + w_k \mathbf{C}_r)^{-1} \bar{\mathbf{H}}_k$ can be seen as some kind of generalized Tx side channel covariance matrix.

4.2.1 Precoder Design

The overall optimization involves several iterations of alternating optimization over $\mathbf{Q}_k, z_k, w_k, z_{\bar{k}}, w_{\bar{k}}$. To determine the \mathbf{Q}_k , we observe the following:

$$(4.15) \quad \begin{aligned} \log |\mathbf{I} + \mathbf{Q} \mathbf{T}_k(z_k, w_k)| &= \log |\mathbf{I} + \sum_{l=1}^N \mathcal{J}_l \mathbf{Q}_l \mathcal{J}_l^H \mathbf{T}_k(z_k, w_k)| \\ &= \log |\bar{\mathbf{R}}_{k,\bar{k}}| + \log |\mathbf{I} + \mathbf{Q}_k \mathcal{J}_k^H \mathbf{T}_k(z_k, w_k) \bar{\mathbf{R}}_{k,\bar{k}}^{-1} \mathcal{J}_k|, \end{aligned}$$

where $\bar{\mathbf{R}}_{k,\bar{k}} = \mathbf{I} + \sum_{l \neq k} \mathcal{J}_l \mathbf{Q}_l \mathcal{J}_l^H \mathbf{T}_k(z_k, w_k)$, and \mathcal{J}_k is a block column vector with its block k being an identity matrix and zeros on every other block. Pre-multiplying a matrix with \mathcal{J}_k^H and post-multiplying it with \mathcal{J}_k results in the selection of k^{th} diagonal block of that matrix. Note that \mathbf{Q}_k refers to the k^{th} diagonal block of \mathbf{Q} . On the same lines as [23], split $\text{EWSR} = \text{EWSR}_k + \text{EWSR}_{\bar{k}}$. The derivative of $\text{EWSR}_{\bar{k}}$ with respect to \mathbf{Q}_k is given by,

$$(4.16) \quad \begin{aligned} \mathbf{B}_k &= -\frac{\partial \text{EWSR}_{\bar{k}}}{\partial \mathbf{Q}_k} = \mathcal{J}_k^H \left(\sum_{l \neq k} \left[\mathbf{T}_l(z_{\bar{l}}, w_{\bar{l}}) \bar{\mathbf{R}}_{\bar{l}}^{-1} - \mathbf{T}_l(z_l, w_l) \bar{\mathbf{R}}_l^{-1} \right] \right) \mathcal{J}_k. \\ \bar{\mathbf{R}}_l &= \mathbf{I} + \mathbf{Q} \mathbf{T}_l(z_l, w_l). \\ \bar{\mathbf{R}}_{\bar{l}} &= \mathbf{I} + \mathbf{Q}_{\bar{l}} \mathbf{T}_l(z_{\bar{l}}, w_{\bar{l}}). \end{aligned}$$

Table 4.1: Overall Algorithm for precoder design

Initialize $\mathbf{Q}, P_k, w_k, z_k, z_{\bar{k}}, w_{\bar{k}}$ for used subcarriers Compute $\bar{\mathbf{H}}_k$ for all used subcarriers Initialize $\mathbf{T}_k(z_k, w_k), \mathbf{T}_k(z_{\bar{k}}, w_{\bar{k}})$ for used subcarriers Repeat until convergence For every used subcarrier k Maximize alternatively $w_k, z_k, z_{\bar{k}}, w_{\bar{k}}$ (see (4.18)) Compute $\mathbf{T}_k(z_k, w_k), \mathbf{T}_k(z_{\bar{k}}, w_{\bar{k}})$ for used subcarriers For every used subcarrier k Update \mathbf{Q}_k based on (4.17) For every used subcarrier k Update power allocation P_k , see from [?]

Thus, the precoding directions are obtained as the solution for the generalized Eigenmatrix condition,

$$(4.17) \quad \mathbf{A}_k \mathbf{G}_k = (\mathbf{B}_k + \mu_k \mathbf{I}) \mathbf{G}_k \Sigma.$$

where $\mathbf{A}_k = \mathcal{J}_k^H \mathbf{T}_k(z_k, w_k) \mathbf{R}_{k, \bar{k}}^{-1} \mathcal{J}_k$. μ_k is the Lagrangian corresponding to the power constraint P_k at subcarrier k at the current stage of the iteration and Σ is a diagonal matrix with non-negative real entries. The details of power allocation across subcarriers and the interference-aware water-filling are exactly as in 3. Given \mathbf{Q} , the optimization of z_k, w_k is obtained as

$$(4.18) \quad \begin{aligned} w_k &= \text{tr}\{\mathbf{Q} \mathbf{C}_{tx} (\mathbf{I} + \mathbf{Q} \mathbf{T}_k(z_k, w_k))^{-1}\} \\ z_k &= \text{tr}\left\{ \mathbf{C}_r \left(\mathbf{I} + w_k \mathbf{C}_r + \bar{\mathbf{H}}_k (\mathbf{I} + z_k \mathbf{Q} \mathbf{C}_{tx, k})^{-1} \mathbf{Q} \bar{\mathbf{H}}_k^H \right)^{-1} \right\} \end{aligned}$$

Due to the interdependency between w_k and z_k , they have to be iterated among themselves until convergence. The equations for $z_{\bar{k}}, w_{\bar{k}}$ are similar except for \mathbf{Q} being replaced by $\mathbf{Q}_{\bar{k}}$. The overall steps are briefly summarized in Table 4.1. As always, there are multiple ways of performing the alternating optimization and this is just one possible approach. It is also illustrative to observe that in the extreme case of \mathbf{C}_r and \mathbf{C}_t being all zeros (implying perfect CSIT), equation (4.9) is satisfied with $z = 0, w = 0$ and the algorithm reduces to that given in [?].

Note, however, that the convergence of the algorithm is not guaranteed for small N_t, N_r . This is primarily due to the fact that the expression in (4.9) is only approximate at non-asymptotic values of N_t, N_r . However, we observe the algorithm to converge in the simulations presented in section 4.2.2.

4.2.2 Simulation Results

An LTE OFDM system operating at unlicensed 2.4GHz band is considered with 15KHz of channel spacing and 128 subcarriers. For every Tx-Rx pair, FIR Rayleigh fading channels are generated independently with the power delay profile (PDP) as [0 -5 -5] in dB. A Doppler frequency corresponding to 450kmph is assumed. The receive and transmit variance of the un-estimated part of the channel are chosen to be identity matrices reflecting a worst case scenario of no covariance knowledge about the un-estimated part. The total power in the un-estimated part is assumed to be 6 dB lower than the estimated portion. In the simulation results presented, all subcarriers are assumed to be used. The scale factor β in (4.5) is taken as 0.0033 corresponding to a Doppler variation of 450kmph. For every subcarrier k parameters $z_k, w_k, z_{\bar{k}}, w_{\bar{k}}$ are initialized to 0. Figure 4.1 shows the EWSR averaged across 500 different channel realizations with the proposed precoder for $N_t = 6, N_r = 3$. In other words, the EWSR is computed for each channel realization based on the available CSIT and covariance information. The EWSR thus computed for 500 channel realizations are averaged to obtain the average EWSR at a given SNR. Also shown is the performance with a naive precoder that does not take into account the unknown error part (partial CSIT) and computes the precoder using the mean predicted channel. This is also equivalent to forcing $z = 0, w = 0$ in the large system approximation. As expected, the gains from the explicit use of the partial CSIT information become more pronounced at higher SNR.

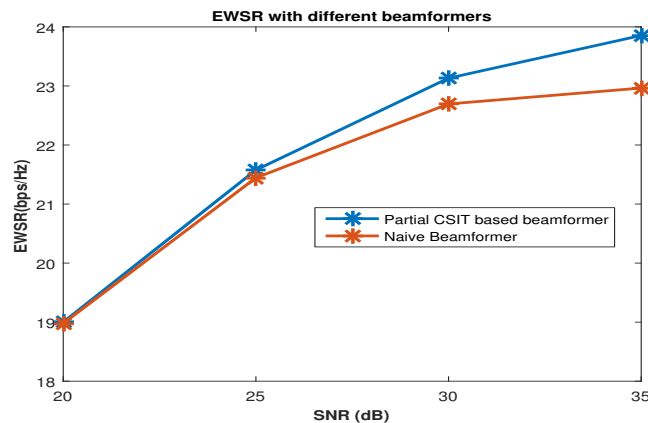


Figure 4.1: EWSR comparison for $N_t = 6, N_r = 3$

4.3 Summary of Contributions

- Extended the full CSIT results to a more relaxed setting of partial CSIT.
- Came up with a system model that facilitated the use of the Large system approximation to solve the optimization problem under partial CSIT.

- Employed large system approximation to solve the EWSR optimizing precoders which work quite well even at small values of Tx and Rx number of antennas.
- This work was published in [?].

ANALYSIS OF THE GAP BETWEEN EWSR AND ESEI-WSR

In chapter 4, EWSR optimization was tackled with the help of the large system approximation given in equation (4.9). In this chapter, we look at an alternative metric ESEI-WSR. Then, we note that for the particular, but significant, special case of MaMIMO, the EWSR converges to ESEI-WSR and this metric is more amenable to optimization. [36] considered a multi-user Multiple-Input Single-Output (MISO) scenario and proposed approximating the EWSR by ESEI-WSR. They then derived a constant bound for this approximation. We perform a refined analysis of the gap between EWSR and ESEI-WSR criteria for finite antenna dimensions to analyze the suitability of this approximation. Noting, however, that the sum rate optimization for the Doppler scenario is identical to that encountered in a MIMO IBC scenario as well (see section 3.3), we formulate the problem directly for a MIMO IBC scenario, so as to cover a wider range of problems.

5.1 MIMO IBC Signal Model

Consider an IBC with C cells and a total of K users with d_k streams per user. We shall consider a system-wide numbering of the users. User k has N_k antennas and is served by BS b_k . The $N_k \times 1$ received signal at user k in cell b_k is,

$$(5.1) \quad \mathbf{y}_k = \underbrace{\mathbf{H}_{k,b_k} \mathbf{G}_k \mathbf{x}_k}_{\text{signal}} + \underbrace{\sum_{\substack{i \neq k \\ b_i = b_k}} \mathbf{H}_{k,b_k} \mathbf{G}_i \mathbf{x}_i}_{\text{intracell interf.}} + \underbrace{\sum_{j \neq b_k} \sum_{i: b_i = j} \mathbf{H}_{k,j} \mathbf{G}_i \mathbf{x}_i}_{\text{intercell interf.}} + \mathbf{v}_k$$

where \mathbf{x}_k is the intended (white, identity covariance) signal, \mathbf{H}_{k,b_k} is the $N_k \times M_{b_k}$ channel from BS b_k to user k . BS b_k serves $K_{b_k} = \sum_{i: b_i = b_k} 1$ users. We consider a noise whitened signal representation so that we get for the noise $\mathbf{v}_k \sim \mathcal{CN}(0, I_{N_k})$. The $M_{b_k} \times d_k$ spatial Tx filter or precoder is \mathbf{G}_k .

The scenario of interest is that of partial CSIT available globally with all the BSs. The Gaussian CSIT model for the partial CSIT is

$$(5.2) \quad \mathbf{H}_{k,b_k} = \bar{\mathbf{H}}_{k,b_k} + \tilde{\mathbf{H}}_{k,b_k} \mathbf{C}_t^{1/2}$$

where $\bar{\mathbf{H}}_{k,b_k} = \mathbf{E}\mathbf{H}_{k,b_k}$, and $\mathbf{C}_t^{1/2}$ is the Hermitian square-roots of the Tx side covariance matrices. The elements of $\tilde{\mathbf{H}}_{k,b_k}$ are i.i.d. $\sim \mathcal{CN}(0,1)$.

$$(5.3) \quad \begin{aligned} \mathbf{E}_{\mathbf{H}_{k,b_k} | \bar{\mathbf{H}}_{k,b_k}} \left(\mathbf{H}_{k,b_k} - \bar{\mathbf{H}}_{k,b_k} \right) \left(\mathbf{H}_{k,b_k} - \bar{\mathbf{H}}_{k,b_k} \right)^H &= \text{tr}\{\mathbf{C}_t\} \mathbf{I}_{N_k} \\ \mathbf{E}_{\mathbf{H}_{k,b_k} | \bar{\mathbf{H}}_{k,b_k}} \left(\mathbf{H}_{k,b_k} - \bar{\mathbf{H}}_{k,b_k} \right)^H \left(\mathbf{H}_{k,b_k} - \bar{\mathbf{H}}_{k,b_k} \right) &= N_k \mathbf{C}_t \end{aligned}$$

Note that the expectation is done over \mathbf{H}_{k,b_k} , for a known $\bar{\mathbf{H}}_{k,b_k}$. This is true for all the expectation operations done in this paper. However, as the parameter over which the expectation is done is clear from the context, henceforth, we just mention the expectation operator \mathbf{E} to reduce notational overhead.

5.2 EWSR

Once the CSIT is imperfect, various optimization criteria could be considered, such as outage capacity. Here we shall consider the EWSR for a known channel mean $\bar{\mathbf{H}}$.

$$(5.4) \quad \begin{aligned} \text{EWSR}(\mathbf{G}) &= \mathbf{E} \sum_k u_k \ln \left| \mathbf{I} + \mathbf{G}_k^H \mathbf{H}_{k,b_k}^H \mathbf{R}_k^{-1} \mathbf{H}_{k,b_k} \mathbf{G}_k \right| \\ &= \mathbf{E} \sum_{k=1}^K u_k \left(\ln |\mathbf{R}_k| - \ln |\mathbf{R}_k^-| \right). \end{aligned}$$

Here, \mathbf{G} represents the collection of precoders \mathbf{G}_k , u_k are rate weights.

$$(5.5) \quad \begin{aligned} \mathbf{R}_k &= \mathbf{H}_{k,b_k} \mathbf{Q}_k \mathbf{H}_{k,b_k}^H + \mathbf{R}_k^-, \quad \mathbf{Q}_i = \mathbf{G}_i \mathbf{G}_i^H, \\ \mathbf{R}_k^- &= \sum_{i \neq k} \mathbf{H}_{k,b_i} \mathbf{Q}_i \mathbf{H}_{k,b_i}^H + \mathbf{I}_{N_k}. \end{aligned}$$

The EWSR cost function needs to be augmented with the power constraints $\sum_{k:b_k=j} \text{tr}\{\mathbf{Q}_k\} \leq P_j$.

5.3 MaMIMO limit and ESEI-WSR

If the number of Tx antennas M becomes very large, we get a convergence for any quadratic term of the form

$$(5.6) \quad \mathbf{H}\mathbf{Q}\mathbf{H}^H \xrightarrow{N_t \rightarrow \infty} \mathbf{E}\mathbf{H}\mathbf{Q}\mathbf{H}^H = \bar{\mathbf{H}}\mathbf{Q}\bar{\mathbf{H}}^H + \text{tr}\{\mathbf{Q}\mathbf{C}_t\} \mathbf{I}$$

and hence we get the following MaMIMO limit matrices

$$(5.7) \quad \begin{aligned} \check{\mathbf{R}}_k &= \check{\mathbf{R}}_{\bar{k}} + \bar{\mathbf{H}}_{k,b_k} \mathbf{Q}_k \bar{\mathbf{H}}_{k,b_k}^H + \text{tr} \{ \mathbf{Q}_k \mathbf{C}_{t,k,b_k} \} \mathbf{I}_{N_k} \\ \check{\mathbf{R}}_{\bar{k}} &= \mathbf{I}_{N_k} + \sum_{i \neq k}^K \left(\bar{\mathbf{H}}_{k,b_i} \mathbf{Q}_i \bar{\mathbf{H}}_{k,b_i}^H + \text{tr} \{ \mathbf{Q}_i \mathbf{C}_{t,k,b_i} \} \mathbf{I}_{N_k} \right) \end{aligned}$$

With the expectation operator taken care of, the problem is similar to that encountered in chapter 3 for a full CSIT case. Hence, the same approach may be used to maximize the EWSR.

$$(5.8) \quad \begin{aligned} \text{ESEI-WSR} &= \sum_{k=1}^K u_k (\ln |\mathbf{E} \mathbf{R}_k| - \ln |\mathbf{E} \mathbf{R}_{\bar{k}}|) \\ &= \sum_{k=1}^K u_k (\ln |\check{\mathbf{R}}_k| - \ln |\check{\mathbf{R}}_{\bar{k}}|). \end{aligned}$$

We shall refer to this approach as the ESEI-WSR approach as (channel dependent) signal and interference covariance matrices are replaced by their expected values. In the following sections, we analyze the gap between the EWSR and the ESEI-WSR to suggest an approximation of the first by the latter in the design of the precoder.

5.4 EWSR to ESEI-WSR gap Analysis

We are interested in bounding the difference between ESEI-WSR and the EWSR. At the level of each user k , we stack the channel estimates relevant for each user k .

$$(5.9) \quad \begin{aligned} \mathbf{H}_k &= [\mathbf{H}_{k,b_1} \cdots \mathbf{H}_{k,b_{k-1}} \mathbf{H}_{k,b_k} \mathbf{H}_{k,b_{k+1}} \cdots \mathbf{H}_{k,b_K}] \\ &= \bar{\mathbf{H}}_k + \tilde{\mathbf{H}}_k \mathbf{C}_{t,k}^{\frac{1}{2}} \end{aligned}$$

where the elements of $\tilde{\mathbf{H}}_k$ are i.i.d $\sim \mathcal{C} \mathcal{N}(0, 1)$ and $\bar{\mathbf{H}}_k$ refers to the mean part of \mathbf{H}_k . $\mathbf{C}_{t,k}$ is a block diagonal matrix whose i^{th} diagonal block is \mathbf{C}_{t,k,b_i} . Let \mathbf{Q} be a block diagonal matrix with i^{th} diagonal block being $\sum_{l: b_l = b_i} \mathbf{Q}_l$. Note that this summation corresponds to contributions from all the intracell precoding vectors. $\mathbf{Q}_{\bar{k}}$ is similar to \mathbf{Q} but with the k^{th} block diagonal set to $\sum_{l: b_l = b_k}^{l \neq k} \mathbf{Q}_l$. Thus, in $\mathbf{Q}_{\bar{k}}$, only the interfering precoders (intracell and intercell) are included. Then,

$$(5.10) \quad \mathbf{R}_k = \mathbf{I} + \mathbf{H}_k \mathbf{Q} \mathbf{H}_k^H, \quad \mathbf{R}_{\bar{k}} = \mathbf{I} + \mathbf{H}_k \mathbf{Q}_{\bar{k}} \mathbf{H}_k^H$$

$$(5.11) \quad \begin{aligned} \text{EWSR}(\mathbf{G}) &= \sum_{k=1}^K u_k \mathbf{E} \mathbf{H}_k (\ln |\mathbf{R}_k| - \ln |\mathbf{R}_{\bar{k}}|) \\ &= \mathbf{E} \sum_{k=1}^K u_k \left(\ln |\mathbf{I} + \mathbf{H}_k \mathbf{Q} \mathbf{H}_k^H| - \ln |\mathbf{I} + \mathbf{H}_k \mathbf{Q}_{\bar{k}} \mathbf{H}_k^H| \right) \end{aligned}$$

$$(5.12) \quad \text{ESEI-WSR}(\mathbf{G}) = \sum_{k=1}^K u_k \left(\ln |\mathbf{I} + \mathbf{E} \mathbf{H}_k \mathbf{Q} \mathbf{H}_k^H| - \ln |\mathbf{I} + \mathbf{E} \mathbf{H}_k \mathbf{Q}_{\bar{k}} \mathbf{H}_k^H| \right)$$

Thus, the EWSR and ESEI-WSR have been rewritten in a convenient format so that one can focus on the gap between the two by comparing terms of the form $\mathbf{E} \ln |\mathbf{I} + \mathbf{H}_k \mathbf{Q} \mathbf{H}_k^H|$ and $\ln |\mathbf{I} + \mathbf{E} \mathbf{H}_k \mathbf{Q} \mathbf{H}_k^H|$.

5.4.1 Monotonicity of gap with SNR

For an SNR ρ , define

$$(5.13) \quad \Gamma_k(\rho) = \ln \left| \mathbf{I} + \rho \mathbf{E} \mathbf{H}'_k \mathbf{H}'_k{}^H \right| - \mathbf{E} \ln \left| \mathbf{I} + \rho \mathbf{H}'_k \mathbf{H}'_k{}^H \right|$$

where $\mathbf{H}'_k \sim \mathcal{CN}(\bar{\mathbf{H}}'_k, \mathbf{C})$, $\bar{\mathbf{H}}'_k = \frac{1}{\sqrt{\rho}} \bar{\mathbf{H}}_k \mathbf{Q}^{\frac{1}{2}}$, and $\mathbf{C} = \frac{1}{\rho} \mathbf{C}_t^{\frac{1}{2}} \mathbf{Q} \mathbf{C}_t^{\frac{1}{2}}$. Then, $\mathbf{I} + \mathbf{H}_k \mathbf{Q} \mathbf{H}_k{}^H = \mathbf{I} + \rho \mathbf{E} \mathbf{H}'_k \mathbf{H}'_k{}^H$.

Theorem 1. $\Gamma_k(\rho)$ is monotonically increasing in ρ

Proof. $\ln |\mathbf{I} + \rho \mathbf{E} \mathbf{H} \mathbf{H}^H|$ is concave in ρ . By Jensen's inequality, $\Gamma_k(\rho) \geq 0$ and it can be seen easily that equality is attained when $\rho = 0$. To show the monotonicity, we show that the derivative with respect to ρ is always non-negative. We omit the subscripts and superscripts on \mathbf{H} for convenience.

$$(5.14) \quad \begin{aligned} \frac{\partial}{\partial \rho} \left(\ln |\mathbf{I} + \rho \mathbf{E} \mathbf{H} \mathbf{H}^H| - \mathbf{E} \ln |\mathbf{I} + \rho \mathbf{H} \mathbf{H}^H| \right) = \\ \text{tr} \left(\left\{ \mathbf{I} + \rho \mathbf{E} \mathbf{H} \mathbf{H}^H \right\}^{-1} \mathbf{E} \mathbf{H} \mathbf{H}^H - \mathbf{E} \left(\left\{ \mathbf{I} + \rho \mathbf{H} \mathbf{H}^H \right\}^{-1} \mathbf{H} \mathbf{H}^H \right) \right) \end{aligned}$$

Noting that, $\left\{ \mathbf{I} + \rho \mathbf{E} \mathbf{H} \mathbf{H}^H \right\}^{-1} \mathbf{E} \mathbf{H} \mathbf{H}^H$ can be written as $\frac{1}{\rho} \mathbf{I} - \frac{1}{\rho} \left\{ \mathbf{I} + \rho \mathbf{E} \mathbf{H} \mathbf{H}^H \right\}^{-1}$,

$$(5.15) \quad \frac{\partial}{\partial \rho} \left(\ln |\mathbf{I} + \rho \mathbf{E} \mathbf{H} \mathbf{H}^H| - \mathbf{E} \ln |\mathbf{I} + \rho \mathbf{H} \mathbf{H}^H| \right) = \frac{1}{\rho} \text{tr} \left\{ \mathbf{E} \left(\left\{ \mathbf{I} + \rho \mathbf{H} \mathbf{H}^H \right\}^{-1} \right) \right\} - \text{tr} \left\{ \frac{1}{\rho} \left\{ \mathbf{I} + \rho \mathbf{E} \mathbf{H} \mathbf{H}^H \right\}^{-1} \right\} \geq 0$$

where we have applied Jensen's inequality again as $\left\{ \mathbf{I} + \rho \mathbf{H} \mathbf{H}^H \right\}^{-1}$ is a convex function in ρ . ■

As a result, the largest value of $\Gamma_k(\rho)$ will be observed at infinite SNR for a general non-zero mean MIMO channel \mathbf{H} with arbitrary transmit covariance matrix. Now, following the same steps as in [36], we can obtain, for any collection of precoders \mathbf{G} ,

$$(5.16) \quad \begin{aligned} \text{ESEI-WSR} - \sum_{k=1}^K u_k \Gamma_k(\infty) &\leq \text{ESEI-WSR} - \sum_{k=1}^K u_k \Gamma_k(\rho) \\ &\leq \text{EWSR} \leq \\ \text{ESEI-WSR} + \sum_{k=1}^K u_k \Gamma_{\bar{k}}(\rho) &\leq \text{ESEI-WSR} + \sum_{k=1}^K u_k \Gamma_{\bar{k}}(\infty) \end{aligned}$$

In the above, $\Gamma_k(\rho)$ and $\Gamma_{\bar{k}}(\rho)$ are terms corresponding to the first and the second terms of equation (5.11). Remains now to obtain the $\Gamma_k(\infty)$ for different scenarios. Hence, in the rest of this chapter, we will drop the subscript k and use the notation $\Gamma(\rho)$. However, we first look at the Taylor series expansion of EWSR to get an alternative expression for the gap.

5.4.2 Second-Order Taylor Series Expansion of EWSR

Consider the Taylor series expansion for matrices \mathbf{X} , \mathbf{Y} of dimension N_k .

$$(5.17) \quad \ln|\mathbf{X} + \mathbf{Y}| \approx \ln|\mathbf{X}| + \text{tr}\{\mathbf{X}^{-1}\mathbf{Y}\} - \frac{1}{2}\text{tr}\{\mathbf{X}^{-1}\mathbf{Y}\mathbf{X}^{-1}\mathbf{Y}\}$$

Consider $\mathbf{X} + \mathbf{Y} = \mathbf{I} + \rho\mathbf{H}\mathbf{H}^H$, $\mathbf{H} = \bar{\mathbf{H}} + \tilde{\mathbf{H}}\mathbf{C}^{\frac{1}{2}}$, $\tilde{\mathbf{H}} \sim \mathcal{CN}(0, \mathbf{I})$. For expansion around $\mathbf{I} + \rho\mathbf{E}\mathbf{H}\mathbf{H}^H$, choose $\mathbf{X} = \mathbf{I} + \rho\mathbf{E}\mathbf{H}\mathbf{H}^H$, $\mathbf{Y} = \rho(\mathbf{E}\mathbf{H}\mathbf{H}^H - \mathbf{H}\mathbf{H}^H)$. Hence, we get,

$$(5.18) \quad \mathbf{E} \ln|\mathbf{I} + \rho\mathbf{H}\mathbf{H}^H| \approx \ln|\mathbf{I} + \rho\mathbf{E}\mathbf{H}\mathbf{H}^H| - \frac{\rho^2}{2}\mathbf{E} \text{tr}\left\{\mathbf{X}^{-1}(\mathbf{H}\mathbf{H}^H - \mathbf{E}\mathbf{H}\mathbf{H}^H)\mathbf{X}^{-1}(\mathbf{H}\mathbf{H}^H - \mathbf{E}\mathbf{H}\mathbf{H}^H)\right\}$$

Using 4th order Gaussian moments [19], we get

$$(5.19) \quad \mathbf{E} \ln|\mathbf{I} + \rho\mathbf{H}\mathbf{H}^H| \approx \ln|\mathbf{I} + \rho\mathbf{E}\mathbf{H}\mathbf{H}^H| - \frac{\rho^2}{2}\text{tr}\left\{\text{tr}\{\mathbf{X}^{-1}\}^2\mathbf{C}^2 + 2\text{tr}\{\mathbf{X}^{-1}\}\bar{\mathbf{H}}^H\mathbf{X}^{-1}\bar{\mathbf{H}}\mathbf{C} - (\bar{\mathbf{H}}^H\mathbf{X}^{-1}\bar{\mathbf{H}})^2\right\}.$$

Let us denote this second-order approximation by $\check{\Gamma}(\rho)$. i.e,

$$(5.20) \quad \check{\Gamma}(\rho) = \frac{\rho^2}{2}\text{tr}\left\{\text{tr}\{\mathbf{X}^{-1}\}^2\mathbf{C}^2 + 2\text{tr}\{\mathbf{X}^{-1}\}\bar{\mathbf{H}}^H\mathbf{X}^{-1}\bar{\mathbf{H}}\mathbf{C} - (\bar{\mathbf{H}}^H\mathbf{X}^{-1}\bar{\mathbf{H}})^2\right\}.$$

Consider the mean zero special case, $\bar{\mathbf{H}} = 0$. Then, $\mathbf{E}\mathbf{H}\mathbf{H}^H = \text{tr}\{\mathbf{C}\}\mathbf{I}$ and $\mathbf{X} = \mathbf{I}_{N_k} + \rho\text{tr}\{\mathbf{C}\}\mathbf{I}_{N_k}$. Therefore,

$$(5.21) \quad \mathbf{E} \ln|\mathbf{I} + \rho\mathbf{H}\mathbf{H}^H| \approx \ln(1 + \rho\text{tr}\{\mathbf{C}\}) - \frac{\rho^2 N_k^2}{2} \frac{\text{tr}\{\mathbf{C}^2\}}{(1 + \rho\text{tr}\{\mathbf{C}\})^2}.$$

At high SNR, as $\rho \rightarrow \infty$,

$$(5.22) \quad \mathbf{E} \ln|\mathbf{I} + \rho\mathbf{H}\mathbf{H}^H| \approx \ln(1 + \rho\text{tr}\{\mathbf{C}\}) - \frac{N_k^2}{2} \frac{\text{tr}\{\mathbf{C}^2\}}{(\text{tr}\{\mathbf{C}\})^2}.$$

Thus, $\check{\Gamma}(\infty) = \frac{N_k^2}{2} \frac{\text{tr}\{\mathbf{C}^2\}}{(\text{tr}\{\mathbf{C}\})^2}$. Continuing from Theorem 1, we now determine the value of $\Gamma(\infty)$ for different scenarios.

5.4.3 MISO correlated channel

In the MISO correlated channel, the relevant metric is of the form $\ln(1 + \|\mathbf{h}\|^2)$, where \mathbf{h} is a $1 \times M$ MISO channel vector with $\lambda_1 \cdots \lambda_p$ being the p non-zero, non-identical eigenvalues of the correlation matrix $\mathbf{E}\mathbf{h}\mathbf{h}^H$.

Though in general, the correlation matrix would have non-equal eigenvalues, it is illustrative to consider an extreme case where the eigenvalues are all identical and $p = M$. In fact, this is identical to a MISO i.i.d channel.

Theorem 2.

$$0 \leq \ln(1 + \rho M) - \mathbf{E} \ln(1 + \rho\|\mathbf{h}\|^2) \leq \gamma - \left(\sum_{k=1}^M \frac{1}{k} - \ln(M) \right) + \frac{1}{M}$$

Proof. To ease the notation, we take $x = \|\mathbf{h}\|^2$, where x is Chi-squared distributed with mean M .

$$(5.23) \quad f_X(x) = \frac{x^{M-1}e^{-x}}{(M-1)!}.$$

It is known that,

$$(5.24) \quad \gamma = - \int_0^\infty e^{-x} \ln(x) dx.$$

At high SNR ($\rho \rightarrow \infty$),

$$(5.25) \quad \mathbf{E}_x \ln(1 + \rho x) = \int_0^\infty f_X(x) \ln(\rho x) dx = \int_0^\infty \frac{x^{M-1}e^{-x}}{(M-1)!} \ln(x) dx + \ln(\rho).$$

We note the following,

$$(5.26) \quad \begin{aligned} \int e^{-x} \ln(x) dx &= -e^{-x} \ln(x) + \text{Ei}(-x). \\ \text{Ei}(x) &= - \int_{-x}^\infty \frac{e^{-t}}{t} dt. \\ - \int_0^\infty \frac{x^{(M-2)}}{(M-2)!} \text{Ei}(-x) dx &= \int_0^\infty \frac{x^{(M-2)}}{(M-2)!} \int_x^\infty \frac{e^{-t}}{t} dt dx = \int_0^\infty \left(\int_0^t \frac{x^{(M-2)}}{(M-2)!} dx \right) \frac{e^{-t}}{t} dt \\ &= \int_0^\infty \frac{t^{(M-1)}}{(M-1)!} \frac{e^{-t}}{t} dt = \frac{1}{M-1}. \end{aligned}$$

Integrating by parts ($M \geq 2$),

$$(5.27) \quad \int_0^\infty \frac{x^{M-1}e^{-x}}{(M-1)!} \ln(x) dx = \frac{x^{M-1}}{(M-1)!} (-e^{-x} \ln(x) + \text{Ei}(-x)) \Big|_0^\infty - \int_0^\infty \frac{x^{M-2}}{(M-2)!} (-e^{-x} \ln(x) + \text{Ei}(-x))$$

The first part in the above equation is zero, so we only need to focus on the second portion of the integral.

$$(5.28) \quad \begin{aligned} \int_0^\infty \frac{x^{M-1}e^{-x}}{(M-1)!} \ln(x) dx &= - \int_0^\infty \frac{x^{M-2}}{(M-2)!} (-e^{-x} \ln(x) + \text{Ei}(-x)) \\ &= \int_0^\infty \frac{x^{M-2}e^{-x}}{(M-2)!} \ln(x) dx - \int_0^\infty \frac{x^{M-2}}{(M-2)!} \text{Ei}(-x) \\ &= \int_0^\infty \frac{x^{M-2}e^{-x}}{(M-2)!} \ln(x) dx + \frac{1}{M-1} \end{aligned}$$

The above is a recursive equation, from where we quickly deduce that,

$$(5.29) \quad \int_0^\infty \frac{x^{M-1}e^{-x}}{(M-1)!} \ln(x) dx = \int_0^\infty e^{-x} \ln(x) dx + \sum_{k=1}^{M-1} \frac{1}{k} = -\gamma + \sum_{k=1}^{M-1} \frac{1}{k}$$

Thus, we can now write (5.25) as,

$$(5.30) \quad \begin{aligned} \mathbf{E}_x \ln(1 + \rho x) &= \int_0^\infty \frac{x^{M-1}e^{-x}}{(M-1)!} \ln(x) dx + \ln(\rho) \\ &= -\gamma + \sum_{k=1}^{M-1} \frac{1}{k} + \ln(\rho) \\ &= -\gamma + \left(\sum_{k=1}^{M-1} \frac{1}{k} - \ln(M) \right) + \ln(M\rho) \end{aligned}$$

■

Note that for $M = 1$, the bound reduces to that in [36], namely γ . Thus, this bound is a much more refined and tighter bound than what is provided in [36]. We further explore the bound using the properties of the harmonic series. Define $\mathcal{H}_p = \sum_{k=1}^p \frac{1}{k}$. It is known that,

$$(5.31) \quad \mathcal{H}_p = \ln(p) + \gamma + \frac{1}{2p} - \frac{1}{12p^2} + \frac{1}{120p^4} \cdots$$

Using this in (2), we get

$$(5.32) \quad \gamma - (\mathcal{H}_p - \ln(p)) + \frac{1}{p} = \frac{1}{2p} + \frac{1}{12p^2} - \frac{1}{120p^4} \cdots$$

Thus, the second-order term for the bound is $\frac{1}{2p}$, which is also in agreement with equation (5.22),

$$(5.33) \quad \frac{1 \operatorname{tr}\{\mathbf{C}^2\}}{2 (\operatorname{tr}\{\mathbf{C}\})^2} = \frac{\sum_{i=1}^p \lambda_i^2}{2(\sum_{i=1}^p \lambda_i)^2} = \frac{1}{2p}.$$

Theorem 3.

$$(5.34) \quad 0 \leq \ln(1 + \rho \sum_{i=1}^p \lambda_i) - \mathbf{E} \ln(1 + \rho \|\mathbf{h}\|^2) \leq \gamma - \left(\sum_{i=1}^p \frac{\ln \lambda_i}{\pi_{l \neq i}(1 - \lambda_l/\lambda_i)} - \ln \left(\sum_{i=1}^p \lambda_i \right) \right),$$

where ρ is the SNR, γ is Euler constant.

Proof. For a correlated MISO scenario, we can write equivalently,

$\ln|1 + \rho \|\mathbf{h}\|^2| = \ln|1 + \rho \sum_{i=1}^p \lambda_i |\mathbf{h}_i|^2|$, where $\lambda_i, i \in 1 \cdots p$ are the non-zero, non-identical eigenvalues of the correlation matrix $\mathbf{E}\mathbf{h}\mathbf{h}^H$, scaled in such a manner that $\sum_{i=1}^p \lambda_i = M$. $\mathbf{h}_i \sim \mathcal{CN}(0, 1)$. The probability distribution is given in [16] as $\sum_{i=1}^p \frac{e^{-\frac{x}{\lambda_i}}}{\lambda_i \pi_{l \neq i}(1 - \lambda_l/\lambda_i)}$, where $x = \sum_{i=1}^p \lambda_i |\mathbf{h}_i|^2$. Thus, at high SNR ($\rho \rightarrow \infty$),

$$(5.35) \quad \begin{aligned} \mathbf{E}_x \ln(1 + \rho x) &= \int_0^\infty \sum_{i=1}^p \frac{e^{-\frac{x}{\lambda_i}}}{\lambda_i \pi_{l \neq i}(1 - \lambda_l/\lambda_i)} \ln(x) dx + \ln(\rho) \\ &= \sum_{i=1}^p \frac{\int_0^\infty \frac{1}{\lambda_i} e^{-\frac{x}{\lambda_i}} \ln(x) dx}{\pi_{l \neq i}(1 - \lambda_l/\lambda_i)} + \ln(\rho) = \sum_{i=1}^p \frac{-\gamma + \ln \lambda_i}{\pi_{l \neq i}(1 - \lambda_l/\lambda_i)} + \ln(\rho) \\ &= -\gamma + \left(\sum_{i=1}^p \frac{\ln \lambda_i}{\pi_{l \neq i}(1 - \lambda_l/\lambda_i)} - \ln \left(\sum_{i=1}^p \lambda_i \right) \right) + \ln(\rho \sum_{i=1}^p \lambda_i). \end{aligned}$$

■

5.4.4 MIMO zero mean i.i.d channel

In a multi-user scenario, the regime of interest is $M \geq N_k$. To tackle this scenario, we first introduce the LDU (Lower Diagonal Upper triangular factorization) of the channel Gram matrix,

$$(5.36) \quad \mathbf{H}\mathbf{H}^H = \mathbf{L}\mathbf{D}\mathbf{L}^H = (\mathbf{L}\mathbf{D}^{\frac{1}{2}})(\mathbf{L}\mathbf{D}^{\frac{1}{2}})^H$$

where \mathbf{L} has unit diagonal and \mathbf{D} is a diagonal matrix with diagonal entries (\mathbf{D}_i) greater than zero. The second factorization corresponds to a Cholesky decomposition. The Cholesky factorization of a Wishart matrix (such as $\mathbf{H}\mathbf{H}^H$) leads to,

$$\mathbf{D}_i \sim \frac{1}{2} \chi_{2(M-i+1)}^2, i \in 1 \cdots N_k \quad \mathbf{L}_{i,j} \mathbf{D}_i^{\frac{1}{2}} \sim \mathcal{CN}(0, 1), i > j$$

which is also known as Bartlett's decomposition [28]. Note that $|\mathbf{H}\mathbf{H}^H| = |\mathbf{L}\mathbf{D}\mathbf{L}^H| = |\mathbf{D}|$. Hence, $\ln|\mathbf{H}\mathbf{H}^H| = \sum_{i=1}^{N_k} \ln|\mathbf{D}_i|$ and the MIMO case reduces to a sum of MISO scenarios, each having a χ^2 distribution with a reducing number of degrees of freedom. Thus, reusing the results in section 5.4.3, we get,

$$(5.37) \quad \Gamma(\infty) = \sum_{i=1}^{N_k} \left(\gamma - \left(\sum_{k=1}^{M-i} \frac{1}{k} - \ln(M) \right) \right)$$

For illustration, let us also consider $M \gg N_k$. Then using the approximation of the Harmonic series, it can be easily shown that $\Gamma(\infty) \approx \frac{N_k^2}{2M}$, which concurs with the second-order Taylor series term in (5.22). The general case of correlated MIMO channel with non-zero mean is a future work to be addressed. However, we conjecture that in the case of a non-zero mean MIMO, the gap would further reduce based on the rice factor (the ratio of the power in the mean to that of the random part). However, a few comments are in order. Whenever $\Gamma(\infty)$ is closely approximated by $\check{\Gamma}(\infty)$ then $\Gamma(\rho)$ should be closely approximated by $\check{\Gamma}(\rho)$ also. We can also observe that whenever the gap $\Gamma(\rho)$ gets small, the second-order term $\check{\Gamma}(\rho)$ becomes good, in the sense that $\Gamma(\rho) = \check{\Gamma}(\rho) + O(\Gamma_2^2(\rho))$.

5.5 Actual EWSR Gap

In the previous sections, the analysis was based upon determining an optimal collection of precoders denoted as \mathbf{G}^{**} using the ESEI-WSR criterion. Once this is done, we evaluate $|\text{EWSR}(\mathbf{G}^{**}) - \text{ESEI-WSR}(\mathbf{G}^{**})|$ to determine the gap. However, note that our real interest is in bounding the difference $|\text{EWSR}(\mathbf{G}^*) - \text{EWSR}(\mathbf{G}^{**})|$, where \mathbf{G}^* refers to the optimal precoders that maximize the EWSR metric. This actual gap determination is not straightforward because of the difficulty in optimizing the EWSR metric to obtain \mathbf{G}^* . We now provide some insights into this for cases where the Tx has more antennas than the dimension of the total interference covariance subspace. Consider a MISO scenario with covariance only CSIT. At infinite SNR, the optimal precoders perform zero-forcing (ZF). Thus, there is no interference observed at user k and only the signal part needs to be optimized. Then, the equivalent scalar channel observed at the receiver for a zero mean Gaussian channel \mathbf{h}_k may be written as $\mathbf{h}_k \mathbf{g}_k$, which is clearly complex Gaussian for any choice of the precoding vector \mathbf{g}_k . Thus, at infinite SNR, \mathbf{G}^* optimizes $\sum_{k=1}^K \mathbf{E} \ln(|\mathbf{h}_k \mathbf{g}_k|^2)$ and the ESEI-WSR optimizes $\sum_{k=1}^K \ln(\mathbf{E} |\mathbf{h}_k \mathbf{g}_k|^2)$. However, as shown in the proof of Theorem 2, $\ln(\mathbf{E} |\mathbf{h}_k \mathbf{g}_k|^2) = \mathbf{E} \ln(|\mathbf{h}_k \mathbf{g}_k|^2) - \gamma$. I.e, in this case, the two metrics differ only by a constant and it follows immediately that $\mathbf{G}^* = \mathbf{G}^{**}$.

Thus, for a zero mean correlated MISO IBC channel allowing covariance CSIT based ZF, at infinite SNR, the actual gap $|\text{EWSR}(\mathbf{G}^*) - \text{EWSR}(\mathbf{G}^{**})| = 0$.

5.6 Simulation Results

Figure 5.1 verifies the infinite-SNR bounds for MISO correlated scenario by comparing them against the true values of the gap for different SNRs and different values of M . The true values of the gap are obtained from Matlab simulations by averaging across different channel realizations and channel correlations. As expected, the gap is zero at very low SNR. As the SNR increases, the gap monotonically increases to the infinite SNR limit, as predicted in section 5.4.1. In addition, the gap reduces rapidly with increasing M . Further, to verify the goodness of the second-order

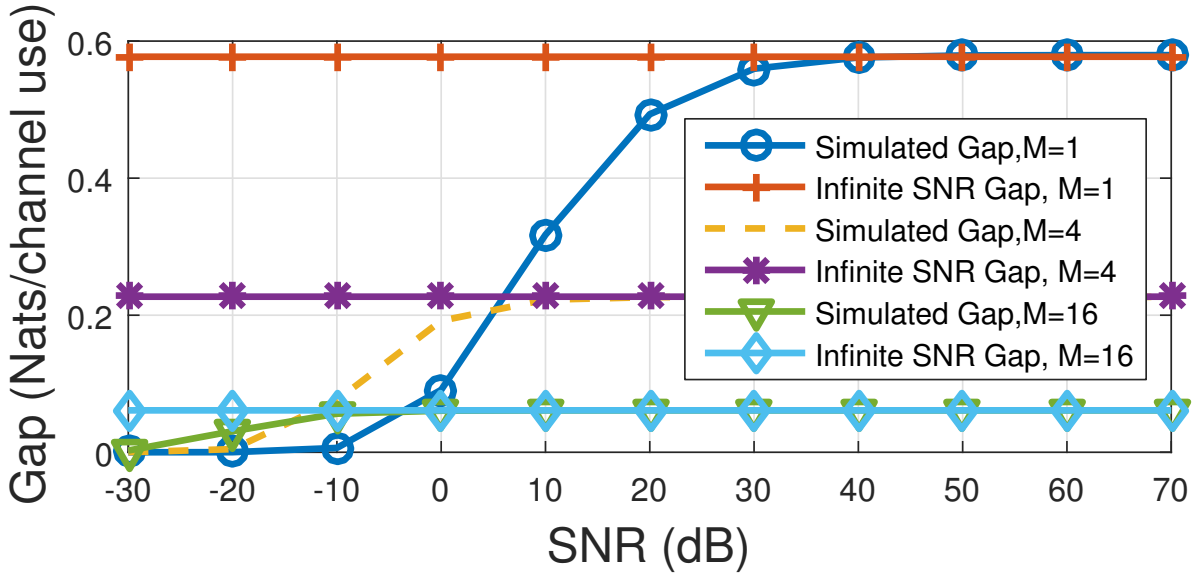


Figure 5.1: Gap between ESEI-WSR and EWSR for the MISO correlated scenario for different values of transmit antennas.

Taylor series approximation, Figure 5.2 compares the true gap to the gap approximated from the Taylor series expansion for a zero mean correlated MIMO scenario. This scenario is chosen as we expect the gap to be maximum here. The number of receive antennas for each user was chosen as $N_k = 4$. ρ was chosen as 1000. As expected, the Taylor series approximation becomes more accurate with increasing number of Tx antennas. Indeed, even in this MIMO correlated scenario, the gap reduces quickly as the number of Tx antennas increases.

5.7 Conclusion

We have motivated the use of the ESEI-WSR metric (or the MaMIMO limit of the EWSR) for utility optimization involving partial CSIT. Towards this end, we presented a refined bound for the gap between EWSR and the ESEI-WSR. We first showed that the gap is maximum at infinite SNR. The results clearly show that the gap reduces with increasing number of transmit antennas, thereby concurring with the well-known result for the MaMIMO limit. We also derived

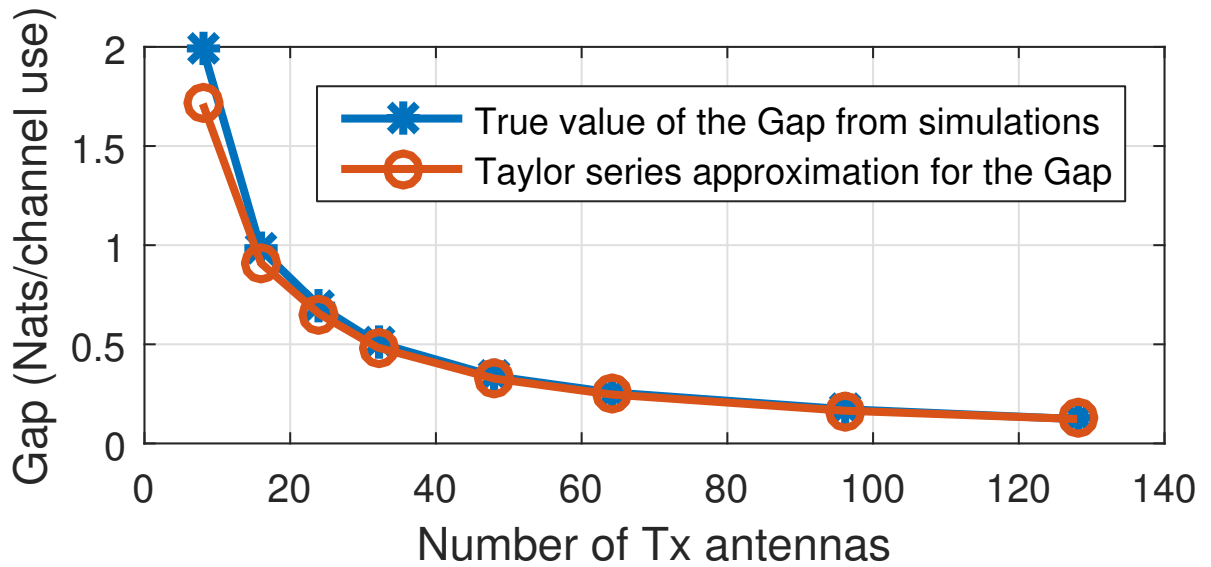


Figure 5.2: Gap obtained from the second-order Taylor series approximation vs. the true value of the gap for a MIMO correlated scenario. The number of antennas at each receiver, N_k , is taken as 4.

an alternative simple approximate expression for the gap using the second-order Taylor series approximation. The general case of correlated MIMO channel with non-zero mean is a subject of future work. However, we conjecture that in the case of a non-zero mean MIMO, the gap would further reduce based on the rice factor (the ratio of the power in the mean to that of the random part).

5.8 Summary of Contributions

- Motivated the use of the ESEI-WSR metric (or the MaMIMO limit of the EWSR) for utility optimization involving partial CSIT.
- Showed that the gap is maximum at infinite SNR and that it reduces with increasing number of transmit antennas.
- Also touched upon the actual gap criterion and showed that for a specific MISO scenario with covariance only CSIT, this gap is zero. I.e, the ESEI-WSR metric optimization results in the true EWSR optimum.
- This work was published in [?].

EXPERIMENTAL RESULTS

In this chapter, we detail some of the experimental evaluations performed in the Eurecom lab as part of demo deliverables to different projects. We detail the following

- Downlink channel estimation via RCMM.
- MU-MIMO precoding for a 2 BS, 2 UE scenario.
- Multiple antenna based self-interference cancellation for Full Duplex scenario.

The first two experiments were performed using the Eurecom MaMIMO testbed. The third demo was developed from scratch using Universal Software Radio Peripheral (USRP) B210 software defined radio (SDR) kit.

6.1 Downlink channel estimation via RCMM.

In this section, we implement the RCMM and verify its performance via maximal ratio transmission (MRT) precoding. The estimation of the reciprocity calibration parameters follows basically the Argos [37] approach, but with a non-coherent flavor.

6.1.1 Massive MIMO testbed

Figure 6.1 shows an image of the MaMIMO prototype that is a part of the Eurecom OpenAir-Interface platform. The Eurecom Massive MIMO array is constructed with several microstrip antenna cards, 12 of which are used in the current validation. Each such microstrip card, in turn, has 4 antennas. The 48 antennas are driven by 12 Express MIMO radio cards, where each radio card has 4 transceiver units. The radio units are synchronized with the help of an octoclock. The



Figure 6.1: Eurecom MaMIMO prototype

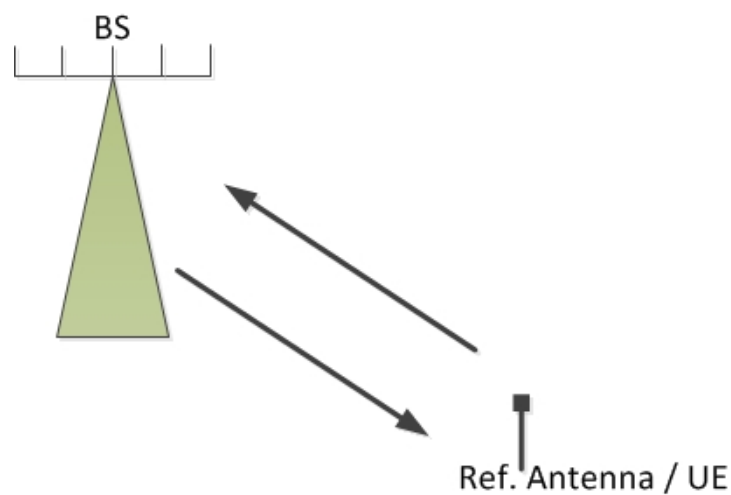


Figure 6.2: Demo configuration for RCMM

parameters of the testbed are listed in Table 6.1. The transmission scheme from the BS as well as the UE uses LTE like frames that contain OFDM symbols. The precoder design is applied individually on every frequency subcarrier.

Figure 6.2 illustrates the demo scenario for the RCMM. The BS units can have up to 46 antennas and the UE has a single antenna. Note that the UE is in reality just another transceiver unit among the overall 48 radios of the hardware setup. The software setup for the demo is as

Parameters	Value
Number of Antennas	48
Center Frequency	2.6GHz
Bandwidth	5 MHz
Sampling Rate	7.68MHz
FFT Size	512
Number of used subcarriers	300
Frame Duration	10ms
Subframe Duration	1ms
OFDM symbols per subframe	12

Table 6.1: Parameters of the Massive MIMO Prototype

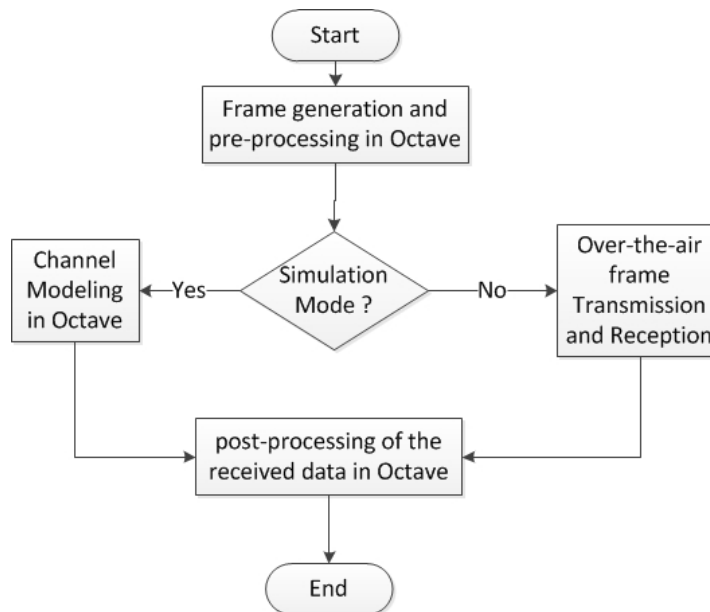


Figure 6.3: Software setup for the experiment.

shown in Fig. 6.3. A key component in the software setup is the possibility to mimic the over-the-air demo in a pure octave environment (an octave simulation only environment) where the over-the-air transmission and reception were replaced by simple channel models in octave. This corresponds to the path followed by the flow chart in Fig. 6.3 when the decision block indicates "yes" for simulation mode. In this scenario, the end to end simulations only involves octave blocks which are easy to debug and control compared to the case where the USRP would be involved. This greatly shortened the development time for the demo as the code could first be validated in simulations before launching the actual over-the-air demo.

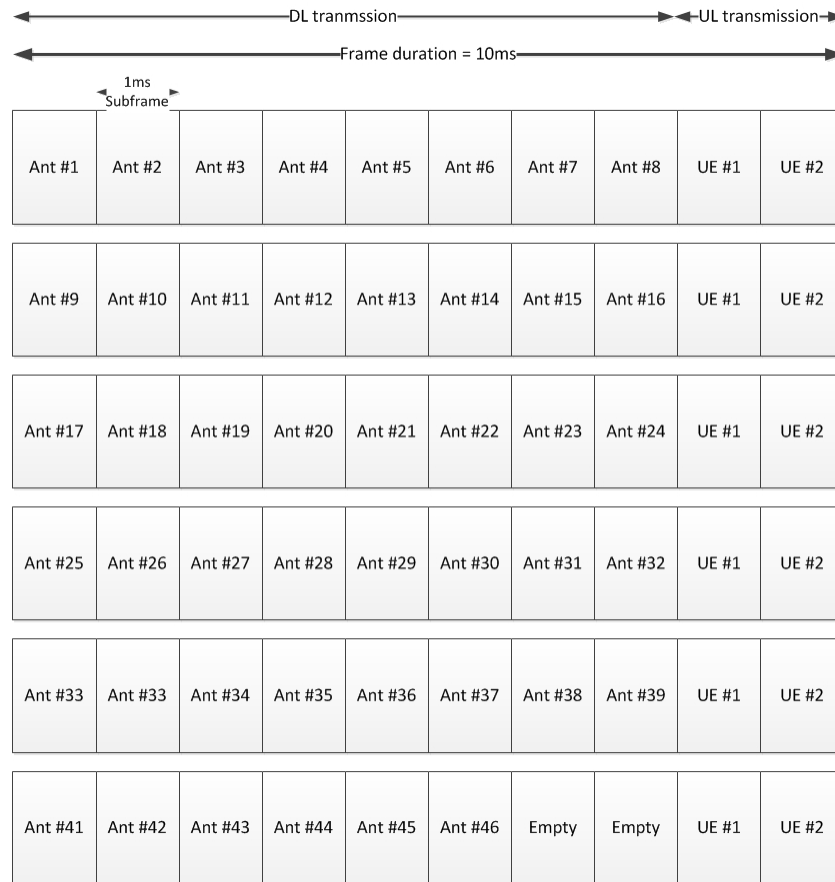


Figure 6.4: Frame structure for calibration parameter estimation.

6.1.2 Frame structure

The frame structure for calibration parameter estimation is shown in Fig. 6.4. Note that this frame structure can support up to 48 Tx antennas and two UEs. The first 8 subframes of the frame are for DL while the last two subframes are for UL. While the BS antennas are in Tx mode, the UE stays in Rx mode and hence receives the signal in the DL. The last two subframes are for UL transmission by the UE where the BS antennas switch to Rx mode. During the DL part of the frame, only one of the Tx antennas transmits non-zero data during any given subframe as indicated by the numbering in Fig. 6.4. This ensures the orthogonality between the different transmissions required to estimate the channel. In the experiment, these frame transmissions are repeated 4 times. During these repetitions, the channel is not assumed to stay a constant, only the reciprocity parameters need to stay a constant. Hence, due to this lack of assumption of channel coherence, our estimation algorithm for reciprocity parameters follows the non-coherent approach.

Note that the use of the calibration frame is just to derive the calibration parameters. Once the calibration parameters are stored, a similar frame can be used to obtain the UL (and the

SF#1 Ideal MRT	SF #2 Naïve MRT	SF #3 Reciprocity based MRT	SF #4 – SF #10
-------------------	--------------------	-----------------------------------	----------------

Figure 6.5: Frame structure for MRT transmission to verify the reciprocity calibration. SF refers to subframe.

actual DL too) channel estimates. As we already have the calibration parameters, the DL channel estimates may be derived from the UL channel estimates. The goodness of this estimate is verified by performing DL MRT precoding. It is important to note that the channel is assumed to remain a constant between the channel estimation phase and the precoding phase. Hence, to reduce the overhead of frame transmission for channel estimation, the channel estimation frame interleaves the transmission from different antennas across subcarriers. With an interleaving factor of 6, one single 10ms frame is sufficient to complete the channel estimation for all the 48 antennas. Of course, the calibration parameters also are assumed to retain their value during this phase. The frame structure for precoding is shown in Fig. 6.5. Only the first 3 subframes are used in this case. No transmission occurs during the rest of the subframes. In the first subframe, the true DL channel estimates are used to derive the MRT precoder. In the next subframe, the UL channel is naively taken as the DL channel to perform precoding. Finally, in the third subframe, the DL channel estimates derived with the help of reciprocity calibration are used to perform precoding.

6.1.3 Results

Consider $L = 4$ repetitions of the pilots using L frame transmissions. During these pilot transmissions, the channel is not expected to remain a constant. Based on the estimated UL and DL channels, we minimize the least squares error $\sum_{l=1}^L |h_i^{(l)} - \mathbf{f}_i \check{h}_i^{(l)}|^2$. Here, h_i^l refers to the DL channel on Tx antenna i obtained during the l^{th} transmission of the calibration frame depicted in Fig. 6.4 for a given subcarrier. "*" refers to the conjugation operation. Explicit subcarrier indices are not shown for ease of notation. Let the corresponding uplink channel across all the antennas be denoted by $\check{\mathbf{h}}$. The least squares estimate of \mathbf{f}_i is now obtained as,

$$(6.1) \quad \mathbf{f}_i = \frac{\sum_{l=1}^L h_i^{(l)} \check{h}_i^{*(l)}}{\sum_{l=1}^L \check{h}_i^{(l)} \check{h}_i^{*(l)}}.$$

Once the calibration factors are estimated, the MRT precoder \mathbf{g}_{MRT} is obtained as follows:

$$(6.2) \quad \mathbf{g}_{MRT} = \mathbf{F}^* \check{\mathbf{h}}^*,$$

where $\mathbf{F} = \text{diag}(\mathbf{f})$. Figure 6.6 shows the need for calibration in a scenario where the BS has 23 antennas. The performance is measured on the basis of the ratio between the received signal power and the noise power (SNR) observed at the UE. Note that the noise power at the UE can be measured easily during the portion of the precoding frame where no DL transmission occurs. The curve "ideal" here refers to the case where the DL channel estimate is available and estimated

directly. The curve "calib" refers to the implementation of (6.2) and the curve "no_calib" directly uses the estimated UL channel for DL precoding without applying any reciprocity calibration. The SNR is shown for all the 300 occupied subcarriers of the 5MHz LTE orthogonal frequency division multiplexing (OFDM) symbol. The close match between the curves "ideal" and "calib" shows the goodness of the calibration. Similarly, the poor performance of the naive calibration ("no_calib") shows the need for calibration. The difference in SNR level between the left half and right half of the figure is due to the noise characteristic on the Express MIMO card.

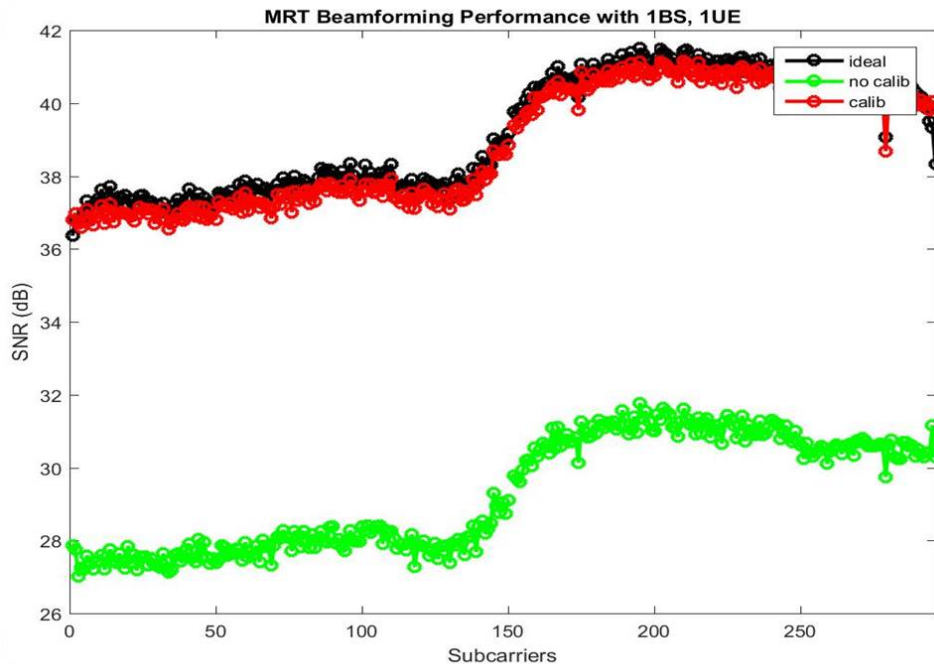


Figure 6.6: Performance of MRT with and without calibration for a 23 antenna BS with a single UE.

6.2 MU-MIMO precoding for a 2 BS, 2 UE scenario

In this section, we consider MU-MIMO precoding for a 2 BS, 2 UE scenario under TDD. We also take into account the fact that the end-to-end digital channel is not reciprocal. The demo framework is the same as that used in Section 6.1. Figure 6.7 illustrates the demo scenario. The two base BS units consist of 23 antennas each and the two UEs have one antenna each. Thus, 48 antennas of the MaMIMO antenna array are used to mimic the BS as well as the two single antenna UEs.

The demo exploits channel reciprocity to derive the DL precoder weights based on the UL channel/covariance estimates. Hence, when the prototype is initialized, we perform a reciprocity calibration and store the reciprocity calibration parameters \mathbf{F} in a file.

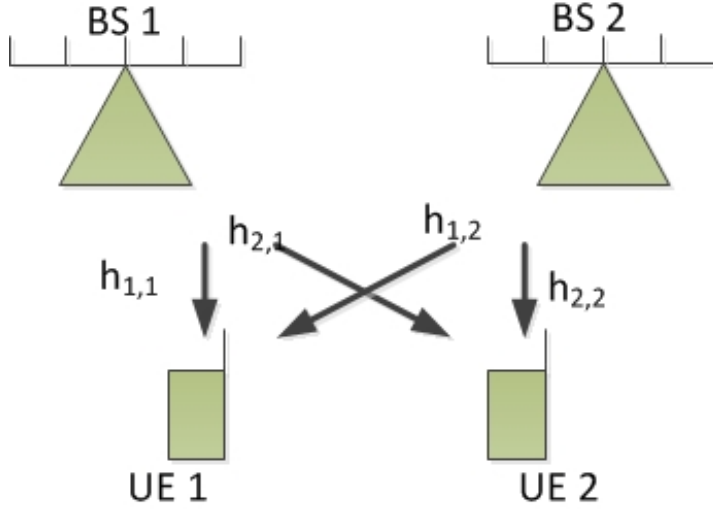


Figure 6.7: Demo configuration for MU-MIMO precoding.

6.2.1 Channel Estimation

To perform precoding using channel reciprocity, the UL channel has to be estimated. It is advantageous to estimate the channel in the UL, as a single pilot transmission from the UE can provide the channel estimate for all the BS antennas. The instantaneous UL channel estimation is based on UL pilots. In our demo, we assume all the useful (non-guard band) subcarriers as pilots in the UL. The quality of the channel estimates is further improved by exploiting the limited time domain spread of the channel taps. An example plot of the time domain channel taps is given in Figure 6.8. To improve the estimation accuracy, we choose only the strongest taps in the time domain, leaving out the taps that are below the noise level.

6.2.2 EWSR Lower Bound: EWSMSE

We have already explored partial CSIT approaches in the previous chapters. Chapter 4 considered a large system approximation and chapter 5 motivated the use of the ESEI-WSR metric. Here, we consider the EWSMSE [29] approach to precoder design under partial CSIT to optimize the EWSR metric defined in equation (4.6). However, we take the special case of a single stream being transmitted to each user as this is the scenario of choice in our demo. Consider the same system model as in (5.1). Due to the assumption of single stream, however, the matrix precoder \mathbf{G}_k is replaced by its vector equivalent \mathbf{g}_k . Introduce an Rx precoder \mathbf{f}_k . The Rx filter output,

$$(6.3) \quad \hat{x}_k = \mathbf{f}_k^H \mathbf{y}_k = \mathbf{f}_k^H \mathbf{H}_{k,b_k} \mathbf{g}_k x_k + \sum_{i \neq k} \mathbf{f}_k^H \mathbf{H}_{k,b_i} \mathbf{g}_i x_i + \mathbf{f}_k^H \mathbf{v}_k$$

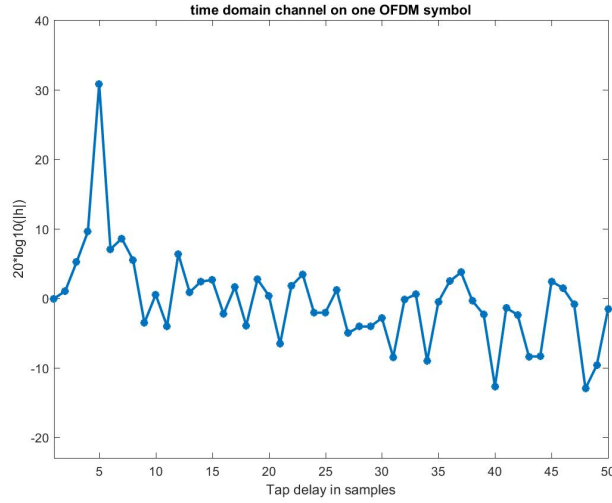


Figure 6.8: Example plot for the channel taps in the time domain.

With this, the mean square error (MSE) may be obtained as,

$$(6.4) \quad e_k(\mathbf{f}_k, \mathbf{g}_k, \mathbf{H}) = 1 - \mathbf{f}_k^H \mathbf{H}_{k,b_k} \mathbf{g}_k - \mathbf{g}_k^H \mathbf{H}_{k,b_k} \mathbf{f}_k + \sum_i \mathbf{f}_k^H \mathbf{H}_{k,b_i} \mathbf{g}_i \mathbf{g}_i^H \mathbf{H}_{k,b_i}^H \mathbf{f}_k + \|\mathbf{f}_k\|^2.$$

Here, \mathbf{H} refers to the collection of all \mathbf{H}_{k,b_i} . It turns out that it is much more attractive to consider $\mathbf{E}e_k(\mathbf{f}_k, \mathbf{g}_k, \mathbf{H})$ as in [29] since $e_k(\mathbf{f}_k, \mathbf{g}_k, \mathbf{H})$ is quadratic in \mathbf{H} . Hence consider optimizing the expected weighted sum MSE, $\mathbf{E}WSMSE(\mathbf{g}, \mathbf{f}, w, \mathbf{H})$.

$$(6.5) \quad \begin{aligned} & \min_{\mathbf{f}, w} \mathbf{E}_{\mathbf{H}|\bar{\mathbf{H}}} WSMSE(\mathbf{g}, \mathbf{f}, w, \mathbf{H}) \\ & \geq \mathbf{E}_{\mathbf{H}|\bar{\mathbf{H}}} \min_{\mathbf{f}, w} WSMSE(\mathbf{g}, \mathbf{f}, w, \mathbf{H}) = -EWSR(\mathbf{g}) \end{aligned}$$

or hence

$$(6.6) \quad EWSR(\mathbf{g}) \geq -\min_{\mathbf{f}, w} \mathbf{E}_{\mathbf{H}|\bar{\mathbf{H}}} WSMSE(\mathbf{g}, \mathbf{f}, w, \mathbf{H}).$$

Thus, this approach results in the maximization of a lower bound of EWSR.

$$\begin{aligned} \mathbf{E}e_k = \hat{e}_k &= 1 - 2\Re\{\mathbf{f}_k^H \bar{\mathbf{H}}_{k,b_k} \mathbf{g}_k\} + \sum_{i=1}^K \mathbf{f}_k^H \bar{\mathbf{H}}_{k,b_i} \mathbf{g}_i \mathbf{g}_i^H \bar{\mathbf{H}}_{k,b_i}^H \mathbf{f}_k \\ &+ \|\mathbf{f}_k\|^2 \sum_{i=1}^K \mathbf{g}_i^H \mathbf{C}_{t,k,b_i} \mathbf{g}_i + \|\mathbf{f}_k\|^2. \end{aligned}$$

where \mathbf{C}_{t,k,b_i} are Tx side (Linear Minimum Mean Square Error (LMMSE) error) covariance matrices of \mathbf{H}_{k,b_i} . Note that the signal term disappears if $\bar{\mathbf{H}}_{k,b_k} = 0$. Hence the EWSMSE lower bound is very loose unless the Rice factor is high, and is useless in the absence of channel estimates. The

overall algorithm for determining the precoders is to perform alternating optimization amongst the following,

$$\begin{aligned}
 (6.7) \quad & \min_{w_k} EWSMSE \Rightarrow w_k = 1/\hat{e}_k \\
 & \min_{\mathbf{f}_k} EWSMSE \Rightarrow \mathbf{f}_k = \hat{\mathbf{R}}_k^{-1} \bar{\mathbf{H}}_{k,b_k} \mathbf{g}_k \\
 & \min_{\mathbf{g}_k} EWSMSE \Rightarrow \mathbf{g}_k = (\hat{\mathbf{T}}_k + \lambda_{b_k} \mathbf{I}_{N_t})^{-1} \bar{\mathbf{H}}_{k,b_k}^H \mathbf{f}_k u_k w_k
 \end{aligned}$$

where

$$\begin{aligned}
 (6.8) \quad & \hat{\mathbf{R}}_k = \sum_i \bar{\mathbf{H}}_{k,b_i} \mathbf{g}_i \mathbf{g}_i^H \bar{\mathbf{H}}_{k,b_i}^H + (1 + \sum_i \mathbf{g}_i^H \mathbf{C}_{t,k,b_i} \mathbf{g}_i) \mathbf{I}_{N_k} \\
 & \hat{\mathbf{T}}_k = \sum_{i=1}^K u_i w_i (\bar{\mathbf{H}}_{i,b_k}^H \mathbf{f}_i \mathbf{f}_i^H \bar{\mathbf{H}}_{i,b_k} + \|\mathbf{f}_i\|^2 \mathbf{C}_{t,k,b_i}).
 \end{aligned}$$

Here, λ_{b_k} corresponds to the Lagrangian multiplier for the transmit power constraint at BS b_k . We remark here that a key interpretation of the EWSMSE equations is that the optimal transmit precoder \mathbf{g}_k has the form of a LMMSE receiver for the dual UL.

6.2.3 Dual DL precoder

We design the partial CSIT precoder based on the EWSMSE approach for a specific case of $N_k = 1$. i.e., when there is only one antenna at the UE. Note that this assumption is not too restrictive as single antenna UE is the typical configuration in Massive MIMO. We shall design the partial CSIT precoder based on a naive UL/DL duality. The relations between Rx \mathbf{f}_k and Tx \mathbf{g}_k in equation (6.7) represent a proper UL/DL duality as one can observe that the optimal DL BF \mathbf{g}_k corresponds to an LMMSE Rx in a dual UL in which the UL channels would be \mathbf{H}_{i,b_k}^H , the UL Tx filters would be \mathbf{f}_i , the UL stream powers would be $u_i w_i$ and the white noise variance at the BS would be λ_{b_k} . These dual UL quantities are obviously different from corresponding actual UL transmission quantities. However, in order to largely simplify BF design and reduce signaling overhead, we propose a naive duality BF design in which we use the actual UL LMMSE Rx as DL BF. Note that one difference between actual and dual UL is a complex conjugation on the channel responses. Also, in the case of $N_k = 1$, we can ignore the UE side BF f_k . Note however that the resulting naive UL/DL duality BF design will converge to a matched filter at low SNR, and to a ZF at high SNR. Hence the naive duality gives optimal results at both low or high SNR. Finally, for the partial CSI aspect, we shall replace statistical (channel) averaging by temporal averaging.

The received signal $\check{\mathbf{y}}_k$ at BS b_k may be written as,

$$(6.9) \quad \check{\mathbf{y}}_k = \check{\mathbf{h}}_{k,b_k} s_k + \check{\mathbf{v}}_{b_k}.$$

Here, $\check{\mathbf{v}}_{b_k}$ includes the AWGN noise as well as the received signal from all other users, both intracell and inter-cell. $\check{\mathbf{h}}_{k,b_k}$ denotes the uplink channel from the user k to BS b_k . Let $\mathbf{R}_{\check{\mathbf{y}}\check{\mathbf{y}}}$ be the uplink correlation matrix. Then the UL Minimum Mean Square Error (MMSE) estimator is given by,

$$(6.10) \quad \mathbf{g}_{MMSE}^{UL} = \check{\mathbf{h}}_{k,b_k}^H \mathbf{R}_{\check{\mathbf{y}}\check{\mathbf{y}}}^{-1}$$

Note that we have used the covariance matrix $\mathbf{R}_{\check{y}\check{y}}$ as the partial CSIT is also local. I.e, each BS only has partial CSIT corresponding to its own UEs and not of UEs corresponding to other BSs. Using reciprocity in TDD and accounting for the calibration factors, the DL MMSE estimator is given by

$$(6.11) \quad \begin{aligned} \mathbf{g}_{MMSE}^{DL} &= \mathbf{R}_{yy,dl}^{-1} \mathbf{h}_{k,b_k}^H = (\mathbf{F}^H \mathbf{R}_{\check{y}\check{y}} \mathbf{F})^{-1} \mathbf{F}^H \check{\mathbf{h}}_{k,b_k}^* \\ &= \mathbf{F}^{-1} \mathbf{R}_{\check{y}\check{y}}^{-1} \check{\mathbf{h}}_{k,b_k}^*. \end{aligned}$$

Here, (*) denotes the conjugation operation. The covariance matrix is derived as a sample covariance as follows.

$$(6.12) \quad \mathbf{R}_{\check{y}\check{y}} = \frac{1}{L} \sum_{i=1}^L \check{\mathbf{y}}_k \check{\mathbf{y}}_k^H$$

A known issue with this approach is the signal cancellation that occurs due to the mismatch between the estimated channel of the desired UE and the implicit component of the desired channel present in the sample covariance matrix [47]. A known solution in this context is the subtraction of the desired signal before computing the covariance matrix. This requires an iterative receiver for joint detection, channel estimation so that the BS can subtract out the contribution from its own UE before computing the covariance matrix.

6.2.4 Results

The instantaneous UL channel estimation is based on UL pilots. Let the UL channel matrix to BS1 be,

$$(6.13) \quad \mathcal{H} = \begin{bmatrix} \check{\mathbf{h}}_{1,1} & \check{\mathbf{h}}_{2,1} \end{bmatrix}$$

In our demo, we assume all the useful subcarriers as pilots in the UL. The quality of the channel estimates are further improved by exploiting the limited time domain spread of the channel taps. Our DL LMMSE design assumes no knowledge of the cross-links between the BS of one cell and UE of another. However, to serve as a reference, we also consider a ZF receiver that has full knowledge of all cross-links. In this case, let the UL channel matrix be,

$$(6.14) \quad \mathcal{H} = \begin{bmatrix} \check{\mathbf{h}}_{1,1} & \check{\mathbf{h}}_{2,1} \end{bmatrix}$$

Then,

$$(6.15) \quad \mathbf{g}_{ZF} = (\mathcal{H}^T \mathbf{F})^H \left(\mathcal{H}^T \mathbf{F} (\mathcal{H}^T \mathbf{F})^H \right)^{-1} \mathbf{e}_1 = \mathbf{F}^H \mathcal{H}^* (\mathcal{H}^T \mathbf{F} \mathbf{F}^H \mathcal{H}^*)^{-1} \mathbf{e}_1,$$

where $\mathbf{e}_1 = [1 \ 0]^T$. The other popular receiver in a MaMIMO scenario is the MRT, which in this case would be,

$$(6.16) \quad \mathbf{g}_{MRT} = \mathbf{F}^* \check{\mathbf{h}}_{1,1}^*.$$

The estimation of the covariance matrix needs significant averaging, particularly as the number of BS antennas increases. In our prototype, we exploit the low delay spread of the environment and compute the average covariance matrix across all the subcarriers.

Figure 6.9 shows the relative gains of MRT and ZF precoders compared to no precoding (omnidirectional antenna) by measuring the signal to interference plus noise ratio (SINR) at UE 1 as a result of using the different precoder techniques. It is remarkable that the performance of the ZF precoder is far superior to that of the MRT which is the most widespread precoding technique used for MaMIMO. In Figure 6.10, the covariance matrix is estimated for the interfering links

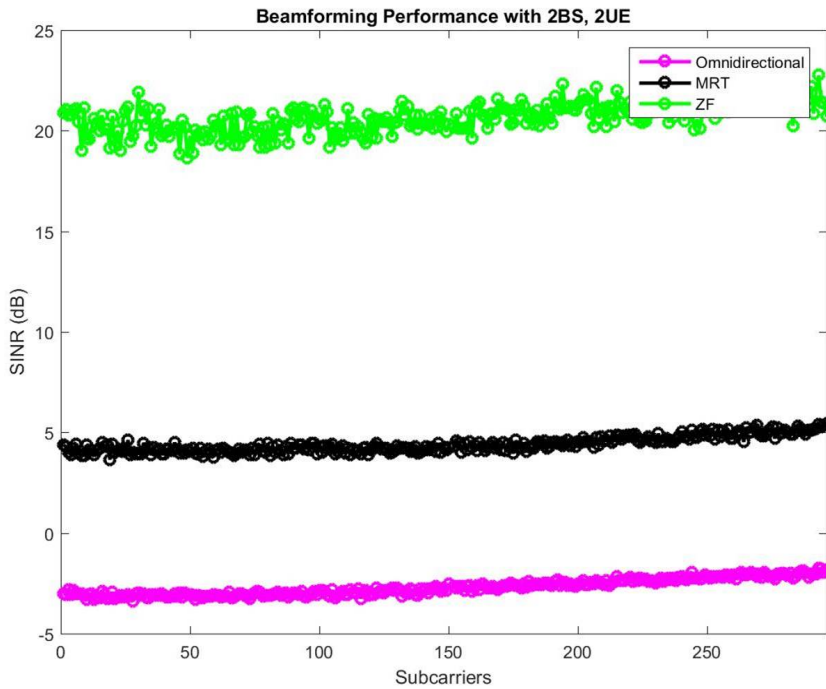


Figure 6.9: Performance of MRT and ZF precoders compared to no precoding

in the UL and the DL MMSE BF is derived based on the UL covariance estimates and the reciprocity calibration parameters. The curve “ZF” serves as a reference where the UL channels of the interfering links are known so that the DL ZF precoding can be done with the help of reciprocity calibration as shown in (6.15). The curve “MMSE_Ryy” is the scenario where the BS computes the covariance based on the total received signal from both its own UE and the interfering UE. We are limited here by the accuracy of the channel estimation and the averaging required for the covariance estimation. For the massive MIMO BS configuration, the averaging requirement for the covariance matrix estimation is very stringent as the dimension of the covariance matrix grows proportionally to the square of the number of BS antennas. Due to inaccuracy in channel estimation, signal cancellation occurs between the channel estimate (in matched filter (MF)) and the channel contribution in $\mathbf{R}_{\check{y}\check{y}}$. The curve “MMSE_Ryy_IntfOnly”

corresponds to the scenario where the covariance of the transmission from the interfering UE is used for DL MMSE BF along with the reciprocity parameters. This approach avoids the signal cancellation issue. Hence, we observe that the performance of “MMSE_Ryy” is much poorer compared to that of the curve “MMSE_Ryy_IntfOnly” for the massive MIMO BS. In fact, the performance of the curve “MMSE_Ryy_IntfOnly” is quite close to that of the ZF which has knowledge of the interfering links as well.

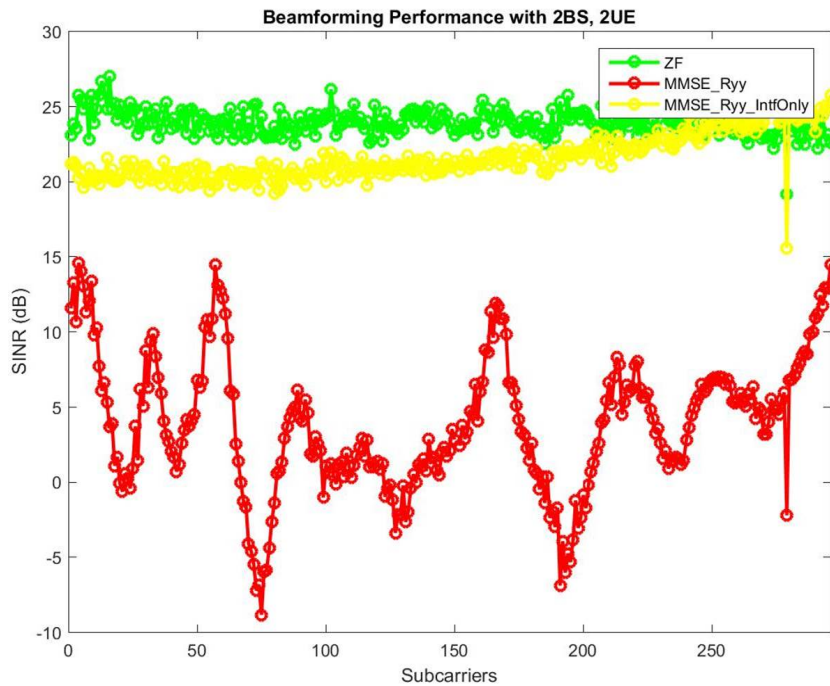


Figure 6.10: Comparison of the performance of partial CSIT LMMSE precoder with that of ZF which requires full information of cross-links.

6.3 Multiple antenna based self-interference cancellation for Full Duplex

Legacy communication systems use either Tx or Rx at a given time using a given frequency. Full Duplex (FD) communication proposes to have simultaneous Tx and Rx at the same frequency and at the same time instant. Of course, this results in severe self-interference at the receiver of the FD system from its own transmitter. For a proper reception, 80-120dB of self-interference cancellation (SIC) is called for. Several works [7],[1] have demonstrated that this can indeed be achieved by a necessary combination of multiple techniques - antenna, RF, analog and digital. A simple instance is to isolate the transmit and receive antennas to increase the attenuation from the Tx to the Rx antenna. With the advent of multiple antennas, another approach is to

precode from the Tx in such a manner as to minimize the self-interference at the Rx antennas. [42], [13] propose a 2x2 Full Duplex MIMO system where the precoding weights are adjusted to selectively cancel the Tx signal at the Rx. [10] experimentally shows the feasibility of this approach for a 72 element antenna array. As concerns the multiple antenna precoding, the lower the number of significant singular values in the channel between the antennas of the Tx and Rx, the lesser the number of Tx antennas required to create nulls at the Rx antennas. Thus, the MIMO self-interference channel that we investigate here is strongly dependent on the antenna arrays involved and can be optimized to reach a desirable rank profile behavior.

This demo was developed jointly with a student intern whom I was supervising. During the development of this work, the Eurecom MaMIMO (Fig. 6.1) was no longer available. Hence, this work was conducted using USRP boards. The purpose of the demo was two-fold:

- Illustrate the multiple antennae based SIC.
- Investigate the rank profile of the internal channel between the BS Tx and Rx antennas.

At the time of writing of the thesis, the demo is functional for two Tx and two Rx antennas, but will be enhanced to use 4Tx and 4 Rx antennas.

6.3.1 USRP based testbed

Fig. 6.11 illustrates the demo configuration. The actual demo setup in the lab is shown in Fig. 6.12. The basic architecture for the software setup was kept identical to that in section 6.1.1 (Fig.

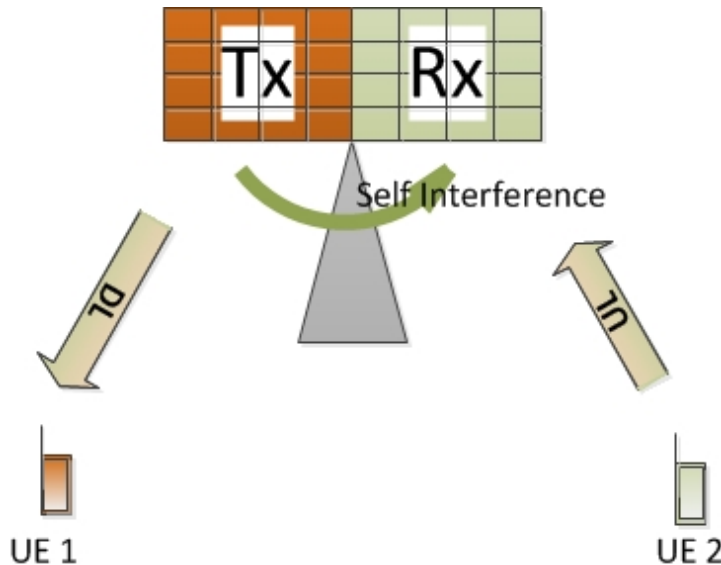


Figure 6.11: FD demo configuration in the lab.

6.3). The key change was to use the USRP boards for the over-the-air transmission instead of the Express MIMO based setup. Of course, the number of antennas under consideration are also far

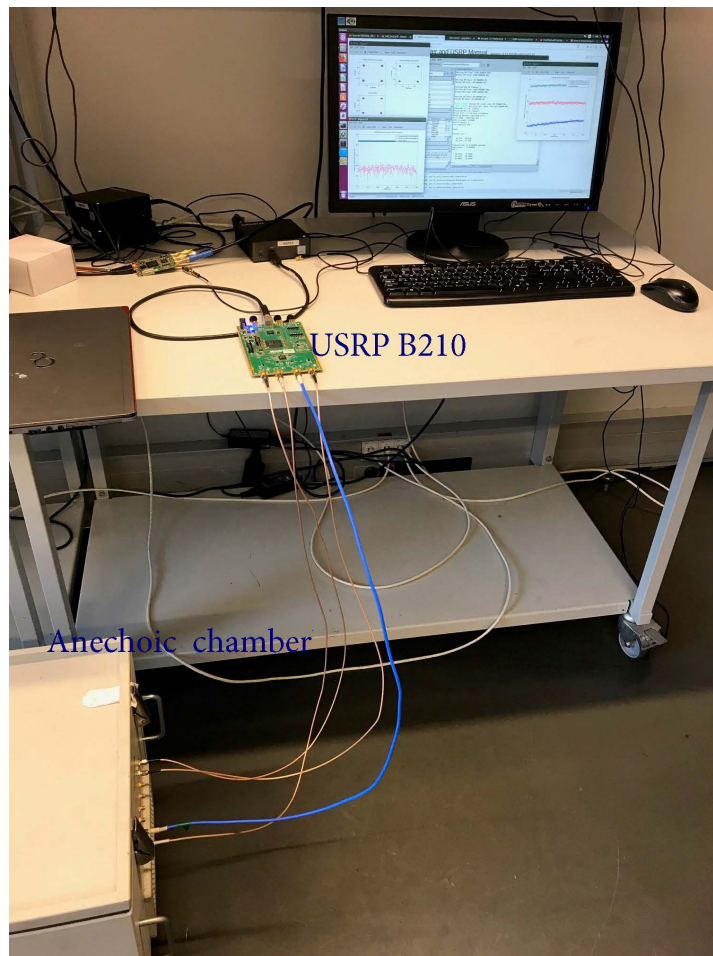


Figure 6.12: FD demo setup in the lab.

less here. Communication with the USRP board from a host processor is via the USRP Hardware Driver (UHD) interface. The UHD installation comes with C++ based examples that illustrate how to perform this communication. One such example was tailored to create an executable that could transmit data from a file and receive data into a file.

6.3.2 Frame structure

The overall demo involves two stages during which the channel is assumed to stay constant:

- A measurement phase where the channels from all the Tx to all the Rx are determined.
- A precoding phase where actual DL precoding is implemented.

The demo parameters are the same as what is listed in Table 6.1. The channel estimation strategy consists of transmitting from one antenna at a time and hence the frame structure is as shown in Fig. 6.13. Note that the frame structure allows transmission from up to 4 Tx antennas

anticipating the enhancement of the demo setup to have 4 Tx antennas. To verify the level of SIC, the channel estimation phase is followed by a precoding phase. Here, we study the signal power received at the UE and the interference level observed at the BS Rx for different precoding strategies as shown in Fig. 6.14.

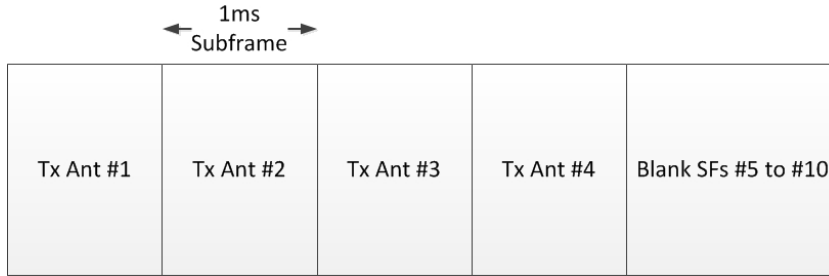


Figure 6.13: Frame structure for channel estimation.

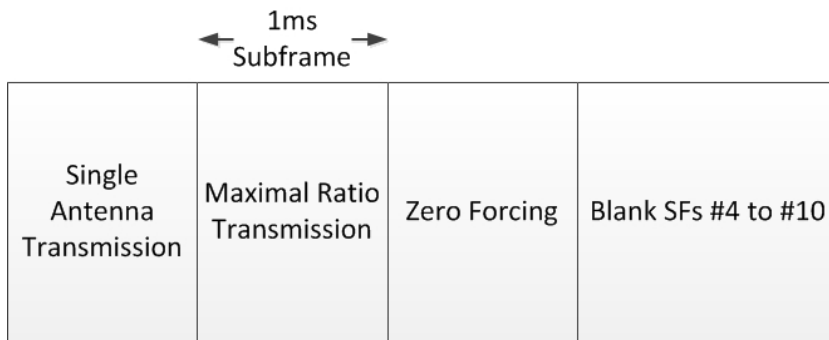


Figure 6.14: Frame structure for precoding.

6.3.3 Results

As the current demo only supports 2Tx and 2 Rx, the selected configuration uses 2 Tx and 1 Rx at the BS while performing precoding for SIC. The remaining Rx is used as the UE. Figure 6.15 shows the signal level and the constellation plot observed at the UE. As expected, the signal level is maximized by the MRT and also results in a slightly better constellation SNR compared to the other approaches. Of course, the constellation SNR for MRT is expected to be poorer once we introduce a second UE in the demo configuration.

The interference level at the BS Rx for the different precoding strategies is shown in Fig 6.16. Here, we see that the ZF approach causes a 20dB reduction in the interference seen at the BS Rx compared to the other approaches.

To investigate the rank profile of the channel between BS Tx and Rx, we use the antenna placement as in Fig. 6.17. Note that in this case, we don't need a UE and hence, both the Rx antennas may be considered to belong to the BS. Thus, we get an internal channel of dimension

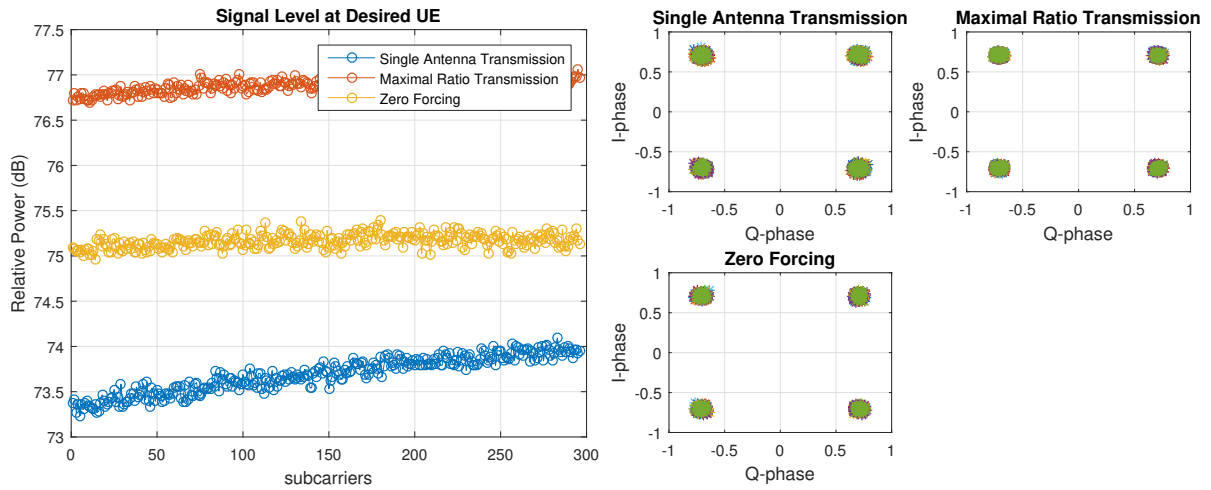


Figure 6.15: Signal level and constellation plot at UE for the different precoding approaches.

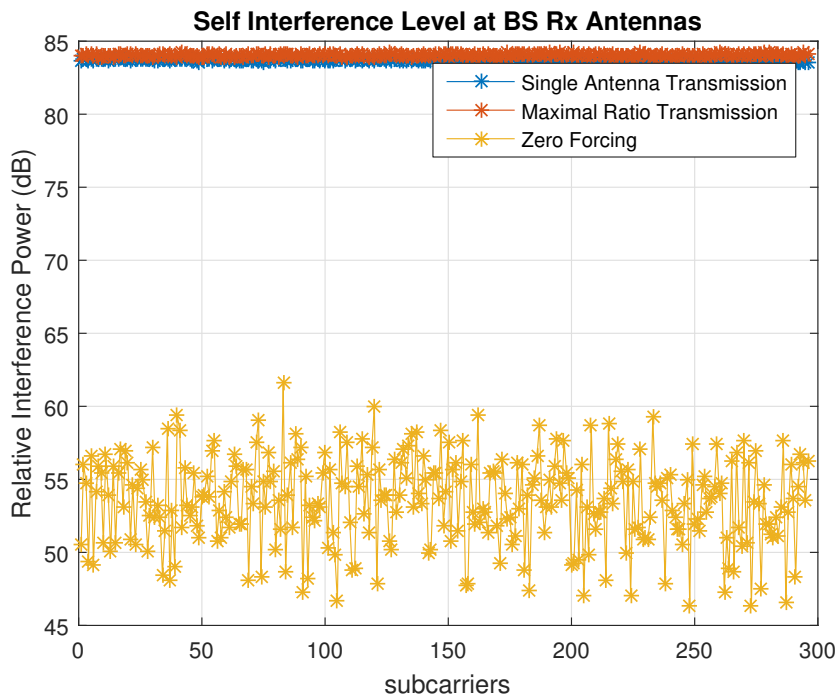


Figure 6.16: Interference level at the BS Rx for different BF approaches.

2×2 . Several configurations of placing the Tx and Rx antennas were tried before arriving at this configuration which gave the lowest value for the smaller singular value of the 2×2 channel. The plot of singular values at each subcarrier is shown in Fig. 6.18. The larger singular value is normalized to unity. This implies that with a careful choice of BS Tx and Rx antennas, it is possible to achieve a low rank internal channel. Such a choice would result in less Tx antennas dedicated to SIC and more Tx antennas free to perform the actual DL precoding.

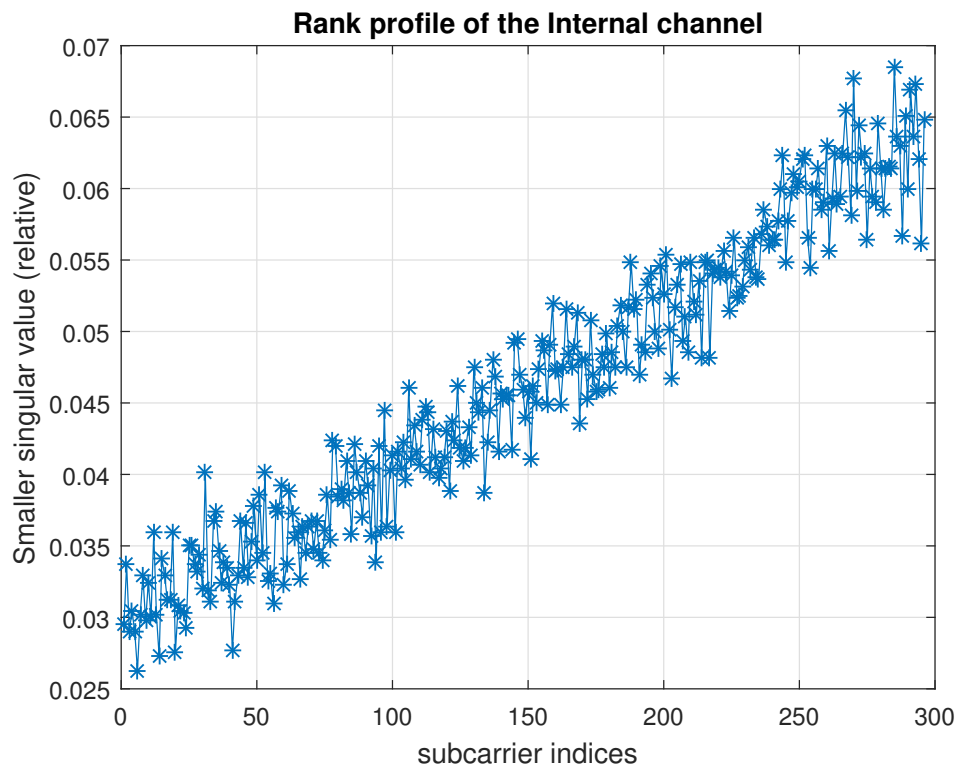


Figure 6.18: Smaller singular value at each subcarrier for the 2×2 channel. The larger singular value is normalized to unity.

- We created a new demo setup with USRPs from scratch and experimentally verified the SIC using multiple antennas. In addition, for a 2×2 internal channel between BS Tx and Rx antennas, we were able to show a favorable rank profile (low smaller singular value) for a judicious antenna placement.

CONCLUSION

In the previous chapters, we have presented our research related to multiple antenna communications for 5G. The main topics that have been explored are:

- Reciprocity calibration for Massive MIMO.
- Precoder design for rapidly time-varying channels such as in HST.

On the first topic, our research was focused on coming up with optimal estimators for the reciprocity calibration parameters. This naturally necessitated the derivation of the Cramer Rao Bound (CRB) so that we could do the following.

- Compare the existing estimators in the literature with the CRB.
- Gain insights into the optimal estimator and also compare our proposed estimators with the CRB.

The existing estimators in the literature focused on first eliminating the nuisance parameters and getting a least squares formulation involving only the calibration parameters. For the CRB derivation, we treated the problem jointly with the calibration parameters and the nuisance parameters which resulted in a simple, elegant and accurate expression. In continuation with this strategy, our optimal estimators also were based on a joint estimation of the parameters. Moreover, our CRB for calibration parameter estimation is applicable to a general setting that allows grouping of antennas. Our initial CRB derivation was done assuming a coherent channel scenario. Recognizing the importance of non-coherent estimation techniques, we also extended our result to a non-coherent scenario. Further, as part of our search for optimal estimators, we analyzed the existing least squares approaches and provided insights into why its performance

differs from that of the ML approach. The analysis resulted in the observation that the ML is actually a weighted version of the least squares approach. This is quite intuitive too as the equations that result after elimination of the nuisance parameters involve colored noise. The optimal algorithms that we derived were based on ML and Variational Bayes. Both these algorithms were based on a joint estimation of the calibration parameters and the nuisance parameters. In the VB approach, we departed from the typical view of the calibration parameters as being unknown deterministic parameters to a Bayesian formulation.

The HST problem focused on MIMO precoder design for a rapidly time varying channel that optimized the weighted sum rate (WSR). The time variations result from the different Doppler frequencies on the different time domain paths. Of course, a single Doppler frequency may always be estimated and compensated. Hence, it is the range of Doppler frequencies (the difference between the maximum and minimum Doppler frequency) that needs to be accounted for. Time variation results in ICI at the receiver which needs to be factored into the design to improve performance. To make the analysis tractable we have assumed the channel variation to be linear as has been done previously in the literature. However, we rigorously showed that this approximation is justified for our problem scenario. Once this was established, in the case of full CSIT, we observed that the problem is similar to that of a MIMO IBC precoding design and hence tapped into existing solutions in that space. Hence, we used the DC approach in [23] but re-interpret as a minorization [38] technique. We also incorporated into the design the excess CP windowing at the receiver to further help mitigate the ICI. Hence, we performed a joint optimization of the precoders and the receive windows. Our precoder design approach ensures convergence and this convergence property was built in while introducing the window optimization as well. In fact, the window optimization methods are useful in itself and are applicable as a stand-alone ICI mitigation technique at the receiver. Once the full CSIT based precoder design problem was solved, we turned our attention to more robust precoder designs where only partial CSIT is available. Given the random nature of the knowledge of the channel, an expected WSR (EWSR) metric was chosen for optimization. The key challenge here was to solve the optimization problem in the presence of this expectation operator. In a first approach, a large system approximation was performed to replace the expectation of the log determinant term with a deterministic equivalent in an iterative fashion. To enable this, we first re-arranged the system model in a very elegant manner to make it mathematically convenient. Another known approach to solve the EWSR metric is to substitute this metric with another metric that is used in the MaMIMO limit, namely the ESEI-WSR approach. We performed a refined analysis of this approximation and provided further insights and results supporting this approach.

Finally, some experimental results based on the theory have also been presented. In these experiments, we first validate the need for reciprocity calibration by comparing the performance of precoding techniques using the Eurecom MaMIMO test bed. Next, we perform precoding for an MU multi-cell scenario where we bring together the concepts of reciprocity calibration and MIMO

DL precoding. In particular, we proposed a naive duality based precoder design that does not need cross-link channel information. The experimental results show that the performance of this design is comparable to that of an ZF approach that has full cross-link information. And last, but not the least, we consider the exploitation of multiple antennas to achieve the self-interference cancellation (SIC) required in a Full Duplex setting. We also explore the importance of the rank profile of the channel between the Tx and the Rx antennas of the BS. The lower the number of significant singular values in this channel, the lesser the number of Tx antennas that have to be dedicated to performing the SIC, thus freeing up the rest of the Tx antennas to perform useful DL transmission. A chapter-wise list of contributions has been provided already at the end of each chapter, but we mention it here again for easy reference.

7.1 Contributions

Our contributions have already been summarized at the end of each chapter. However, we list them again here for easy reference.

7.1.1 Chapter 2

- Showed that the group calibration framework proposed in [?] can result in Fast calibration (Section 2.3.2).
- Came up with a simple and elegant expression for the CRB for calibration parameter estimation (Section 2.4) that includes both coherent and non-coherent estimation methods.
- Came up with optimal algorithms for calibration parameter estimation (Section 2.5).
- We analyzed the performance of least squares methods and showed analytically that their performance differs from that of the CRB simply because they don't take into account the fact that the noise is colored.
- Some of the above contributions were published in [?], [?] and the rest will be in [?].
- This work has also resulted in a patent submission [?].

7.1.2 Chapter 3

- We tackle the problem of designing the optimal precoders for a MIMO point to point link under high Doppler.
- Towards this, we first justify a linear approximation for the channel variation across the OFDM symbol.

- We come up with a good system model that can include the effect of the linear channel variation and the receive windowing using the excess CP.
- The system model reveals that the problem is similar to that of precoder design for a MIMO IBC with an additional receive window coefficients to be optimized as well.
- Due to the similarity of the problem with MIMO IBC, we take advantage of the difference of concave approach in [23].
- We re-interpret the approach in [23] as an instance of the majorization technique [38].
- The window optimization is performed via alternating minimization.
- We prove the convergence of the entire design.
- The work detailed here resulted in the publications [?], [?].

7.1.3 Chapter 4

- Extended the full CSIT results to a more relaxed setting of partial CSIT.
- Came up with a system model that facilitated the use of the Large system approximation to solve the optimization problem under partial CSIT.
- Employed large system approximation to solve the EWSR optimizing precoders which work quite well even at small values of Tx and Rx number of antennas.
- This work was published in [?].

7.1.4 Chapter 5

- Motivated the use of the ESEI-WSR metric (or the MaMIMO limit of the EWSR) for utility optimization involving partial CSIT.
- Showed that the gap is maximum at infinite SNR and that it reduces with increasing number of transmit antennas.
- Also touched upon the actual gap criterion and showed that for a specific MISO scenario with covariance only CSIT, this gap is zero. I.e, the ESEI-WSR metric optimization results in the true EWSR optimum.
- This work was published in [?].

7.1.5 Chapter 6

- Performed actual over-the-air demo using Eurecom's MaMIMO test bed.
- Performed experiments to check the effectiveness of calibration parameters.
- Came up with a naive DL precoder that takes into account reciprocity calibration parameters. This work was published in [?].
- We created a new demo setup with USRPs from scratch and experimentally verified the SIC using multiple antennas. In addition, for a 2×2 internal channel between BS Tx and Rx antennas, we were able to show a favorable rank profile (low smaller singular value) for judicious antenna placement.
- Some of the experimental work was also published in [?].



APPENDIX A

We show in the following that the column space of \mathcal{F}^\perp defined by (2.57) spans the orthogonal complement of the column space of \mathcal{F} assuming that \mathbf{P}_i is full rank for all i and that either $L_i \geq M_i$ or $M_i \geq L_i$ for all i . This proof is not a contribution of the author of this thesis and was done by the second author in [?].

Proof. First, using $(\mathbf{A} \otimes \mathbf{B})(\mathbf{C} \otimes \mathbf{D}) = (\mathbf{AC} \otimes \mathbf{BD})$, it holds

$$(A.1) \quad \underbrace{\begin{bmatrix} \mathbf{I}_{L_i} \otimes \mathbf{P}_j^T \mathbf{F}_j & -\mathbf{P}_i^T \mathbf{F}_i \otimes \mathbf{I}_{L_j} \end{bmatrix}}_{L_i L_j \times (L_i M_j + L_j M_i)} \underbrace{\begin{bmatrix} \mathbf{P}_i^T \mathbf{F}_i \otimes \mathbf{I}_{M_j} \\ \mathbf{I}_{M_i} \otimes \mathbf{P}_j^T \mathbf{F}_j \end{bmatrix}}_{(L_i M_j + L_j M_i) \times M_i M_j} = \mathbf{0}.$$

Then, the row space of the left matrix of (A.1) is orthogonal to the column space of the right matrix. As \mathcal{F} in (2.43) and $\mathcal{F}^{\perp H}$ are block diagonal with blocks of the form of (A.1), it suffices then to prove that the following matrix \mathbf{M} has full column rank, i.e., $L_i M_j + L_j M_i$, which is then also its row rank

$$(A.2) \quad \mathbf{M} := \begin{pmatrix} \mathbf{I}_{L_i} \otimes \mathbf{P}_j^T \mathbf{F}_j & -\mathbf{P}_i^T \mathbf{F}_i \otimes \mathbf{I}_{L_j} \\ (\mathbf{F}_i \mathbf{P}_i)^* \otimes \mathbf{I}_{M_j} & \mathbf{I}_{M_i} \otimes (\mathbf{F}_j \mathbf{P}_j)^* \end{pmatrix}.$$

Denote $\mathbf{A}_i := \mathbf{P}_i^T \mathbf{F}_i \in \mathbb{C}^{L_i \times M_i}$ and $\mathbf{A}_j := \mathbf{P}_j^T \mathbf{F}_j \in \mathbb{C}^{L_j \times M_j}$. Then, by assumption, it holds that either $\text{rank}(\mathbf{A}_i) = M_i$ and $\text{rank}(\mathbf{A}_j) = M_j$ or $\text{rank}(\mathbf{A}_i) = L_i$ and $\text{rank}(\mathbf{A}_j) = L_j$. Let $\mathbf{x} = [\mathbf{x}_1^T \ \mathbf{x}_2^T]^T$ be such that $\mathbf{M}\mathbf{x} = \mathbf{0}$ and show that $\mathbf{x} = \mathbf{0}$. Since $\mathbf{M}\mathbf{x} = \mathbf{0}$, it holds

$$\begin{cases} (\mathbf{I}_{L_i} \otimes \mathbf{A}_j)\mathbf{x}_1 - (\mathbf{A}_i \otimes \mathbf{I}_{L_j})\mathbf{x}_2 = \mathbf{0} \\ (\mathbf{A}_i^H \otimes \mathbf{I}_{M_j})\mathbf{x}_1 + (\mathbf{I}_{M_i} \otimes \mathbf{A}_j)\mathbf{x}_2 = \mathbf{0}. \end{cases}$$

Let \mathbf{x}_1 and \mathbf{x}_2 be matrices such that $\text{vec}(\mathbf{x}_1) = \mathbf{x}_1$ and $\text{vec}(\mathbf{x}_2) = \mathbf{x}_2$. Then

$$\begin{cases} \mathbf{A}_j \mathbf{x}_1 - \mathbf{x}_2 \mathbf{A}_i^T = \mathbf{0} \\ \mathbf{x}_1 \mathbf{A}_i^* + \mathbf{A}_j^H \mathbf{x}_2 = \mathbf{0}. \end{cases}$$

Multiplying the first equation by \mathbf{A}_j^H and the second by \mathbf{A}_i^T , and summing them up, we get $\mathbf{A}_j^H \mathbf{A}_j \mathbf{x}_1 + \mathbf{x}_1 (\mathbf{A}_i \mathbf{A}_i^H)^* = 0$, which is a Sylvester's equation admitting a unique solution if $\mathbf{A}_j^H \mathbf{A}_j$ and $-(\mathbf{A}_i \mathbf{A}_i^H)^*$ have no common eigenvalues. On the other hand, the eigenvalues of $\mathbf{A}_j^H \mathbf{A}_j$ and $\mathbf{A}_i \mathbf{A}_i^H$ are real positive, so common eigenvalues of $\mathbf{A}_j^H \mathbf{A}_j$ and $-(\mathbf{A}_i \mathbf{A}_i^H)^*$ can only be 0. However, this does not occur since by the assumptions either $\mathbf{A}_j^H \mathbf{A}_j$ or $\mathbf{A}_i \mathbf{A}_i^H$ is full rank. We can then conclude that $\mathbf{x}_1 = 0$, i.e., $\mathbf{x}_1 = 0$. Similarly, $\mathbf{x}_2 = 0$, which ends the proof. ■

BIBLIOGRAPHY

- [1] D. BHARADIA, E. MCMILIN, AND S. KATTI, *Full duplex radios*, SIGCOMM Comput. Commun. Rev., 43 (2013).
- [2] S. BOYD AND L. VANDENBERGHE, *Convex Optimization*, Cambridge University Press, New York, USA, 2004.
- [3] E. D. CARVALHO, S. OMAR, AND D. SLOCK, *Performance and complexity analysis of blind FIR channel identification algorithms based on deterministic maximum likelihood in SIMO systems*, Circuits, Systems, and Signal Processing, (2013).
- [4] E. D. CARVALHO AND D. SLOCK, *Semi-Blind Methods for FIR Multichannel Estimation*, in Signal processing advances in wireless communications, Prentice Hall, 2000, ch. 7.
- [5] T. M. COVER AND J. A. THOMAS, *Elements of Information Theory (Wiley Series in Telecommunications and Signal Processing)*, Wiley-Interscience, 2006.
- [6] E. DE CARVALHO AND D. SLOCK, *Cramér-rao bounds for blind multichannel estimation*, CoRR, abs/1710.01605 (2017).
- [7] M. DUARTE AND A. SABHARWAL, *Full-duplex wireless communications using off-the-shelf radios: Feasibility and first results*, in Asilomar Conf. on Signals, Systems and Computers, Nov 2010.
- [8] J. DUMONT, W. HACHEM, S. LASAULCE, P. LOUBATON, AND J. NAJIM, *On the Capacity Achieving Covariance Matrix for Rician MIMO Channels: An Asymptotic Approach*, IEEE Trans. on Information Theory, (2010).
- [9] E. BJÖRNSON, J. HOYDIS, AND L. SANGUINETTI, *Massive mimo networks: Spectral, energy, and hardware efficiency*, Foundations and Trends® in Signal Processing, (2017).
- [10] E. EVERETT, C. SHEPARD, L. ZHONG, AND A. SABHARWAL, *Softnull: Many-antenna full-duplex wireless via digital beamforming*, IEEE Trans. Wireless Communications, (2016).
- [11] A. FARHANG, N. MARCHETTI, L. E. DOYLE, AND B. FARHANG-BOROJENY, *Low Complexity CFO Compensation in Uplink OFDMA Systems With Receiver Windowing*, IEEE Trans. on Signal Processing, (2015).

BIBLIOGRAPHY

- [12] M. FAULKNER, L. WILHELMSSON, AND J. SVENSSON, *Low-Complex ICI Cancellation for Improving Doppler Performance in OFDM Systems*, in IEEE Vehicular Technology Conference, Sept 2006.
- [13] E. FOROOZANFARD, O. FRANEK, A. TATOMIRESCU, E. TSAKALAKI, E. D. CARVALHO, AND G. F. PEDERSEN, *Full-duplex mimo system based on antenna cancellation technique*, Elec. Lett., (2014).
- [14] A. GHOSH, J. ZHANG, J. G. ANDREWS, AND R. MUHAMED, *Fundamentals of LTE*, Prentice Hall Press, Upper Saddle River, NJ, USA, 1st ed., 2010.
- [15] G. H. GOLUB AND C. F. VAN LOAN, *Matrix Computations (3rd Ed.)*, Johns Hopkins University Press, Baltimore, MD, USA, 1996.
- [16] D. HAMMARWALL, M. BENGTSSON, AND B. OTTERSTEN, *Acquiring partial csi for spatially selective transmission by instantaneous channel norm feedback*, IEEE Transactions on Signal Processing, (2008).
- [17] A. HJORUNGNES AND D. GESBERT, *Complex-Valued Matrix Differentiation: Techniques and Key Results*, IEEE Transactions on Signal Processing, (2007).
- [18] D. HOANG AND R. A. ILTIS, *Noncooperative Eigencoding for MIMO Ad hoc Networks*, IEEE Transactions on Signal Processing, (2008).
- [19] P. H. M. JANSSEN AND P. STOICA, *On the expectation of the product of four matrix-valued gaussian random variables*, IEEE Transactions on Automatic Control, (1988).
- [20] X. JIANG, M. ČIRKIĆ, F. KALTENBERGER, E. G. LARSSON, L. DENEIRE, AND R. KNOPP, *MIMO-TDD reciprocity and hardware imbalances: experimental results*, in Proc. IEEE Intern. Conf. on Commun. (ICC), London, United Kingdom, Jun. 2015.
- [21] F. KALTENBERGER, A. BYIRINGIRO, G. ARVANITAKIS, R. GHADDAB, D. NUSSBAUM, R. KNOPP, M. BERNINEAU, Y. COCHERIL, H. PHILIPPE, AND E. SIMON, *Broadband wireless channel measurements for high speed trains*, in 2015 IEEE International Conference on Communications (ICC), June.
- [22] C. KHATRI AND C. R. RAO, *Solutions to some functional equations and their applications to characterization of probability distributions*, Sankhyā: The Indian Journal of Statistics, Series A, (1968).
- [23] S.-J. KIM AND G. GIANNAKIS, *Optimal Resource Allocation for MIMO Ad Hoc Cognitive Radio Networks*, IEEE Transactions on Information Theory, (2011).

-
- [24] Y. LEJOSNE, A. BEN NASSER, D. T. SLOCK, AND Y. YUAN WU, *Multi-cell multi-user MIMO downlink with partial CSIT and decentralized design*, in 10th IEEE Broadband Wireless Access workshop, colocated with IEEE GLOBECOM , Austin, Texas, USA, 2014.
- [25] T. L. MARZETTA, *How Much Training is Required for Multiuser MIMO?*, in 2006 Fortieth Asilomar Conference on Signals, Systems and Computers, Oct 2006.
- [26] T. L. MARZETTA, *Noncooperative Cellular Wireless with Unlimited Numbers of Base Station Antennas*, IEEE Transactions on Wireless Communications, (2010).
- [27] M. BENGTTSSON AND P. ZETTERBERG, *Some notes on the kronecker model*, EURASIP JOURNAL ON WIRELESS COMMUNICATIONS AND NETWORKING, (2006).
- [28] R. J. MUIRHEAD, *Aspects of Multivariate Statistical Theory*, John Wiley and Sons, Inc., 2008.
- [29] F. NEGRO, I. GHAURI, AND D. T. M. SLOCK, *Sum Rate maximization in the noisy MIMO interfering broadcast channel with partial CSIT via the expected weighted MSE*, in International Symposium on Wireless Communication Systems (ISWCS), Aug 2012.
- [30] M. OPPER AND O. WINTHER, *Expectation Consistent Approximate Inference*, J. Mach. Learn. Res., 6 (2005).
- [31] H. PAPADOPOULOS, O. Y. BURSALIOGLU, AND G. CAIRE, *Avalanche: Fast RF calibration of massive arrays*, in Proc. IEEE Global Conf. on Signal and Information Process. (GlobalSIP), Washington, DC, USA, Dec. 2014.
- [32] R1-091752, *Performance study on Tx/Rx mismatch in LTE TDD dual-layer beamforming*. Nokia, Nokia Siemens Networks, CATT, ZTE, 3GPP RAN1 #57, May 2009.
- [33] R1-091794, *Hardware calibration requirement for dual layer beamforming*. Huawei, 3GPP RAN1 #57, May 2009.
- [34] R. ROGALIN, O. BURSALIOGLU, H. PAPADOPOULOS, G. CAIRE, A. MOLISCH, A. MICHALO-LIAKOS, V. BALAN, AND K. PSOUNIS, *Scalable synchronization and reciprocity calibration for distributed multiuser MIMO*, IEEE Trans. Wireless Commun., (2014).
- [35] R. ROGALIN, O. Y. BURSALIOGLU, H. C. PAPADOPOULOS, G. CAIRE, AND A. F. MOLISCH, *Hardware-impairment compensation for enabling distributed large-scale MIMO*, in Proc. Information Theory and Applications (ITA) Workshop, San Diego, California, USA., Feb. 2013.
- [36] M. SHAO AND W.-K. MA, *A simple way to approximate average robust multiuser MISO transmit optimization under covariance-based CSIT*, in IEEE Int'l Conf. on Acoustics, Speech and Signal Processing (ICASSP), New Orleans, USA, Mar. 2017.

BIBLIOGRAPHY

- [37] C. SHEPARD, N. YU, H. AND ANAND, E. LI, T. MARZETTA, R. YANG, AND L. ZHONG, *Argos: Practical many-antenna base stations*, in Proc. ACM Intern. Conf. Mobile Computing and Netw. (Mobicom), Istanbul, Turkey, Aug. 2012.
- [38] P. STOICA AND Y. SELEN, *Cyclic minimizers, majorization techniques, and the expectation-maximization algorithm: a refresher*, IEEE Signal Processing Magazine, (2004).
- [39] G. TARICCO, *Asymptotic Mutual Information Statistics of Separately Correlated Rician Fading MIMO Channels*, IEEE Transactions on Information Theory, (2008).
- [40] I. E. TELATAR, *Capacity of multi-antenna Gaussian channels*, EUROPEAN TRANSACTIONS ON TELECOMMUNICATIONS, (1999).
- [41] K. T. TRUONG AND R. W. HEATH, *The viability of distributed antennas for massive MIMO systems*, in Asilomar Conf. on Signals, Systems and Computers, Nov 2013.
- [42] E. TSAKALAKI, E. FOROOZANFARD, E. D. CARVALHO, AND G. F. PEDERSEN, *A 2-order mimo full-duplex antenna system*, in The 8th European Conf. on Antennas and Propagation (EuCAP), Apr. 2014.
- [43] J. VIEIRA, F. RUSEK, O. EDFORS, S. MALKOWSKY, L. LIU, AND F. TUFVESSON, *Reciprocity Calibration for Massive MIMO: Proposal, Modeling and Validation*, IEEE Trans. Wireless Commun., (2017).
- [44] J. VIEIRA, F. RUSEK, AND F. TUFVESSON, *Reciprocity calibration methods for massive MIMO based on antenna coupling*, in 2014 IEEE Global Communications Conference, Dec 2014.
- [45] H. WEI, W. D., AND X. YOU, *Reciprocity of mutual coupling for TDD massive MIMO systems*, in Proc. Intern. Conf. on Wireless Commun. and Signal Process. (WCSP), Nanjing, China, Oct. 2015.
- [46] H. WEI, D. WANG, H. ZHU, J. WANG, S. SUN, AND X. YOU, *Mutual Coupling Calibration for Multiuser Massive MIMO Systems*, IEEE Trans. on Wireless Communications, 15 (2016).
- [47] B. WIDROW, K. DUVAL, R. GOOCH, AND W. NEWMAN, *Signal cancellation phenomena in adaptive antennas: Causes and cures*, IEEE Trans. on Ant. and Prop., (1982).
- [48] Y. PENG, W. WANG, AND Y. I. KIM, *Performance Analysis of OFDM System Over Time-Selective Fading Channels*, in IEEE Wireless Communications and Networking Conference (WCNC), Apr. 2009.